Evaporative instability in binary mixtures

Kamuran Erdem Uguz

UNIVERSITE PARIS-SUD

ÉCOLE DOCTORALE : Physique de la Région Parisienne
Laboratoire LIMSI

DISCIPLINE Physique

THÈSE DE DOCTORAT

soutenue le 20/09/2012

par

Kamuran Erdem Uguz

Evaporative instability in binary mixtures

Directeur de thèse :	Claudine Dang Vu-Delcarte	Professeur, Université Paris-Sud
Co-directeur de thèse :	Ranga Narayanan	Professeur, University of Florida

Composition du jury :

Président du jury :	Oscar Crisalle	Professeur, University of Florida
Rapporteurs :	Sakir Amiroudine	Professeur, Université de Bordeaux 1
	Farzam Zoueshtiagh	Maître de Conférences, Université de Lille 1
Examinateurs :	Guillaume Kasperski	Maître de Conférences, Université Paris-Sud
	Corin Segal	Professeur, University of Florida
	Kirk Ziegler	Professeur Associé, University of Florida
Membres invités :	Gérard Labrosse	Professeur retraité, Université Paris-Sud

To people who are proud of me

ACKNOWLEDGMENTS

First of all, I would like to thank Professor Ranga Narayanan for his support and advice. He has been both a mentor and a friend. He always emphasizes the importance of enjoying your work. Prof. Narayanan is enthusiastic about his work and this is the best motivation for a student. His dedication to teaching and his philosophy have inspired me.

I would like to thank the members of my PhD committee, Prof. Claudine Dang Vu-Delcarte, Prof. Sakir Amiroudine, Prof. Farzam Zouesthsiagh, Prof. Guillaume Kasperski, Prof. Corin Segal, Prof. Kirk Ziegler, and special thanks to Prof. Oscar Crisalle for being the president of the committee. Also, I would like to thank Prof. Gérard Labrosse for sharing his knowledge and experiences.

I would like to thank my brother, Kerem Uğuz, who has always been with me, and has motivated me for my work. I would like to express my highest appreciation for my parents and my brother for their love and support throughout my educational career. It has been difficult for them and for me because of the large distance. Thank you for your patience, encouragement and your moral support.

I would like to thank the Partner University Fund and the Embassy of France for a Chateaubriand Fellowship during Spring 2011 and the University of Florida for the part-alumni fellowship for a major part of my Doctoral work. The National Science Foundation provided funding via grant NSF OISE 0968313 is gratefully acknowledged. I am grateful to all of them in no small measure.

TABLE OF CONTENTS

LIST OF TABLES

LIST OF FIGURES

Abstract

EVAPORATIVE INSTABILITY IN BINARY MIXTURES

By
Kamuran Erdem Uguz

August 2012

This study focuses on the understanding of the physics of convective flow resulting from evaporative instability in binary mixtures. The system of interest consists of a liquid mixture underlying its own vapor sandwiched between two conducting plates with insulated sidewalls in a closed container, i.e., total mass is conserved. In this system it is important to understand how the fluid dynamics and the heat and mass transfer interact competitively to form patterns. The main goal of this work is to identify the conditions for the system going from the conductive no-flow state to a convection state when the applied vertical temperature gradient exceeds a certain value called the critical value.

Convection arises due to; evaporation, density gradients, and interfacial-tension gradients. These convective forces are opposed by the diffusion effects (vorticity diffusion, heat diffusion, and mass diffusion) that try to keep the system in the conductive state. First, the problem is studied for a single component system using a three dimensional model to investigate the sidewalls effects on the onset point. After identifying the effect of sidewall, the binary system is studied using a one dimensional model both in the presence and in the absence of gravity. An experimental set-up was built to verify many of the qualitative predictions.

Four major results arise from this work. First, in a multi-component system in the absence of gravity, an instability arises only when the system is heated from the vapor side as opposed to evaporation in a single-component. The implication is that evaporative processes in thin layers or in micro-gravity are best conducted with heat from the liquid side if instabilities are to be avoided.

Second, in the presence of gravity, a multi-component system may become unstable no matter the direction of heating. This means that the applied temperature difference must be kept below a threshold in order to avoid flow instabilities for either heating direction.

Third, whenever instability occurs in the absence of gravity, patterns will not result in the case of a pure component but may result in the case of multi-components. Likewise, patterns will result when gravity is taken into account provided the aspect ratio of the container lies in a suitable range. As a result, aspect ratios can be chosen to avoid multi-cellular patterns even if convective flow instabilities arise during evaporation.

Lastly, oscillations are not ordinarily predicted despite opposing effects of solutal and thermal convection in the evaporation problem.

CHAPTER 1
INTRODUCTION TO THE PHYSICS

Evaporation is an important process in many industrial applications such as heat pipes, spin coating of materials, paint drying, and glass fabrication where at least two phases, like liquid and vapor, are in contact with one another via an interface. In many of these applications evaporation is generally accompanied by either a temperature gradient or a concentration gradient, if not both. Due to these applied or induced gradients, an evaporation process can lead to an instability which can affect the final quality of the product. The instability manifests itself as an undulation of the interface between the phases and an onset of convective flow. Therefore, a better understanding of the evaporation process, especially in multi-component mixtures, is not only of scientific interest but also of industrial importance.

The fluid flow that arises on account of instability in an evaporative process is not only caused by the evaporation itself but also due to density gradients and forces arising from surface tension gradients. When you combine all these effects for a multi-component system, the physics of the problem becomes very complicated. Therefore, in the following three sub-sections all these phenomena; flow due to evaporation, flow due to buoyancy forces and flow due to surface tension gradients will be discussed one at a time employing explanatory picture arguments.

1.1 Pure Evaporative Instability

An evaporating liquid can convect even in the absence of gravity or surface tension gradient effects. This is termed pure evaporative convection. To understand why pure evaporative convection can occur in a multi-component system, consider Figures 1-1 and 1-2 which depict a liquid mixture in equilibrium with its vapor in a closed vessel subject to a vertical temperature gradient. Figure 1-1 shows the heating arrangement where the heat needed for evaporation is supplied from the liquid side while Figure 1-2 shows heat input from the vapor side. For the sake of understanding the physics

imagine that there are no fluid dynamics present in the system. As the system is closed, the net evaporation rate is zero. However, in the presence of mechanical perturbation local evaporation and local condensation will take place at the liquid-vapor interface for both heating arrangements. In the figures the dotted wave represents a perturbed interface while the dotted lines represent the temperature profiles in the perturbed state at the interface.

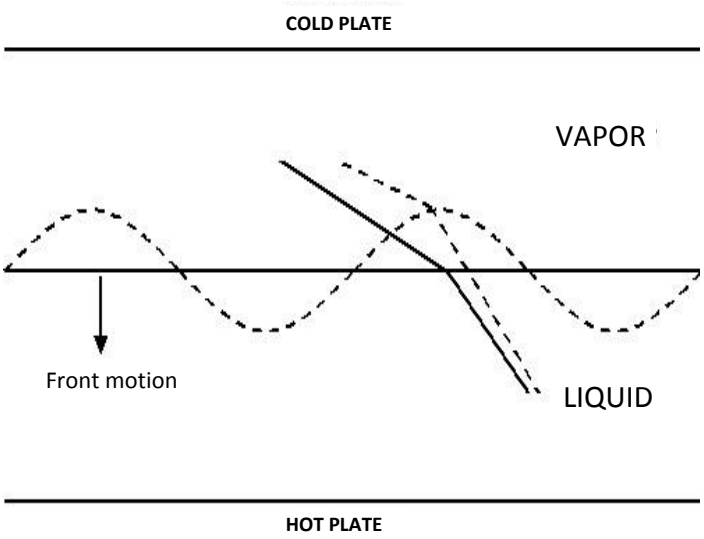

Figure 1-1. Heat input from the liquid side, unstable to all wave numbers.

When the heat is supplied from the liquid side as in Figure 1-1, the temperature gradient at a trough becomes more pronounced on account of its proximity to the hot boundary. The rate of evaporation from the trough is thus increased and the trough becomes deeper which enhances the instability. On the other hand, when the system is heated from the vapor side as in Figure 1-2, the crest gets closer to the heat source and evaporation is enhanced there which stabilizes the interface.

Observe that when the heat is supplied from the liquid side the system is unstable to all disturbances. In other words, the disturbance will grow with time, independent of the wavelength of the disturbance. However, when the heat is supplied from above, i.e. from the vapor side, the system is always stable. Figure 1-3 depicts pure evaporative convection with fluid dynamics present in both phases; but, other convective effects like

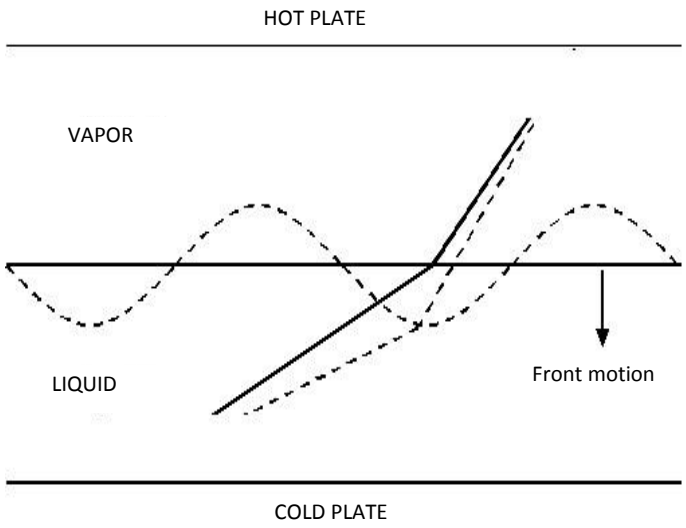

Figure 1-2. Heat input from the vapor side, stable to all wave numbers.

buoyancy driven flows and the interfacial tension gradient driven flows are still ignored. As before, on the perturbed interface the trough is the local evaporation and the crest is the local condensation point. Due to the evaporation, there is an upward flow from the bulk toward the trough. The upward flow from the bulk brings warm liquid to the trough enhancing the instability. On the other hand, the flow in the vapor phase takes place from trough to crest on account of a higher pressure at the trough. This flow brings warm vapor to the cold crest and helps to re-establish the temperature uniformity. This instability occurs at any wave number when the applied temperature difference is larger than the critical temperature. Interfacial tension acts to stabilize the surface and therefore selects the critical wavelength. Due to the large density difference between the vapor and the liquid, the flow in the vapor is much stronger than the flow in the liquid. Observe from the picture argument that pure evaporative instability would not occur if the bilayer arrangement were to be heated from the vapor side because, in that case, like vapor flow, the bulk flow in the liquid would also be stabilizing.

Note that we have not mentioned anything about the system being multi-component until this point because the physics of multi-component and single component systems for pure evaporative process are identical. However, in the presence of gravity and/or

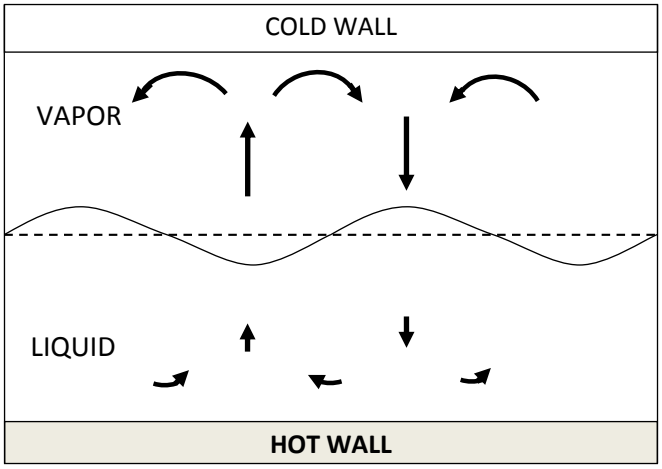

Figure 1-3. Physics with fluid dynamics.

interfacial tension gradient effects, having a binary mixture changes the physics drastically.

1.2 Rayleigh or Buoyancy-Driven Convection

Buoyancy-driven convection, often termed natural convection or Rayleigh convection, occurs when a fluid is subject to a temperature gradient or a concentration gradient in a gravitational field and when there is a variation of density with respect to temperature and/or concentration. To understand the physics of the Rayleigh convection let us separate the problem into two parts: first, the thermal problem where the density dependence on the mass fraction is ignored and then, the solutal problem where the density of the mixture does not depend on temperature.

Figure 1-4 is drawn to show the physics of the thermal problem where the bilayer is heated from the liquid side. Knowing that density ordinarily decreases with increasing temperature, in this setup the density of the fluid near the upper plate is higher than the density of the fluid near the bottom plate. In other words, the temperature gradient creates a gravitationally unstable stratification. For sufficiently small temperature differences this stratification is stable and the system is able to conduct heat from the lower plate to the upper one by creating a linear temperature gradient.

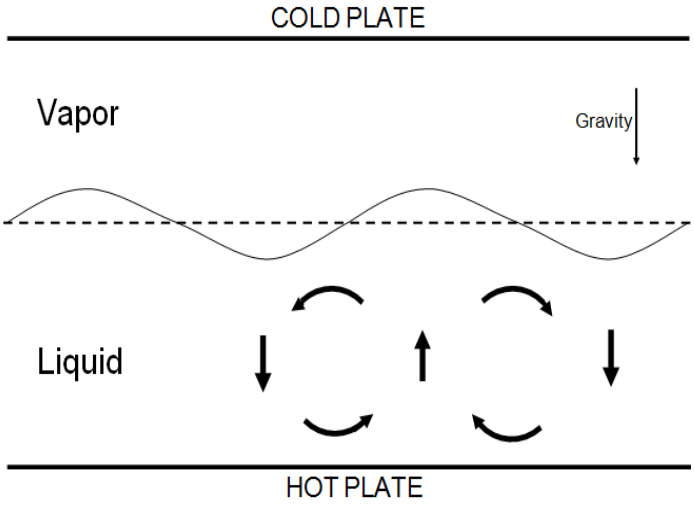

Figure 1-4. Thermal Rayleigh convection.

Now imagine giving a mechanical perturbation to the conductive system by pushing an element of liquid downwards. The density of this liquid element is higher than the ones that underlie it, so it will continue moving downward. Meanwhile due to the mass conversation, the liquid from below ought to move upward. The downward-moving cold fluid elements are heated as they reach the bottom of the system while the upward-moving fluid elements are cooled as they reach the top of the system.

This flow will continue unabated unless the liquid's kinematic viscosity and thermal diffusivity are large enough to settle down the perturbation. Thermal diffusivity helps the downward moving fluid element to reach the same temperature as its environment, and decrease the density. Kinematic viscosity also works against convection by slowing down the mechanical perturbations in the flow. However, there is a critical applied temperature gradient where the viscosity and the thermal diffusivity cannot outweigh the destabilizing effects and disturbances will grow. The balance between these forces is represented by a dimensionless number called thermal Rayleigh number, which arises from scaling the nonlinear equations and is given by,

$$Ra_T = \frac{\beta_T g \Delta T d^3}{\nu \kappa} \tag{1–1}$$

Here;

β_T : Negative thermal expansion coefficient (a positive number).

g : Magnitude of gravity.

ΔT : Temperature difference.

d : Height of the liquid.

ν : Kinematic viscosity.

κ : Thermal diffusivity.

Convection can initiate in either phase simultaneously or propagate from one to the other, depending on the domain dimensions, thermal, and mechanical properties of the phases. Observe that instability would not occur if the bilayer were to be heated from the vapor side because it creates light over heavy configuration, which is a stable configuration with respect to gravity.

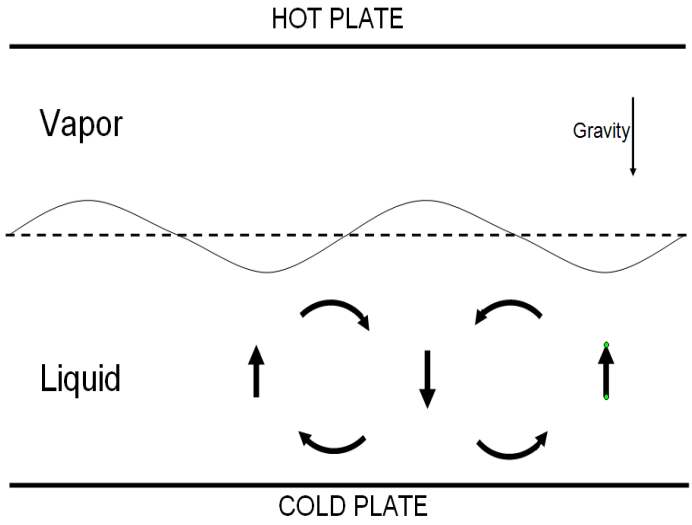

Figure 1-5. Solutal Rayleigh convection.

Now let us look at the solutal Rayleigh convection ignoring the temperature dependence of the density. Concentration gradients can be imposed similar to the temperature gradient by keeping the top and bottom plates at constant concentration which is experimentally hard to achieve. Alternatively the concentration gradient can be induced via evaporation. In the latter case, the concentration gradient is created by

the different evaporation rates of the components where the local temperature gradient is adjusted by the local evaporation and the local condensation. Figure 1-5 depicts the system heat supplied from the vapor side where the concentration gradient is a result of different evaporation rates of the components. To understand the physics we consider a case of a multi-component mixture made up of two simple alcohols such as ethanol and secondary butanol (sec-butanol), the former being the more volatile and the less dense one. In order words, the density of the mixture decreases with increasing ethanol concentration. Upon perturbation, ethanol evaporates more than sec-butanol at the crest creating a sec-butanol rich heavy point while the trough is ethanol rich and light. Therefore, the fluid pocket at the crest sinks and pushes the cold fluid from the bottom of the domain to the cold trough enhancing the instability, while the mass diffusion and the viscosity enhance the stability. Here the balance between destabilizing density gradient effect and stabilizing mass diffusion and viscosity is given by,

$$Ra_{\omega} = \frac{\beta_{\omega} g d^3}{\nu D_{AB}} \tag{1–2}$$

Here:

β_{ω} : Negative solutal expansion coefficient.

D_{AB} : Mass diffusivity.

Observe that the solutal Rayleigh number does not contain a term such as ΔC which would be analogous to ΔT in the thermal Rayleigh number because there is no applied concentration gradient in the system. Also that is the upper bound of the solutal Rayleigh number by virtue of its definition. The other point that requires attention is that when the heat is supplied from the liquid side, solutal Rayleigh cannot initiate convection in the system simply because the crest would be rich in ethanol and therefore it would be light.

1.3 Pure Marangoni or Interfacial Tension Gradient-Driven Convection

Interfacial tension gradient-driven convection or Marangoni convection is unlike buoyancy-driven convection and can occur in a fluid even in the absence of a gravitational field. Like the density, interfacial tension also depends on both temperature and concentration; therefore, it is best to investigate the physics of the Marangoni convection in two parts as done for the Rayleigh convection: so first, the thermal problem where the mass fraction dependence of surface tension is ignored, and second the solutal problem where the temperature dependence is ignored.

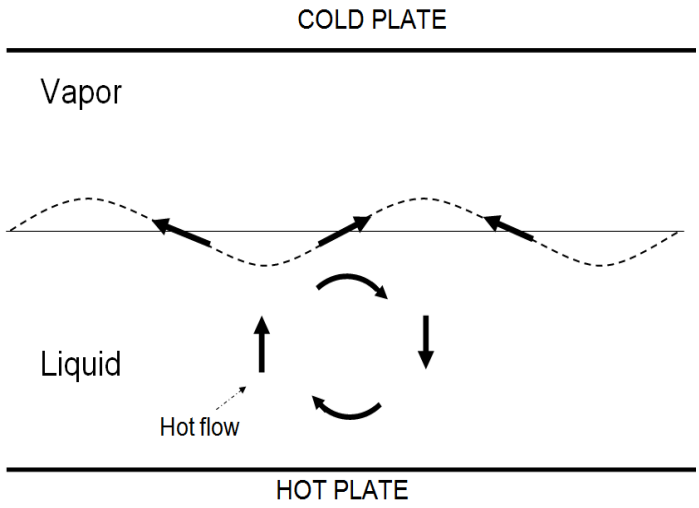

Figure 1-6. Thermal Marangoni convection.

Similar to density, interfacial tension decreases with increasing temperature. Imagine the vapor-liquid bilayer subject to vertical temperature gradient where the heat is supplied from the liquid side as depicted in Figure 1-6. On the perturbed interface there is an interfacial tension gradient caused by the temperature gradient where the interfacial tension is higher at the cold crest. Due to this gradient a flow occurs from trough to crest dragging hotter liquid from the bulk to the crest, enhancing the Marangoni flow. In the gas phase the flow brings the cold fluid from the cold plate to the crest working for the stability; however, the effect of this flow in the vapor phase is less than the liquid phase because of gas phase's high kinematic viscosity. In addition to

vapor flow, the destabilizing effect of the liquid flow can be out powered by the thermal diffusivity and by dynamic viscosity if the applied temperature gradient is sufficiently small. In other words, much like the case of buoyancy-driven convection, there is a critical temperature difference where the Marangoni flow cannot be dampened by the thermal diffusivity or the viscosity, and at that point convection starts. Again like the buoyancy-driven convection case, a dimensionless group arises from the scaled modeling equations that exhibit the balance between stabilizing diffusive effects and the destabilizing interfacial tension gradient effects. This dimensionless group is called the thermal Marangoni number and is given by,

$$\mathrm{Ma_T} = \frac{\gamma_T \Delta T d}{\mu \kappa} \tag{1–3}$$

Here;

γ_T: Change in the interfacial tension with respect to the temperature.

μ : Dynamic viscosity.

Note that, as in the pure evaporative and the thermal Rayleigh convection problems, here also heating from the vapor side is a stable configuration.

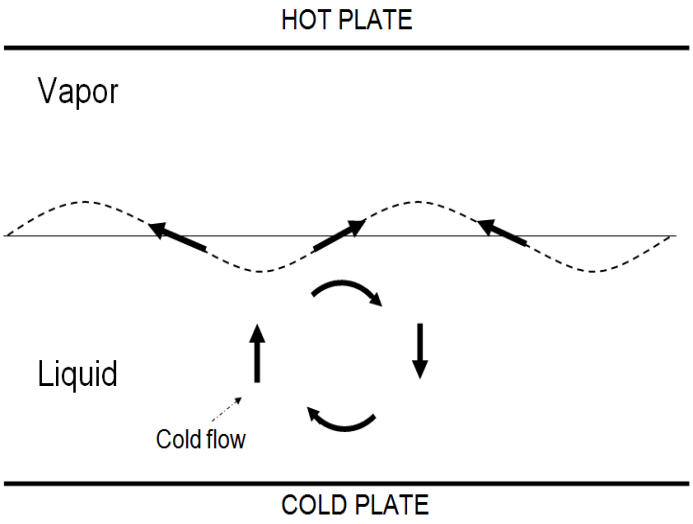

Figure 1-7. Solutal Marangoni convection.

To understand the solutal Marangoni convection, again consider the ethanol and sec-butanol binary mixture. In this mixture ethanol is the more volatile component with a smaller interfacial tension. Therefore, the interfacial tension of the mixture decreases with increasing ethanol concentration. Figure 1-7 depicts the bilayer binary mixture heated from the vapor side. On the perturbed interface, i.e., the dotted lines, the crest would be ethanol rich compared to the trough; as a result, the interfacial tension is lower at the crest. Due to this interfacial tension gradient along the interface, flow takes place from crest to trough, dragging cooler liquid from the bulk to the crest enhancing the condensation and enhancing the interfacial tension gradient. The gradient also causes a flow in the vapor phase which brings the hot flow to the cold crest trying to re-establish temperature uniformity and enhancing the stability. However, the effect of vapor phase flow is less than the liquid phase flow because of gas phase's high kinematic viscosity. Again, there is a critical applied temperature difference, which is the only cause of concentration gradient in the system, where the dynamic viscosity and mass diffusion of the system is not strong enough to sustain the stability and convection sets in. This time the balance between the destabilizing solutal interfacial tension gradient and stabilizing dynamic viscosity and mass diffusion is represented by a solutal Marangoni number given by,

$$\mathrm{Ma}_{\omega} = \frac{\gamma_{\omega} d}{\mu D_{AB}} \tag{1–4}$$

Here;

γ_{ω}: Change in the interfacial tension with respect to the concentration.

Also in solutal Marangoni number, like in solutal Rayleigh number there is no ΔC term and it is also the upper bound. If the heating arrangement were to be reversed, i.e. heating from the liquid side, the solutal effects on the interfacial tension creates a stable system because this time the flow would take place from crest to the trough, dragging hot liquid to the cold crest and re-establishing the temperature uniformity. It is important

to point out again that the physical observation of solutal convection depends on the components that are used. If the more volatile component, in our case ethanol, were to be denser and had a higher interfacial tension than the second component, heating from the vapor side would be solutally stable as in the thermal problems.

Table 1-1. Summary table. (Thermal problem: Ther., Solutal problem: Sol., Unstable: Unst., Stable: Stab.)

	Pure Evaporation		Marangoni		Rayleigh	
	Ther.	Sol.	Ther.	Sol.	Ther.	Sol.
Heating from the Liquid side	Unst.	N/A	Unst.	Stab.	Unst.	Stab.
Heating from the Vapor side	Stab.	N/A	Stab.	Unst.	Stab.	Unst.

Although we have discussed different types of convection separately, in an experiment or application all three modes of convection would occur simultaneously, both solutally and thermally. However, by arranging the liquid height one can make the system Rayleigh or Marangoni dominant. The systems with deep liquids would be Rayleigh dominant because Rayleigh convection is proportional to the cube of the liquid depth, see equations (1–1) and (1–2). On the other hand, for shallow liquid depths the system would be Marangoni dominant simply because Marangoni convection is directly proportional to the liquid depth given in equations (1–3) and (1–4). For intermediate liquid depths, Rayleigh and Marangoni convection have similar effects on the system.

CHAPTER 2
LITERATURE REVIEW

Evaporation coupled with convection, which has many industrial applications, has been extensively investigated. Evaporative instability is a rich problem in many aspects and open to a detailed parametric study of the physical conditions and properties. Therefore, there might be various ways to analyze the literature. In this section we will present the literature dealing with a physical setup close to ours. Early works on this subject focused on single component systems with different aspects of the problem such as evaporation accompanied by only surface tension effects, passive vapor assumption, open or closed systems or experiments in either open or closed systems.

Pearson [1] gave the first theoretical analysis of the Marangoni convection using a methodology similar to that used by Rayleigh [2] for the case of buoyancy driven convection. Pearson's work was meant to describe Bénard's [3] experiment. He used the techniques of linearized stability cf. Chandrasekhar [4]. Although his work is not done for evaporative media the physics of Marangoni convection in non-evaporative systems is similar to Marangoni convection as it occurs in evaporative systems.

In evaporative systems the passive vapor model was used in the early works of Burelbach et al. [5] and recent works by Margerit et al. [6] and Oron [7]. In this type of model, a Biot number is defined to model the thermal resistance in the vapor behavior. The works that include fluid mechanics in the upper vapor phase are the works of Huang and Joseph [8], Ozen and Narayanan [9, 10], Haut and Colinet [11], McFadden et al. [12], and Guo and Narayanan [13].

The other point of interest in evaporative instability problems are the boundary conditions, specifically how the interface temperature conditions are introduced. Ordinarily, the continuity of temperature is used along with another thermodynamic equilibrium condition [8] or a relation derived from the kinetic theory is used instead [14]. Ward and Stanga [15] have questioned the assumption of continuity of temperature and

have verified the existence of a temperature discontinuity at the interface. Margerit et al. [16] studied the role of such interfacial non-equilibrium effects on Bénard-Marangoni instability. However, Ward and Stanga reported that the magnitude of the temperature discontinuity increases with the evaporation flux and noted that when equilibrium exists between the liquid and vapor phases, the temperature is same in each phase. This is also reported by Shankar and Deshpande [17]. Consequently, when the evaporation rate is very small we may assume that there is thermodynamic equilibrium at the phase-change boundary and the temperature of both fluids are equal to each other at the interface.

The works mentioned above focused on single component systems. Studies that include multi-component systems are limited compared to single component systems. de Gennes [18] worked on a scaling analysis for a solvent evaporation in non-glassy polymer. He showed that in the early times the convective instability rises due to concentration gradients and also concluded that concentration effects dominate the thermal effects. Trouette et al. [19] numerically investigated drying of a polymer/solvent solution at the thermal transient regime. They pointed out that the thresholds in the 2-D model and 3-D model′s are not very different from one another and convection cells are in the form of non-regular pentagons or hexagons with increasing size with time while convection fades away. Machrafi et al. [20, 21] numerically investigated the onset of the convection in a binary system consisting of ethanol and water. They showed that their system is dominated by the solutal Marangoni mechanism.

In addition to the theoretical works there are several experimental works done to show the instabilities in evaporating liquid layers. Mancini and Masa [22] worked on the pattern formation in an evaporating hexametildisiloxane liquid layer. They showed that if the evaporation rate is large enough there is no external heating needed to initiate the convection. The cooling of evaporation on the interface is sufficient enough to start convection for certain liquid heights. Also they showed the dynamic behavior of the

convection cells with respect to the liquid height. Zhang [23] studied convection in evaporating liquids such as ethanol and R-113 where R-113 is 10 times more volatile than ethanol. He showed that in thinner liquid layers, $1\ mm$ thick or less for ethanol and $0.5\ mm$ thick or less for R-113, Marangoni-Bénard convection is always dominant compared to Rayleigh-Bénard. There are also some experimental works done in binary systems, e.g. by Zhang et al. [24, 25] They first investigated the transient Marangoni convection in thin liquid films using solutions of NaCl-water and observed the patterns, consisting of rolls and polygons, evolving with time till drying and salt island occurrence. In the second study they chose ethanol and water system and observed circular ring type convection cells. Another experimental work is due to by Dehaeck et al. where they investigated the binary mixture evaporation and reported Rayleigh-Taylor type of instability due to density stratification [26]. Toussaint et al. did an experimental study of the drying of a polymer solution [27]. They concluded that for small initial thickness, convection occurs due to the surface tension effects and the life time of this convection is less than the thermal transient regime. On the other hand for larger thicknesses, convection lasts longer. Also, there is strong interaction between the convection and the skin formation on the interface.

CHAPTER 3
MATHEMATICAL MODEL

To capture the physics of the evaporative convection phenomena that is described in Chapter 1 a complete mathematical model must be developed and that is the objective of this chapter. The model we are going to use is a one dimensional model where we take into account of phases′ momentum dynamics, heat transfer, and mass transfer assuming all along that the interface deflects. The equations are represented in their scaled forms where we first introduce the domain equations in each phase then the top and bottom boundary conditions and finally, the interface conditions.

The instability occurs as convection cells and in mathematical terms arises from the nonlinearity of the system. This nonlinearity manifests itself via a cyclical dependence of the pressure, temperature, velocity, and mass fraction fields at the interface. For example, at the interface, the local temperature gradient creates a pressure gradient which in turn causes flow and also changes the concentration field. This flow will of course modify the temperature profile and will also modify the composition profile via convective transport. The cycle continues on with the temperature and the composition modifying the pressure field.

Another source of the nonlinearity is the interface position which depends upon the flow dynamics and vice versa. In fact the curvature of the interface is a nonlinear functional of its position. This nonlinearity is, however, not the essential one that governs the instability. Interface deflection is only one manifestation of the instability, the essential manifestation being the onset of flow from a quiescent state.

The nonlinear equations that model the physics may be scaled. We choose the liquid depth, d, as the length scale, κ/d as the velocity scale, d^2/κ as the time scale and $\mu\kappa/d^2$ as the pressure scale while the temperature is written as a deviation from T_{cold} and scaled by $T_{hot} - T_{cold}$. In the equations that will follow, asterisks denote the vapor phase and ρ, ν, κ, μ and D_{AB} are the density, the kinematic viscosity, the thermal

diffusivity, the dynamic viscosity and the mass diffusion. In the model, the fluid mixtures are taken to be ideal this is reasonable for the present example where the mixture made up of two low weight alcohols.

3.1 1-D Scaled Nonlinear Equations for the Binary System

The fluid flow in both phases is modeled using scaled Navier-Stokes equations or momentum balances. In the following momentum balance equations the densities are taken to be constant in all of the terms other than the terms multiplied by gravitational acceleration. This approach is called Boussinesq approximation and details are given in the Appendix B. This assumption is fair provided the temperature drop in the system is not very large and density is not a strong function of temperature.

The momentum balances for both phases using the Boussinesq approximation are given by,

$$\frac{1}{\mathrm{Pr}}\left(\frac{\partial \vec{v}}{\partial t}+\vec{v}\cdot\nabla\vec{v}\right)=-\nabla P+\nabla^2\vec{v}+Ra_T T\vec{k}+\frac{Ra_\omega}{Le}\left(\omega_A-\omega_{A_{ref}}\right)\vec{k} \tag{3–1}$$

and

$$\frac{\nu}{\nu^*}\frac{1}{\mathrm{Pr}}\left(\frac{\partial \vec{v}^*}{\partial t}+\vec{v}^*\cdot\nabla\vec{v}^*\right)=-\nabla P^*+\nabla^2\vec{v}^*+\frac{\beta_T^*}{\beta_T}\frac{\nu}{\nu^*}Ra_T T^*\vec{k}+\frac{\beta_\omega^*}{\beta_\omega}\frac{\nu}{\nu^*}\frac{Ra_\omega}{Le}\left(\omega_A^*-\omega_{A_{ref}}\right)\vec{k} \tag{3–2}$$

In the above, $\vec{k}$ is the unit vector in the positive z direction with $\omega_{A_{ref}}$ is the initial reference mass fraction. The dimensionless variables are; Prandtl number, $\mathrm{Pr}=\frac{\nu}{\kappa}$, thermal Rayleigh number, $Ra_T=\frac{\beta_T g\Delta T d^3}{\nu\kappa}$, solutal Rayleigh number, $Ra_\omega=\frac{\beta_\omega g d^3}{\nu D_{AB}}$ and the Lewis number, $Le=\frac{\kappa}{D_{AB}}$.

The flows in both phases are connected to temperature via the Ra_T term. In order to solve for the temperature profiles we need the energy balances in each phases. They are given by,

$$\frac{\partial T}{\partial t}+\vec{v}\cdot\nabla T=\nabla^2 T \tag{3–3}$$

and

$$\frac{\partial T^*}{\partial t} + \vec{v}^* \cdot \nabla T^* = \frac{\kappa^*}{\kappa} \nabla^2 T^* \tag{3–4}$$

Like the temperature dependence the flow also depends on the concentration field in each phase. In order to solve for the flow field we need to solve for the concentration field as well and for that we need the concentration balances in each phase, i.e.

$$\frac{\partial \omega_A}{\partial t} + \vec{v} \cdot \nabla \omega_A = \frac{1}{Le} \nabla^2 \omega_A \tag{3–5}$$

and

$$\frac{\partial \omega_A^*}{\partial t} + \vec{v}^* \cdot \nabla \omega_A^* = \frac{D_{AB}^*}{D_{AB}} \frac{1}{Le} \nabla^2 \omega_A^* \tag{3–6}$$

Finally we need to satisfy mass conversation in each phase by using the continuity equations, i.e., $\nabla \cdot \vec{v} = 0$ and $\nabla \cdot \vec{v}^* = 0$.

In the equations above,P is the scaled modified pressure where the modified pressure is equal to the scalar pressure, p, added to the density multiplied by the gravitational potential. The variables, $\vec{v}$ and T are the scaled modified pressure, velocity and temperature fields. The mass fraction of component A, ω_A, is already dimensionless. Note that in a binary mixture there are two components A and B where $\omega_A + \omega_B = 1$.

In order to solve the system of domain equations we need 16 boundary conditions and one additional condition to define the surface deflection.

The top and bottom walls are solid and impermeable with uniform temperature, i.e., at the bottom wall, $z = -d$, we have

$$v_z = 0, \frac{\partial \omega_\mathrm{A}}{\partial \mathrm{z}} = 0 \text{ and } T = T_{Bottom}$$

and at the top wall, $z = d^*$, we have

$$v_z{}^* = 0, \frac{\partial \omega_\mathrm{A}^*}{\partial \mathrm{z}} = 0 \text{ and } T^* = T_{Top}$$

No-slip conditions are assumed for the top and bottom walls. Therefore, at the bottom wall $v_x = 0$ and at the top wall ${v_x}^* = 0$.

The total mass balance at the interface, located at $z = Z(x, t)$, is

$$(\vec{v} - \vec{u}) \cdot \vec{n} = \frac{\rho^*}{\rho} (\vec{v}^* - \vec{u}) \cdot \vec{n} \tag{3–7}$$

and the component balance at the interface is

$$-\nabla\omega_A \cdot \vec{n} + Le\omega_A (\vec{v} - \vec{u}) \cdot \vec{n} = -\frac{\rho^*}{\rho} \left[-\frac{D^*_{AB}}{D_{AB}} \nabla\omega^*_A \cdot \vec{n} + Le\omega^*_A (\vec{v}^* - \vec{u}) \cdot \vec{n} \right] \tag{3–8}$$

Note that the mass flux, J_A, is given by $J_A = -\rho D_{AB} \nabla\omega_A$ is the mass flux.

The unit normal vector is,

$$\vec{n} = \frac{-\frac{\partial Z}{\partial x}\vec{i} + \vec{k}}{\left[1 + \left(\frac{\partial Z}{\partial x}\right)^2\right]^{1/2}}$$

The interface speed is,

$$\vec{u} \cdot \vec{n} = \frac{\frac{\partial Z}{\partial t}}{\left[1 + \left(\frac{\partial Z}{\partial x}\right)^2\right]^{1/2}}$$

At the interface the tangential components of the velocities of both fluids are equal to each other, i.e., $\vec{v} \cdot \vec{t} = \vec{v}^* \cdot \vec{t}$ hold where,

$$\vec{t} = \frac{\vec{i} + \frac{\partial Z}{\partial x}\vec{k}}{\left[1 + \left(\frac{\partial Z}{\partial x}\right)^2\right]^{1/2}}$$

Above $\vec{i}$ is the unit vector in the positive x direction. The derivations of the unit normal vector, interface speed, and the unit tangent is given in the Appendix D.

The interfacial force balance equation in scaled from is [28],

$$Ca_T \left[\frac{1}{\mathrm{Pr}} \vec{v} (\vec{v} - \vec{u}) - \frac{1}{\mathrm{Pr}} \frac{\rho^*}{\rho} \vec{v}^* (\vec{v}^* - \vec{u}) \right] \cdot \vec{n} - Ca_T Ma_T \nabla_s T t - Ca_\omega Ma_\omega \nabla_s \omega_A t + 2H\vec{n} = Ca_T \left(\vec{\vec{T}} - \vec{\vec{T}}^* \right) \cdot \vec{n} \tag{3–9}$$

where $2H = \frac{\frac{\partial^2 Z}{\partial x^2}}{\left[1+\left(\frac{\partial Z}{\partial x}\right)^2\right]^{3/2}}$ is twice the mean curvature, $\vec{\vec{T}} = -P\vec{\vec{I}} + \vec{\vec{S}}$ is the stress tensor, $Ca_T = \frac{\mu\kappa}{\gamma d}$ is a thermal capillary number, $Ma_T = \frac{\gamma_T d\Delta T}{\mu\kappa}$ is the thermal Marangoni number, $Ca_\omega = \frac{\mu D_{AB}}{\gamma d}$ is a solutal capillary number and $Ma_\omega = \frac{\gamma_\omega d}{\mu D_{AB}}$ is the solutal Marangoni number.

Observe that the force balance has two components, the normal and the tangential components.

The energy balance at the interface is [28]

$$\begin{aligned}\left\{1+K_{PC}\left[\frac{1}{2}\left(\vec{v}-\vec{u}\right)^2-\frac{1}{2}\left(\vec{v}^*-\vec{u}\right)^2\right]\right\}\left(\vec{v}-\vec{u}\right)\cdot\vec{n}+E_2\nabla\omega_A\\ -E_1\left(\nabla T\cdot\vec{n}-\frac{\lambda^*}{\lambda}\nabla T\cdot\vec{n}\right)-V_{PC}\left[\vec{\vec{S}}\cdot\left(\vec{v}-\vec{u}\right)-\frac{\mu^*}{\mu}\vec{\vec{S}}^*\cdot\left(\vec{v}^*-\vec{u}\right)\right]\cdot\vec{n}=0\end{aligned} \tag{3–10}$$

Here the dimensionless numbers are; $E_2 = D_{AB}\left(\hbar_A-\hbar_B\right)/\kappa\left(-\hbar_A\omega_A-\hbar_B\omega_B\right)$, $K_{PC} = \kappa^2/d^2\left(-\hbar_A\omega_A-\hbar_B\omega_B\right)$, $E_1 = \lambda\Delta T/\kappa\rho\left(-\hbar_A\omega_A-\hbar_B\omega_B\right)$, $V_{PC} = \nu\kappa/d^2\left(-\hbar_A\omega_A-\hbar_B\omega_B\right)$, λ is the thermal conductivity and $\hbar$ is the latent heat per unit mass.

At the interface the compositions of both phases are coupled with Raoult's law, i.e.,

$$y_A p = x_A P_A^{vap} \tag{3–11}$$

where y_A and x_A are vapor molar and liquid molar compositions.

In the closed system the local evaporation which takes place only upon perturbation is obtained from linearized stability and is assumed to be very small. Ward and Stanga [15] and Shankar and Deshpande[17] have shown that the temperature jump across the interface is very small if the evaporation rate is also small. Small evaporation rates at the interface allow us to assume continuity of temperature, i.e., $T = T^*$ and also local thermodynamic equilibrium which leads to the Clausius-Clapeyron[8] equation, i.e.,

$$\prod_{KE}\left(p^*-p^*_{base}\right) = \ln\left(\frac{T^*}{T^*_{base}}\right) \tag{3–12}$$

where $\prod_{KE} = \frac{\rho}{\rho^*}\frac{\upsilon\kappa}{\hbar d^2}$, p^*_{base} and where T^*_{base} are the scaled interfacial pressure and temperature of the vapor at a reference state.

3.2 1-D The Scaled Linear Equations for the Binary System

To determine the stability of the system and the onset point of convection, requires linearization of the domain equations and boundary conditions about a base state [29]. The base state for our system is the no-flow conductive state. In order to study the stability of a reference state, arbitrary infinitesimal disturbances are applied to the domain state variables and the boundary variables. If the state is unstable to infinitesimal disturbances it must be unstable to all disturbances and so it is sufficient to consider infinitesimal disturbances. Thus, stability to small disturbance does not give any information of the system but instability does. Using small disturbances also allows us to drop terms with quadratic and higher interactions.

Hereon, the base state variables are denoted by subscript 0 and the variables of the perturbed state by the subscript 1. Any perturbed domain variable evaluated on the deflecting surface is give by,

$$U = U_0 + \varepsilon\left(U_1 + \frac{dU_0}{dz}z_1\right) + O\left(\varepsilon^2\right)$$

where ε is the arbitrary infinitesimal disturbance that represents the deviation from the base state and z_1 is the mapping of the perturbed state to the base state. The detailed explanation of the mapping is given in the Appendix K. At the interface the mapping is simply the perturbation of the surface deflection and at its first order it is termed, Z_1, a variable that also needs to be determined. The perturbed variables are assumed to either grow or decay as $e^{\sigma t}$, where σ is the inverse growth or decay constant hereafter termed as just the growth constant. The perturbed variables are further expanded into normal modes, thus

$$U_1 = \widehat{U}_1(z)e^{\sigma t}e^{ikx}$$

where k is the wave number of a given disturbance that arises because the system is infinite in lateral extent. The wave number can be related to the radius of the system if the sidewalls are assumed to have periodic boundary conditions.

As we mentioned above in the base state there is no flow, i.e. $\vec{v}_0 = 0 = \vec{v}^*$, and it has a simple conduction solution. The temperature profiles in both phases in their scaled form are given by

$$T_0 = -\frac{\lambda^*}{\lambda\delta + \lambda^*} z + \frac{\lambda\delta}{\lambda\delta + \lambda^*}$$

and

$$T_0^* = -\frac{\lambda}{\lambda\delta + \lambda^*} z + \frac{\lambda\delta}{\lambda\delta + \lambda^*}$$

where $\delta = d^*/d$ is the ratio of vapor to liquid depth. The linearized domain equations in the liquid phase become,

$$\frac{\sigma}{\mathrm{Pr}} v_{x1} = -ikp_1 + \left(\frac{d^2}{dz^2} - k^2\right) v_{x1} \tag{3–13}$$

$$\frac{\sigma}{\mathrm{Pr}} v_{z1} = -\frac{dp_1}{dz} + \left(\frac{d^2}{dz^2} - k^2\right) v_{z1} + Ra_T T_1 + \frac{Ra_\omega}{Le}\omega_{A1} \tag{3–14}$$

$$\sigma T_1 = \left(\frac{d^2}{dz^2} - k^2\right) T_1 - \frac{dT_0}{dz} v_{z1} \tag{3–15}$$

$$\sigma\omega_{A1} = \frac{1}{Le}\left(\frac{d^2}{dz^2} - k^2\right)\omega_{A1} \tag{3–16}$$

and

$$0 = ikv_{x1} + \frac{dv_{z1}}{dz} \tag{3–17}$$

Like wise for the vapor phase we have

$$\frac{\sigma}{\mathrm{Pr}}\frac{\nu}{\nu^*} v_{x1}^* = -ik\frac{\mu}{\mu^*} p_1^* + \left(\frac{d^2}{dz^2} - k^2\right) v_{x1}^* \tag{3–18}$$

$$\frac{\sigma}{\mathrm{Pr}}\frac{\nu}{\nu^*}v_{z1}^* = -\frac{\mu}{\mu^*}\frac{dp_1^*}{dz} + \left(\frac{d^2}{dz^2} - k^2\right)v_{z1}^* + \frac{\nu}{\nu^*}\frac{\beta_T^*}{\beta_T}Ra_T\,T_1^* + \frac{\nu}{\nu^*}\frac{\beta_\omega^*}{\beta_\omega}\frac{Ra_\omega}{Le}\omega_{A1}^* \tag{3–19}$$

$$\sigma\omega_{A1}^* = \frac{1}{Le}\frac{D_{AB}^*}{D_{AB}}\left(\frac{d^2}{dz^2} - k^2\right)\omega_{A1}^* \tag{3–20}$$

and

$$0 = ikv_{x1}^* + \frac{dv_{z1}^*}{dz} \tag{3–21}$$

At the lower plate, $z = -1$, we have

$$v_{x1} = v_{z1} = T_1 = \frac{d\omega_{A1}}{dz} = 0$$

and at the top plate, $z = \delta$, we have

$$v_{x1}^* = v_{z1}^* = T_1^* = \frac{d\omega_{A1}^*}{dz} = 0$$

At the interface, the mass balance and component balance turn into,

$$v_{z_1} - \frac{\rho^*}{\rho}v_{z_1}^* = \sigma\left(1 - \frac{\rho^*}{\rho}\right)Z_1 \tag{3–22}$$

and

$$-\frac{d\omega_{A1}}{dz} + \frac{\rho^*}{\rho}\frac{D_{AB}^*}{D_{AB}}\left(\frac{d\omega_{A1}^*}{dz}\right) + Le\left(\omega_{A0}v_{z1} - \frac{\rho^*}{\rho}\omega_{A0}^*v_{z1}^*\right) = \sigma Le\left(\frac{\rho^*}{\rho}\omega_{A0}^* - \omega_{A0}\right)Z_1 \tag{3–23}$$

where Z_1 is the perturbed surface deflection and ω_{A0} is the initial mass fraction at the base state.

The continuity of temperature and the no-slip conditions become

$$T_1 + \frac{dT_0}{dz}Z_1 = T_1^* + \frac{dT_0^*}{dz}Z_1 \tag{3–24}$$

and

$$v_{x1} = v_{x1}^* \tag{3–25}$$

The linearized equations for the tangential and normal stress are given by,

$$\frac{\mu^*}{\mu}\left(\frac{dv_{x1}^*}{dz}+ikv_{z1}^*\right)-\left(\frac{dv_{x1}}{dz}+ikv_{z1}\right)-ikMa_T\left(T_1+\frac{dT_0}{dz}Z_1\right)-ikMa_\omega\omega_{A1}=0 \quad (3\text{–}26)$$

and

$$Ca\left(p_1-p_1^*\right)-2Ca\left(\frac{dv_{z1}}{dz}-\frac{\mu^*}{\mu}\frac{dv_{z1}^*}{dz}\right)-\left(Bo+k^2\right)Z_1=0 \quad (3\text{–}27)$$

Here $Bo=\left[\left(\rho-\rho^*\right)gd^2\right]/\gamma$ is the Bond number.

The interfacial energy balance in its linear form given by,

$$v_{z1}+E_2\frac{d\omega_{A1}}{dz}-E_1\left(\lambda\frac{dT_1}{dz}-\lambda^*\frac{dT_1^*}{dz}\right)=\sigma Z_1 \quad (3\text{–}28)$$

Upon perturbation Raoult's law becomes,

$$\begin{aligned}\left[\left(\frac{dP_A^{\mathrm{Vap}}}{dT}\right)_{T=T_0}\left(x_{A_0}y_{A_0}-x_{A_0}\right)+\left(\frac{dP_B^{\mathrm{Vap}}}{dT}\right)_{T=T_0}\left(y_{A_0}-x_{A_0}y_{A_0}\right)\right]\left(T_1+\frac{dT_0}{dz}Z_1\right)\\+\left[P_{A_0}^{\mathrm{Vap}}\left(y_{A_0}-1\right)-P_{B_0}^{\mathrm{Vap}}y_{A_0}\right]x_{A_1}+\left[P_{A_0}^{\mathrm{Vap}}x_{A_0}+P_{B_0}^{\mathrm{Vap}}\left(1-x_{A_0}\right)\right]y_{A_1}=0\end{aligned} \quad (3\text{–}29)$$

And the coefficients y_{A1} and x_{A1} are given by,

$$x_{A_1}=\left[\frac{M_B}{\omega_{A_0}\left(M_B-M_A\right)+M_A}-\frac{\omega_{A_0}M_B\left(M_B-M_A\right)}{\left(\omega_{A_0}\left(M_B-M_A\right)+M_A\right)^2}\right]\omega_{A_1}$$

and

$$y_{A_1}=\left[\frac{M_B}{\omega_{A_0}^*\left(M_B-M_A\right)+M_A}-\frac{\omega_{A_0}^*M_B\left(M_B-M_A\right)}{\left(\omega_{A_0}^*\left(M_B-M_A\right)+M_A\right)^2}\right]\omega_{A_1}^*$$

The remaining condition, i.e., the Clausius-Clapeyron in its linearized from is

$$\prod\nolimits_{KE}p_1^*-\prod\nolimits_{PE}Z_1=\frac{T_1^*+\left(\frac{dT_0^*}{dz}\right)Z_1}{T_0^*} \quad (3\text{–}30)$$

In unscaled terms, the inputs to the calculation aside of the fluid thermo-physical properties, depths, and disturbance wave number k, are the composition of the liquid phase of the binary mixture in the rest state, ω_{A0} and ΔT, the temperature drop across

the bilayer. The output variable is the growth constant, σ. This constant appears in several places, in the domain equations for momentum, energy, and species continuity as well as at the interface on account of overall mass balance, Eq. 3–22, the component balance, Eq. 3–23, and the energy balance, Eq. 3–28. A Chebyshev spectral collocation method, wherein the dependent variables are expanded in terms of polynomials, leads to a generalized eigenvalue problem with σ as the eigenvalue.[30] Calculations reveal that the values of the leading σ are always real, no matter if the ΔT is positive or negative. As our interest is in determining the onset condition for the instability we set σ to zero and calculate the critical ΔT in its scaled form. In this case the scaled critical ΔT becomes the eigenvalue and because it appears linearly in the dimensionless groups Ma_T and E_1, its computation is non-iterative i.e., explicit.

3.3 Numerical Method

The spectral method approximates the solution of a differential equation as continuous functions, resulting in a global solution. In our work, we use the spectral method with Chebyshev grid points to solve coupled partial differential equations consisting of momentum, energy, and concentration fields in two phases [30]. Consider a function $u(x)$, which is a solution to a differential equation. The goal of the Spectral Chebyshev method is to provide a polynomial $u^{(N)}(x)$ which approximates the solution $u(x)$ depending on the number of terms N taken. The first step of the Spectral Chebyshev method is to define the grid points, which will be used to create differentiation matrices.

The best way of describing the differentiation matrix is through an example. Lets discretize $\frac{d}{dx}$ with x defined over $[-1, 1]$. We first need to decide the number of intervals N corresponding to $N + 1$ number of grids points. Let us illustrate this with $N = 2$, i.e., we define three grid points located at $x_0 = -1, x_1 = 0, x_2 = 1$ where $u(x)$ is evaluated. Then, $u(x)$ is approximated with a quadratic polynomial.

$$u(x) \approx u^{(2)}(x) = a(x - x_0)(x - x_1) + b(x - x_1)(x - x_2) + c(x - x_2)(x - x_0) \quad (3\text{–}31)$$

u_0, u_1, and u_2 can be written as

$$u_0 = u(x_0) = b(x_0 - x_1)(x_0 - x_2) \tag{3–32}$$

$$u_1 = u(x_1) = c(x_1 - x_2)(x_1 - x_0) \tag{3–33}$$

$$u_2 = u(x_2) = a(x_2 - x_0)(x_2 - x_1) \tag{3–34}$$

From this set of equations a, b, and c are obtained in terms of u_0, u_1, and u_2 as $a = \frac{u_2}{2}$, $b = \frac{u_0}{2}$ and $c = -u_1$. The derivative of $u^{(2)}(x)$,

$$\frac{du^{(2)}}{dx} = 2x(a + b + c) - [a(x_0 + x_1) + b(x_1 + x_2) + c(x_2 + x_0)] \tag{3–35}$$

$$\left.\frac{du}{dx}\right|_{x=x_0} = -1.5u_0 + 2u_1 - 0.5u_2$$

$$\left.\frac{du}{dx}\right|_{x=x_1} = -0.5u_0 + 0.5u_2 \tag{3–36}$$

$$\left.\frac{du}{dx}\right|_{x=x2} = 0.5u_0 - 2u_1 + 1.5u_2$$

This equation set can be represented in matrix form as $\underline{\underline{A}}\underline{u} = \underline{b}$, where $\underline{\underline{A}}$ is the differentiation matrix.

$$\begin{vmatrix} -1.5 & 2 & -0.5 \\ -0.5 & 0 & 0.5 \\ 0.5 & -2 & 1.5 \end{vmatrix} \begin{vmatrix} u_0 \\ u_1 \\ u_2 \end{vmatrix} = \begin{vmatrix} du_0/dx \\ du_1/dx \\ du_2/dx \end{vmatrix} \tag{3–37}$$

To obtain the 2^{nd} and 3^{rd} order derivative matrices, we can simply take the 2^{nd} and 3^{rd} power of the differentiation matrix.

$$\frac{d^2u^{(2)}}{dx^2} = 2(a + b + c) = u_0 - 2u_1 + u \tag{3–38}$$

Observe that the second derivative does not depend on the position, so the second derivative is same at every position and the second order differentiation matrix is given by,

$$\begin{vmatrix} 1 & -2 & 1 \\ 1 & -2 & 1 \\ 1 & -2 & 1 \end{vmatrix} \tag{3–39}$$

One can get the same matrix by simply taking 2^{nd} power of 1^{st} order differentiation matrix. Note that you cannot use $N = 1$ for solving a 2^{nd} order differential equation because the second power of differentiation matrix turns out to be zero.

This method works over the interval $[-1, 1]$ because the nodes are defined by using cosines function. If the domain is defined in another interval, the differentiation matrix should be multiplied by a linear transformation coefficient.

As an example, imagine that the domain lies between 0 and L. The linear transformation coefficient calculation goes as follows; $x' = Ax + B$ is the linear function which connects your domain to spectral interval, where x' is the spectral interval and x is your domain. When $x = 0 \rightarrow x' = -1$ and $x = L \rightarrow x' = 1$

$$-1 = B$$

$$1 = A \cdot L - 1 \rightarrow A = \frac{2}{L}$$

It is clear that $A\frac{d}{dx'} = \frac{d}{dx}$, so A is the linear transfer coefficient which is $\frac{2}{L}$ in the sample calculation.

Chebyshev Gauss-Lobatto nodes are defined for N number of subintervals over range $[-1, 1]$;

$$x_j = -\cos\left(j\frac{\pi}{N}\right), \mathrm{j} = 0,\ldots,\mathrm{N} \tag{3–40}$$

Note that the grid points are not equally spaced. The nodes are denser near to the boundaries. This has advantage on capturing boundary effects on the domain, which is important for transport phenomena problems. Two examples of how grids look like for different points are given in Figure 3-1;

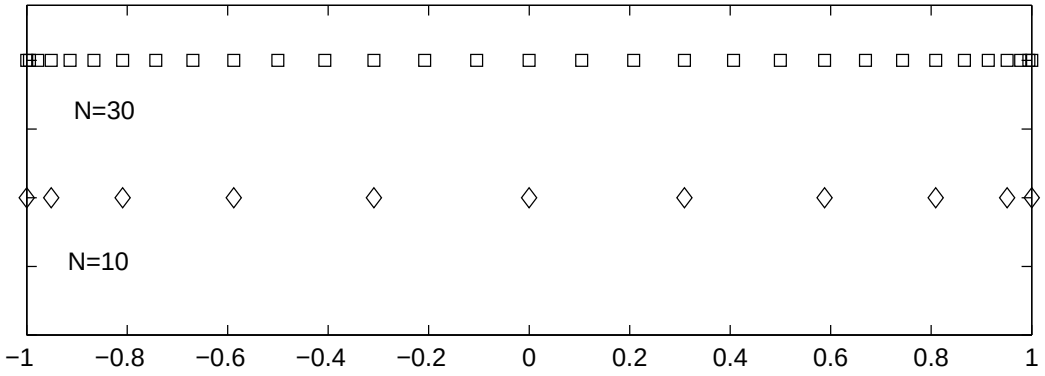

Figure 3-1. Grid points for Gauss-Labotto representation.

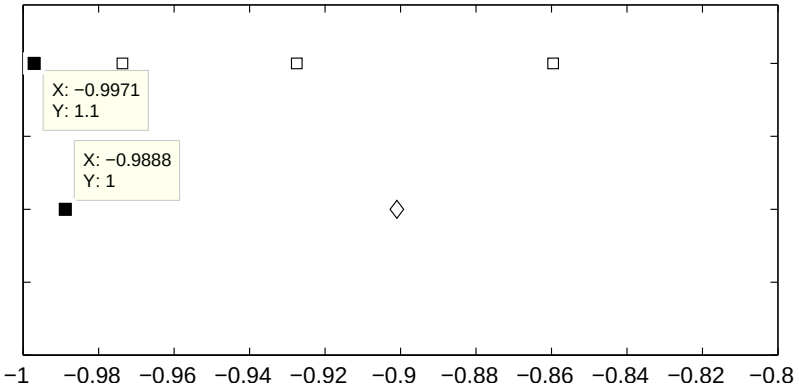

Figure 3-2. Grid points for Gauss-Radau representation.

A different type of grid points structure needs to define for a cylindrical coordinate system because of the singularity that occurs in the operator at the centerline position, $r = 0$. In order to overcome this problem Gauss-Radau grid points have to be introduced seen in Figure 3-2. In the Gauss-Labotto structure both boundaries of the system are included to the model. On the other hand in the Gauss-Radau nodes $r = 0$ point is excluded from the system. In Gauss-Radau structure there is a node close to centerline

position $(r = 0)$ which with increasing node numbers gets closer to $r = 0$ point but never reaches. The grid points are defined as,

$$x_p = -\cos\left(\frac{(2p+1)\,\pi}{2N+1}\right), p = 0, ..., N \tag{3–41}$$

The right boundary node for $p = N$ is $x_p = 1$, but the left one depends on N for example; for $N = 10$, $x_p = -0.9888$ and for $N = 20$, $x_p = -0.9970$. This is shown in Figure 3-2.

$$\frac{d^2 u^{(2)}}{dx^2} = 2(a + b + c) = u_0 - 2u_1 + u \tag{3–42}$$

In order to solve that the set of the equations, the differentiation matrix has to be inverted. However, the determinant of the A matrix is zero, so the A matrix cannot be inverted. Indeed, if the A matrix was invertible it would mean that we can solve a differential equation without boundary conditions. For solving the differential equation, the matrix A should be modified by inserting the proper boundary conditions.

To show how the spectral method is employed for solving a differential equation the following example is used where $\frac{d^2 U}{dx^2} = f$ is solved for known field of U. This know field U is given by

$$U = x^5 + 2\,x^3 - 2\,x^2 \tag{3–43}$$

and it is second derivative given by,

$$\frac{d^2 U}{dx^2} = f = 20\,x^3 + 12\,x - 4$$

To get an accurate derivative of the test function U, the cut-off must match the order of the function, i.e. 5^{th}, the spectral derivative matrix[30] is given below.

$$\begin{bmatrix} -8.5000 & 10.4721 & -2.8944 & 1.5279 & -1.1056 & 0.5000 \\ -2.6180 & 1.1708 & 2.0000 & -0.8944 & 0.6180 & -0.2764 \\ 0.7236 & -2.0000 & 0.1708 & 1.6180 & -0.8944 & 0.3820 \\ -0.3820 & 0.8944 & -1.6180 & -0.1708 & 2.0000 & -0.7236 \\ 0.2764 & -0.6180 & 0.8944 & -2.0000 & -1.1708 & 2.6180 \\ -0.5000 & 1.1056 & -1.5279 & 2.8944 & -10.4721 & 8.5000 \end{bmatrix}$$

Second order spectral matrix, $\frac{d^2}{dx^2}$, is given by,

$$\begin{bmatrix} 41.6000 & -68.3607 & 40.8276 & -23.6393 & 17.5724 & -8.0000 \\ -21.2859 & -31.5331 & 12.6833 & -3.6944 & 2.2111 & -0.9528 \\ -1.8472 & -7.3167 & -10.0669 & 5.7889 & -1.9056 & 0.7141 \\ 0.7141 & -1.9056 & 5.7889 & -10.0669 & 7.3167 & -1.8472 \\ -0.9528 & 2.2111 & -3.6944 & 12.6833 & -31.5331 & 21.2859 \\ -8.0000 & 17.5724 & -23.6393 & 40.8276 & -68.3607 & 41.6000 \end{bmatrix}$$

Applying the second order spectral matrix to the function U we obtain, spectrally, f and that is shown in Figure 3-3 with crosses. The solid line in Figure 3-3 shows the analytical solution and the sub-figure shows the relative difference between the analytical solution. The relative difference between the spectral and analytical solution is of the order of computational noise.

To show the effect of cut-off on the solution, two cases are shown in Figure 3-4 one for cut-off 4 and the other for 6. It is clear from Figure 3-4b decreasing the cut-off to 4 decreases the convergence substantially where increasing does not affect it.

In the current problem the modeling set of equations are discretized and represented as eigenvalue problem in the form of

$$\underline{\underline{A}}(\Delta T)\, u = \sigma \underline{\underline{B}} u \tag{3–44}$$

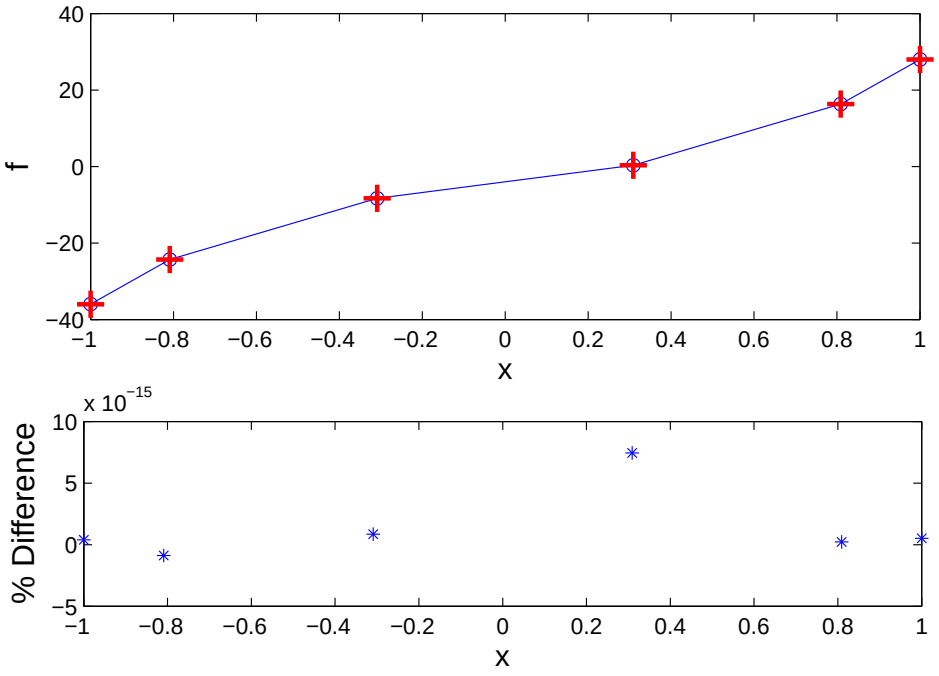

Figure 3-3. Spectral second derivative versus analytical second derivative. (Subplot shows the relative difference)

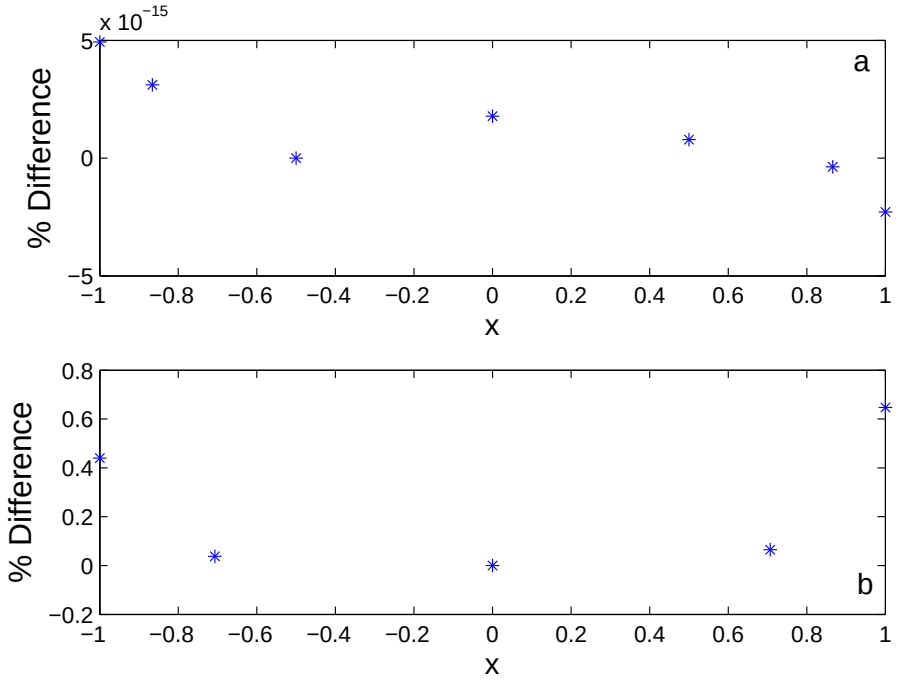

Figure 3-4. Effect of cut-off on the solution.

- $\underline{\underline{A}}$ and $\underline{\underline{B}}$ are found by the discretization of the governing equations, consists of spectral differentiation matrices, and the boundary conditions.
- u is the eigenvector of the problem which includes the velocity, temperature, and concentration fields.
- σ is the eigenvalue of the problem in our case is the growth constant.

Inputs to the computation besides the fluid thermo-physical properties, depths and the disturbance wave number k, are the composition of the liquid phase of the binary mixture in the rest state and ΔT, the temperature drop across the bilayer. The output variable is the growth constant, σ. Calculations reveal that the value of the leading σ are always real, no matter if the ΔT is positive or negative. As our interest is in determining the onset condition for the instability we set σ to zero and determine the critical ΔT in its scaled form. Also several σ calculations are given in the results and discussion section.

CHAPTER 4
RESULTS AND DISCUSSIONS

In this chapter we discuss the solutions of the linearized equations that were given in chapter 3 for a one-dimensional (1-D) model, titled Mathematical Model, as well as in the Appendix for a three-dimensional (3-D) model. The calculations are presented first for the 3-D model for a single component system in order to show the effect of the sidewalls on the system. The 3-D modeling equations are given in the Appendix H. We will then briefly introduce the effect of the non-constant viscosity for the single component system, again for the 3-D model. The modified modeling equations for the non-constant viscosity case are given in the Appendix I. In the last part of this section we will discuss, in great detail, 1-D binary system results.

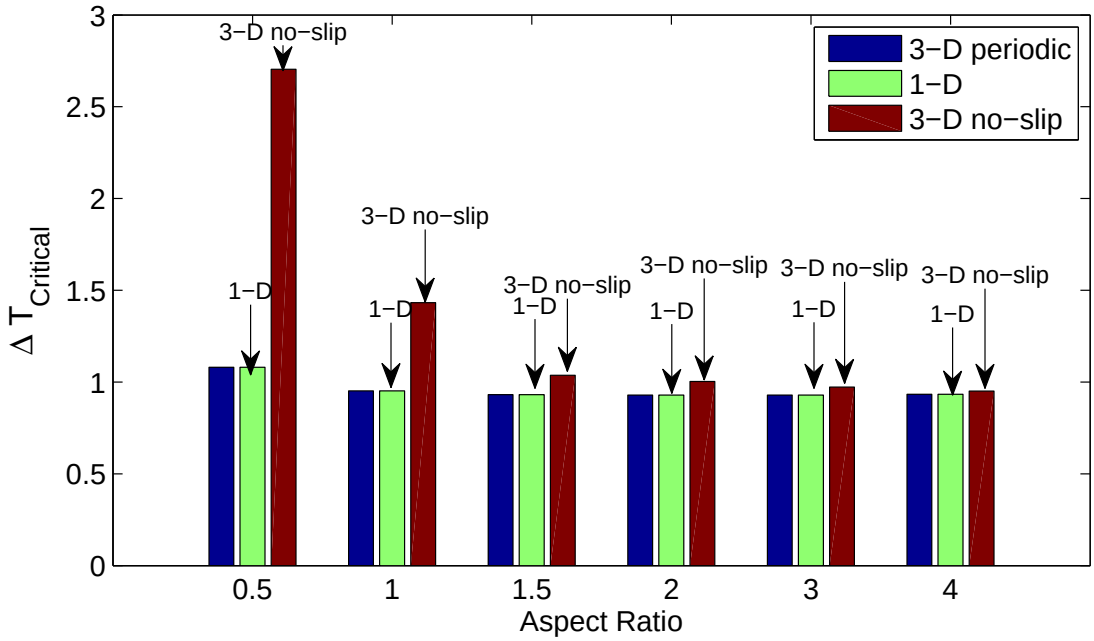

Figure 4-1. Effect of sidewall boundary conditions, aspect ratio, the onset of instability for liquid height=5 mm and vapor height=5 mm. (Bars without label: 3-D periodic system)

4.1 Effect of the Sidewall Conditions in the Single Component System

Investigating an instability problem in the presence of phase change involves heat transfer and fluid dynamics in addition to the complications that arise from the geometry,

as well as mass transfer for multi-component systems. In this section we investigate the sidewall effect on the onset for single component systems where evaporation is accompanied by surface tension gradient and density gradient effects. In order to have a better understanding of the physics a step by step approach is taken in this study. Thus, three different codes were developed, a 1-D code, a 3-D code with periodic sidewall conditions, and a 3-D code with no-slip sidewall conditions.

Table 4-1. Physical properties of liquid ethanol and sec-butanol and $50/50$ liquid weight percent binary liquid mixture at $30°\mathrm{C}$ and 1 atm.

	Ethanol	sec-Butanol	$50/50$ *mix.*
$\rho(\frac{\mathrm{kg}}{\mathrm{m}^3})$	782	800	791
$\mu(\frac{\mathrm{kg}}{\mathrm{m\ sec}})$	9.50×10^{-4}	2.74×10^{-3}	1.52×10^{-3}
$\lambda(\frac{\mathrm{J}}{\mathrm{m\ sec\ °C}})$	1.69×10^{-1}	1.34×10^{-1}	1.46×10^{-1}
$\kappa(\frac{\mathrm{m}^2}{\mathrm{sec}})$	9.20×10^{-8}	6.20×10^{-8}	7.45×10^{-8}
$\hbar(\frac{\mathrm{J}}{\mathrm{kg}})$	8.80×10^{5}	6.63×10^{5}	7.92×10^{5}
$\gamma(\frac{\mathrm{N}}{\mathrm{m}})$	2.27×10^{-2}	2.37×10^{-2}	2.31×10^{-2}
$\gamma_T(\frac{\mathrm{N}}{\mathrm{m°C}})$	9.60×10^{-5}	9.60×10^{-5}	9.60×10^{-5}
$\beta_T(\frac{1}{°\mathrm{C}})$	1.20×10^{-3}	1.20×10^{-3}	1.20×10^{-3}
$\gamma_\omega(\frac{\mathrm{N}}{\mathrm{m}\omega})$	N/A	N/A	8.50×10^{-4}
$\beta_\omega(\frac{1}{\omega})$	N/A	N/A	2.18×10^{-2}

The periodic 3-D code is an intermediate step between the 1-D code and the 3-D code with a no-slip sidewall condition. The periodic code is expected to give the same results as in the 1-D code on account of a separation of variables that arises thanks to stress-free sidewall conditions. This makes it easier to check the 3-D code and also gives us confidence in our codes.

A simple derivation on how we may compare the 3-D periodic code with the 1-D code is given in Appendix J. In this section only the results of those comparisons are given. Ethanol is used as an example of the media and the properties of ethanol for liquid and vapor phase are given in the Tables 4-1 and 4-2 [31].

Table 4-2. Physical properties of ethanol and sec-butanol vapors and $50/50$ liquid weight percent binary vapor mixture at $30^{\circ}\mathrm{C}$ and 1 atm.

	Ethanol	sec-Butanol	$50/50 mix.$
$\rho^*(\frac{\mathrm{kg}}{\mathrm{m}^3})$	1.88	3.03	2.15
$\mu^*(\frac{\mathrm{kg}}{\mathrm{m\ sec}})$	0.9×10^{-5}	0.75×10^{-5}	0.87×10^{-5}
$\lambda^*(\frac{\mathrm{J}}{\mathrm{m\ sec\ ^{\circ}C}})$	1.6710^{-2}	1.4410^{-2}	1.6210^{-2}
$\kappa^*(\frac{\mathrm{m}^2}{\mathrm{sec}})$	6.13×10^{-6}	3.08×10^{-6}	5.14×10^{-6}
$\beta_T^*(\frac{1}{^{\circ}\mathrm{C}})$	3.56×10^{-3}	3.40×10^{-3}	3.53×10^{-3}
$\beta_\omega^*(\frac{1}{\omega})$	N/A	N/A	0.53

The comparison is given for a liquid height of $5\ mm$ and a vapor height of $5\ mm$ for various aspect ratios in Figure 4-1. Observe that by keeping the liquid height fixed at $5\ mm$ the only way to change the aspect ratio is through increasing the radius of the system. The first thing to notice is that the 3-D periodic calculations and 1-D calculations give the same results as expected. On the other hand, the 3-D calculations with no-slip

conditions give a higher critical temperature difference than what is obtained from the other two calculations. This is also an expected result because no-slip side walls stabilize the system against convection. However, with increasing aspect ratio, i.e. larger radii, the effect of the side wall gets weaker and all three cases converge to the same result. Another point that requires attention is that with increasing aspect ratio the difference between the onset points of any two successive aspect ratios gets smaller. This supports the fact that for large enough containers the system is dominated by the heights and not by the radius.

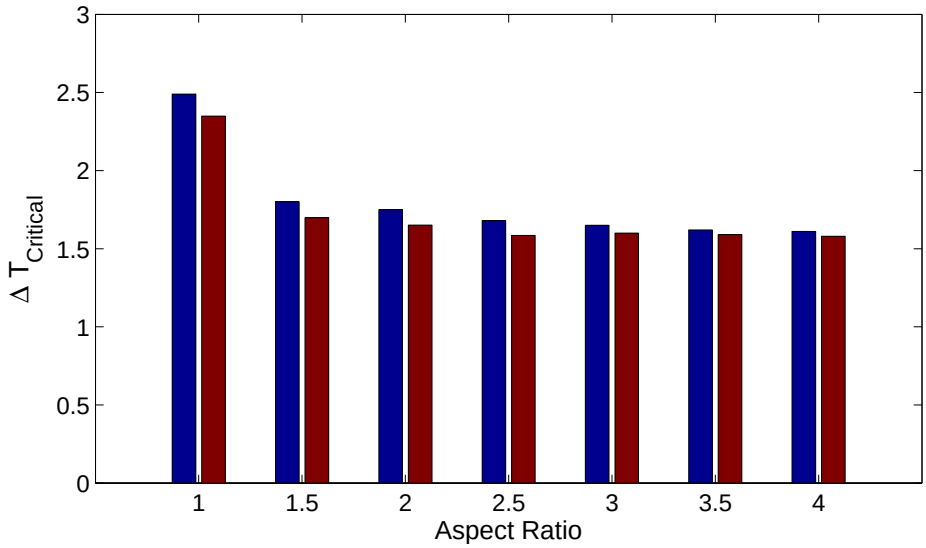

Figure 4-2. Non-constant viscosity vs. constant viscosity for liquid height=$5\ mm$ and vapor height=$9\ mm$. Columns on the left are the constant viscosity system.

4.2 3-D Non-Constant Viscosity Model for Single Component System

Previous calculations were done using constant thermo-physical properties, which are evaluated at the reference temperature for both liquid and vapor phases except in the case of the density where reference temperature is the cold plate temperature. In this section the results of non-constant viscosity, i.e. $\mu(T)$, model are compared with the constant viscosity results.

To go from a constant viscosity model to a non-constant viscosity model we have to modify the momentum balances in both phases as well as the force balances at the

interface(see Appendix I). In the case of ethanol, viscosity is a non-linear function of temperature. However, for small enough temperature ranges such as between 30 and $40\ ^{\circ}C$ the viscosity can be represented as a linear function of temperature. Using a linear dependence instead of a nonlinear one considerably simplifies the coding and decreases the computation time by avoiding an iterative computation.

In the modified model the input viscosity is smaller than the constant viscosity model, resulting in a more unstable system for all aspect ratios as seen in Figure 4-2.

4.3 The Effect of a Second Volatile Component on the Onset Point, 1-D Binary System

In this section we will discuss the effect of a second component on the onset point using the 1-D model that is given in chapter 3. Presence of the second component considerably modifies the modeling equations and also the physics of the problem.
In order to have a better understanding of the convection physics in a binary system we continue with the step by step approach. We first investigate the pure evaporative convection, then the phase change problem accompanied by Marangoni flow and finally, as a last step, we add the effect of gravity.

The binary mixture onset point depends on several parameters such as the vapor and liquid heights, the disturbance wave number, and the mass fraction of the mixture. In the following sections the effects of all these parameters will be discussed. The results will mostly be given as scaled $\Delta T_{Critical}$ versus one of those parameters where the reference point of scaling is given in each plot. This representation is not usual for this type of work; however, in our case the thermo-physical properties of the liquid and vapor mixtures change with respect to initial the mass fraction. Therefore, presenting the results by a dimensionless number such as Rayleigh number or Marangoni number that contains thermo-physical properties would be misleading.

To investigate the physics of the binary system we consider two similar low-weight alcohols such as ethanol and sec-butanol, which allows us to assume an ideal mixture.

An ideal mixture is a mixture whose enthalpy of mixing is equal to zero. In other words, upon mixing the intermolecular attractions do not modify the properties compared to pure liquids. Also, an ideal mixture's vapor phase obeys Raoult's law. The mixture properties are typically calculated using simple mixing rules with respect to either mass or mole fraction. Where possible, empirical formulas documented in the literature were used such as for viscosities [32, 33] and thermal conductivities.[34] For reference purposes, densities, viscosities, thermal conductivities, and surface tension of the mixture are plotted with respect to mass fraction in the Appendix L.

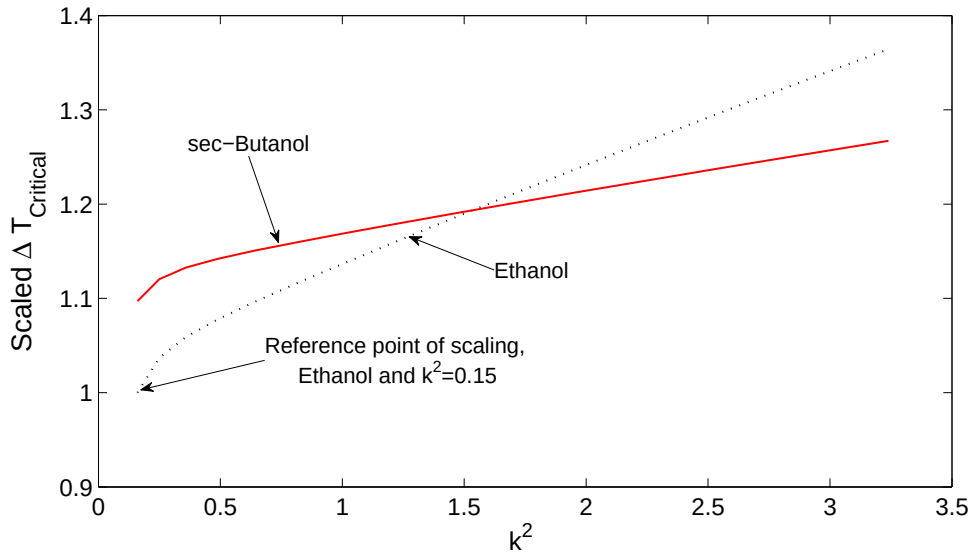

Figure 4-3. Onset of pure evaporative convection. Scaled $\Delta T_{Critical}$ vs. wave number, liquid height=2 mm and vapor height=1 mm.

4.3.1 Pure Evaporative Convection in Binary Mixtures

In this section we investigate the onset of convection in the absence of gravity and surface tension gradient effects. This type of convection is termed as "Pure Evaporative Convection" and its physics is described in Chapter 1, the Introduction of the Physics. Recall that pure evaporative convection occurs only if the heat is supplied from the liquid side, i.e., positive temperature differences.[9]

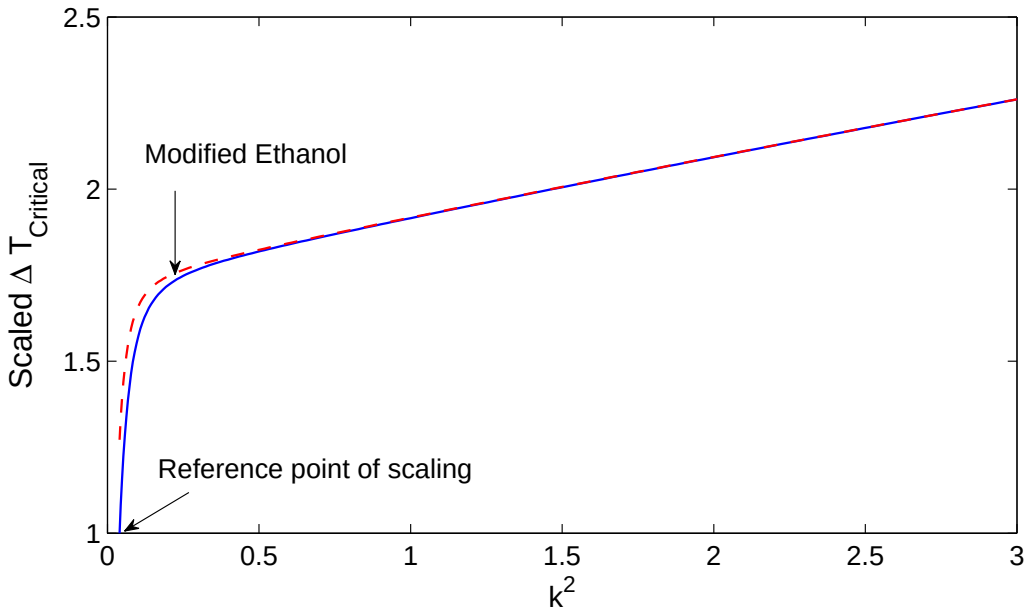

Figure 4-4. Effect of viscosity change on the onset of pure evaporative convection for ethanol, liquid height=2 mm and vapor height=1 mm.

In order to understand the effect of mass fraction on the system, we first need to investigate how the single component systems behave. We start by giving a comparison between the onset points of two pure components, i.e., pure ethanol and pure sec-butanol. Figure 4-3 depicts the onset point, given as scaled $\Delta T_{Critical}$, versus wave number of the disturbance for a liquid height of $2\ mm$ and for a vapor height of $1\ mm$. Both systems become more stable with increasing wave number as a result of increased thermal diffusion in smaller domains, that is, thermal diffusivity acts most strongly in smaller width containers or larger wave numbers due to the proximity of hot and cold regions.[35]

One can argue that viscosity may introduce some type of stability, too. To show that the stabilizing effect principally comes from thermal diffusion for large wave numbers let's take a little detour from Figure 4-3 and show the results of a numerical "experiment". In this numerical experiment we deliberately decrease the viscosity of ethanol by 50% (call it modified ethanol). In Figure 4-4 the results of modified ethanol are compared with

the ethanol of “real” properties. It is clear that changing the viscosity changes the onset point only in the small wave number region and this change is minimal.

Now let’s go back to Figure 4-3, the second point that has to be made is the cross-over between ethanol’s and sec-butanol’s onset points. Although both pure components become more stable with increasing wave number, the rate of stabilization is not equal to each other. This is due to the different thermal diffusivities of ethanol and sec-butanol. Ethanol, which has the larger thermal diffusivity, gets more stable compared to sec-butanol in the large wave number region. The presence of a cross-over has non-trivial consequences in the binary system.

Due to the cross-over seen in Figure 4-3, the pure evaporative instability of a binary mixture of ethanol and sec-butanol exhibits three different behaviors. They are shown in Figures 4-5(a) and 4-5(b) and will be discussed momentarily. Once again the ordinate is expressed by dividing the $\Delta T_{Critical}$ for each input mass fraction by the $\Delta T_{Critical}$ for pure ethanol at a given wave number. In Figure 4-5(a) the behavior of the onset point, $\Delta T_{Critical}$, for a binary alcohol mixture for pure evaporative convection is drawn against the mass fraction, with wave number as a free parameter. It is clear that for either small or large wave numbers the curves are monotonic and understandably they either increase or decrease in slope depending on the wave number, small or large. Observe that the points on the extreme left of Figure 4-5(a), pure sec-butanol points, can be read off from Figure 4-3. What is not apparent from Figure 4-5(a) is the effect of the cross-over point seen in Figure 4-3. This is made more transparent in Figure 4-5(b). Here, a weak maximum is seen to occur in the middle range of wave numbers close to the cross over point.

In order to investigate the effect of vapor and liquid heights on the onset point, several calculations are done and shown in Figure 4-6 for a fifty-fifty mass fraction. It is concluded that by increasing the vapor height the system becomes more stable due to increase in vapor flow from trough to crest. This flow brings in warm vapor to the cold

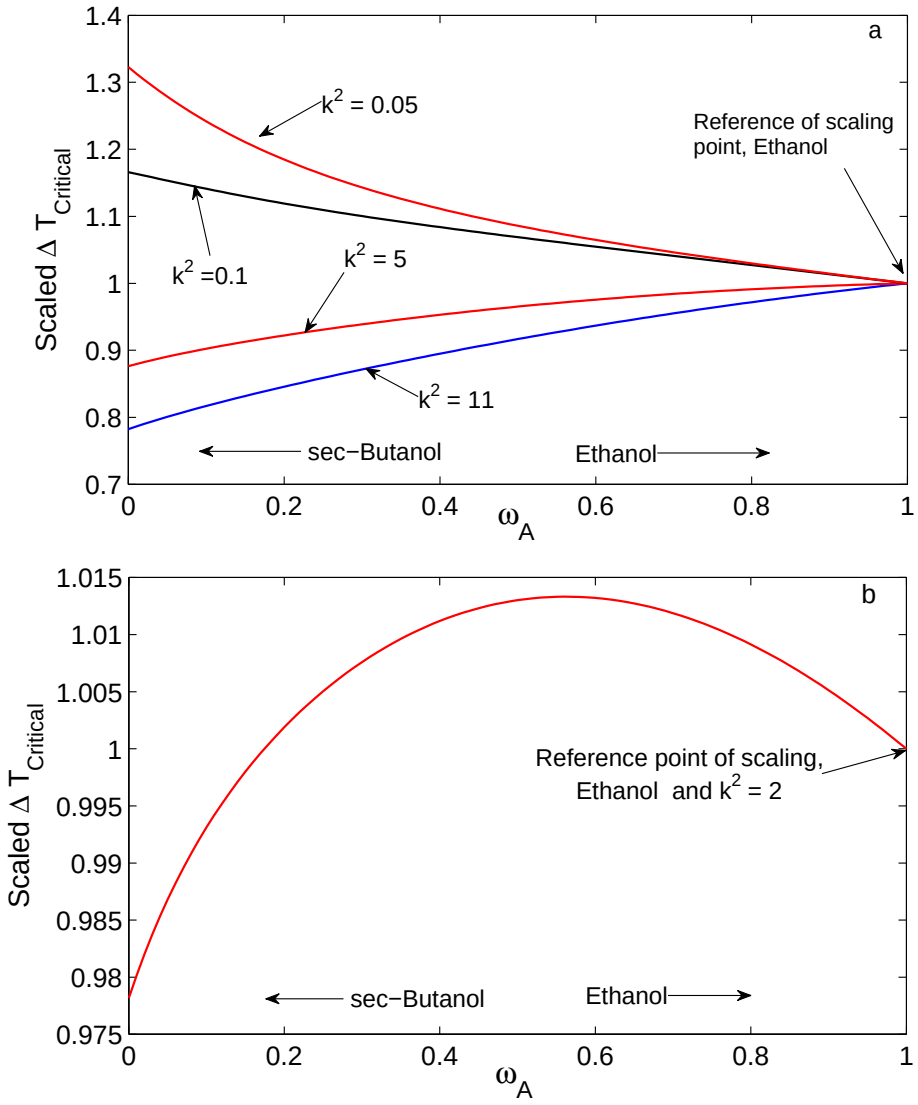

Figure 4-5. Binary mixture pure evaporative convection. Scaled $\Delta T_{Critical}$ vs. mass fraction, liquid height=$2\ mm$ and vapor height=$1\ mm$ (a) Small and large wave numbers (b) Maximum stability depicted for a middle range wave number.

crest and helps to reestablish the temperature uniformity. This behavior occurs for all mass fractions. Conversely, increased liquid heights create a more unstable system due to increased hot upward flow toward the troughs and downward flow from the crests in the liquid phase. Both of these results are qualitatively similar to all mass fractions including single component evaporation.

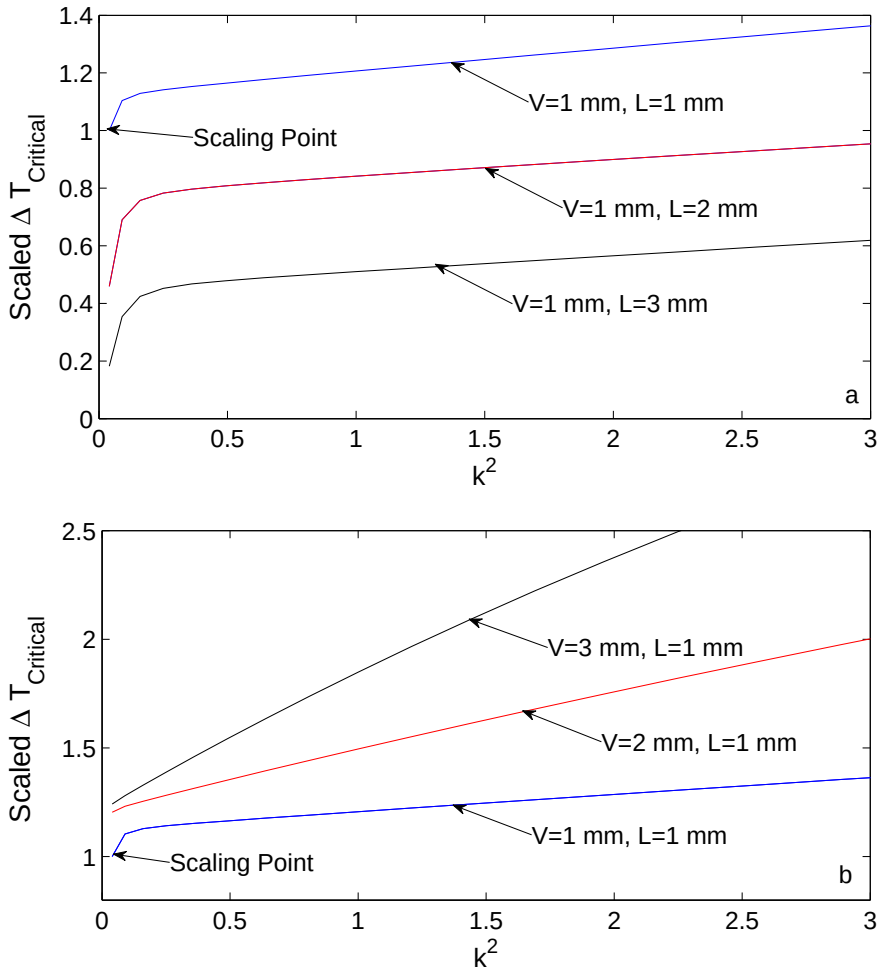

Figure 4-6. Onset of binary mixture pure evaporative convection. Scaled $\Delta T_{Critical}$ vs. k^2 wave number, (a) Effect of liquid height, vapor height=$1\ mm$ and $\omega_A = 0.5$ (b) Effect of vapor height, liquid height=$1\ mm$ and $\omega_A = 0.5$.

4.3.2 Surface Tension Driven Instability with Phase Change

In this section the additive effect of surface tension gradients on the onset of convection is investigated while still ignoring the gravity. This is plausible for small liquid and vapor depths or for systems in a micro-gravity environment. For the binary system surface tension depends on both concentration and temperature. The calculations show that the dependence of surface tension upon temperature is inconsequential in evaporation problems.[9] Recall that, in our physical setup, there is no external mass fraction gradient applied. The mass fraction gradient is induced by the different

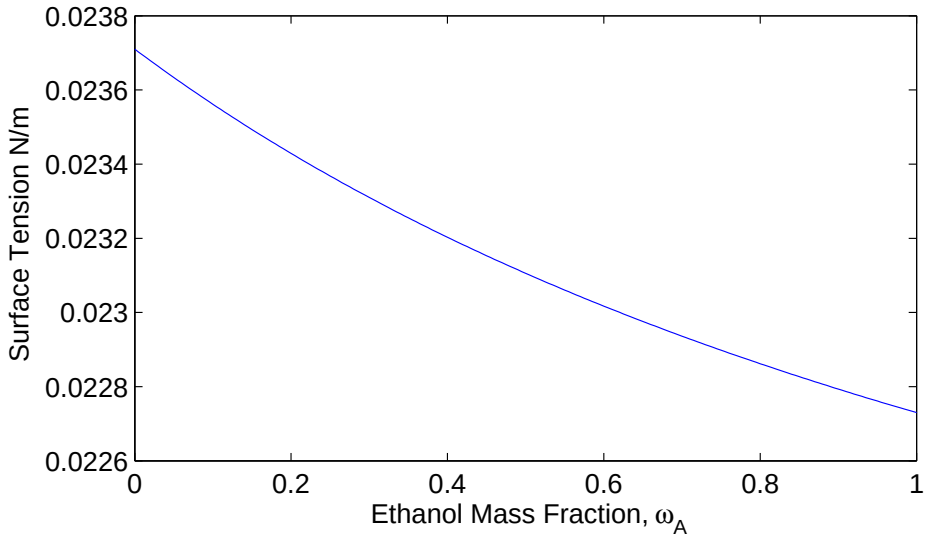

Figure 4-7. Surface tension of the mixture.

evaporation rates of the components where the local temperature gradient is adjusted by the local evaporation and the local condensation. In our system ethanol is the more volatile component with lower surface tension; therefore, with increasing ethanol concentration surface tension decreases shown in Figure 4-7.

The onset of convection depends on several factors such as mass fraction of the mixture, wave number of the disturbance, and phase heights. Due to the selected binary system's thermo-physical properties ethanol and sec-butanol, the system becomes unstable only when it is heated from the vapor side, i.e., negative critical ΔT in the presence of surface tension gradients. This is depicted in Figure 4-8 in a range of mass fractions with wave number as a free parameter for a liquid height of $2\ mm$ and a vapor height of $2\ mm$. Note that the region above each curve is the stable region for that curve because the region represents less negative temperature differences than the critical one. It is clear that for any wave number the middle range of mass fractions is more unstable than the dilute mixtures. In other words, middle range mass fractions require less heating from above compared with the rest of the mass fraction range. This is due to stronger perturbations on the mass fraction in the middle range than the rest.

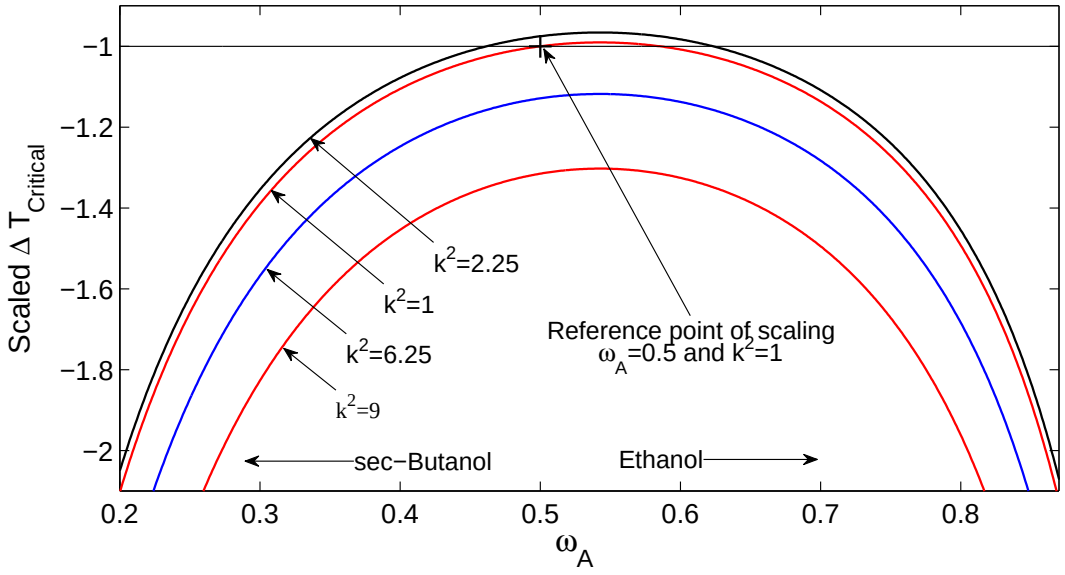

Figure 4-8. Onset of solutal Marangoni driven convection in the presence of phase change. Scaled $\Delta T_{Critical}$ vs. mass fraction, liquid height=2 mm and vapor height=2 mm. $\Delta T_{ref} = -7\,^{\circ}C$.

To support this hypothesis, a numerical experiment is done where the solutal Marangoni number is fixed to that of mass fraction 0.3, Ma_{ω} with $\omega_A = 0.3$, and compared to the results with non-fixed solutal Marangoni results. A Mass fraction of 0.3 is chosen because it is the maximum value of the solutal Marangoni number as shown in Figure 4-9. In Figure 4-10 the numerical experiment is depicted. It is clear that fixing the solutal Marangoni number does not affect the behavior of the onset point; the middle range mass fractions are still more unstable than the dilute region. This means that the change in the solutal Maranoni number with respect to mass fraction is not the reason for this minimum stability region. Therefore, the only mechanism responsible for the minimum stability is the larger perturbations in the mass fraction in the middle region compared with the dilute region.

After identifying why the minimum stability occurs at the middle range mass fraction let us go back to Figure 4-8 again. Although the figure reveals the non-monotonic behavior of the critical point with respect to the wave number, Figure 4-11 is drawn to have a clearer view. This figure can be divided into 3 sections with respect to wave

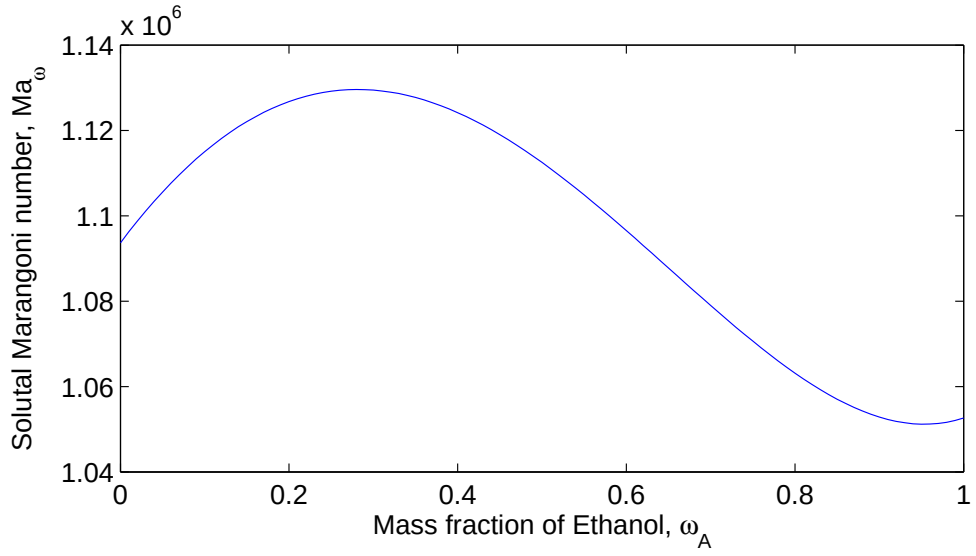

Figure 4-9. Solutal Marangoni number vs mass fraction for liquid height=2 mm.

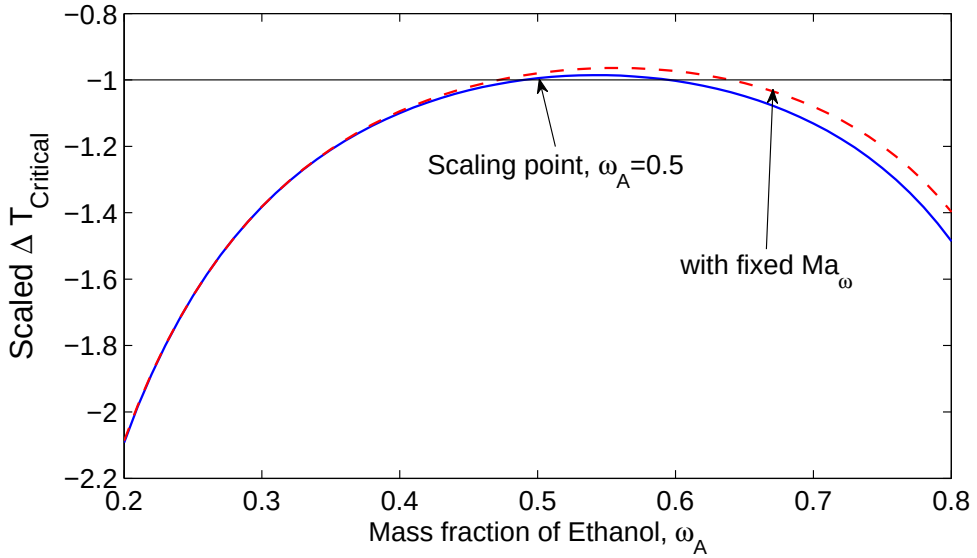

Figure 4-10. Numerical experiment for onset of convection Solutal Marangoni number vs mass fraction for liquid height=2 mm and vapor height=2 mm. $\Delta T_{ref} = -7\ ^{\circ}C$.

number to identify the competition between various effects. In the large wave number region the disturbances become choppier and the system becomes more stable because the transverse diffusion effect increases quadratically with the wave number whereas the system becomes more unstable because transverse variation of the surface

tension is strong. The converse is true at the lower wave numbers. This competition between surface tension gradients and diffusive effects leads to a local maximum in the critical temperature difference as seen in Figure 4-11. At very low wave numbers the critical temperature difference goes to zero (it is not seen in the scale of Figure 4-11). This low wave number tail is a result of the weak interfacial deflection that shows a

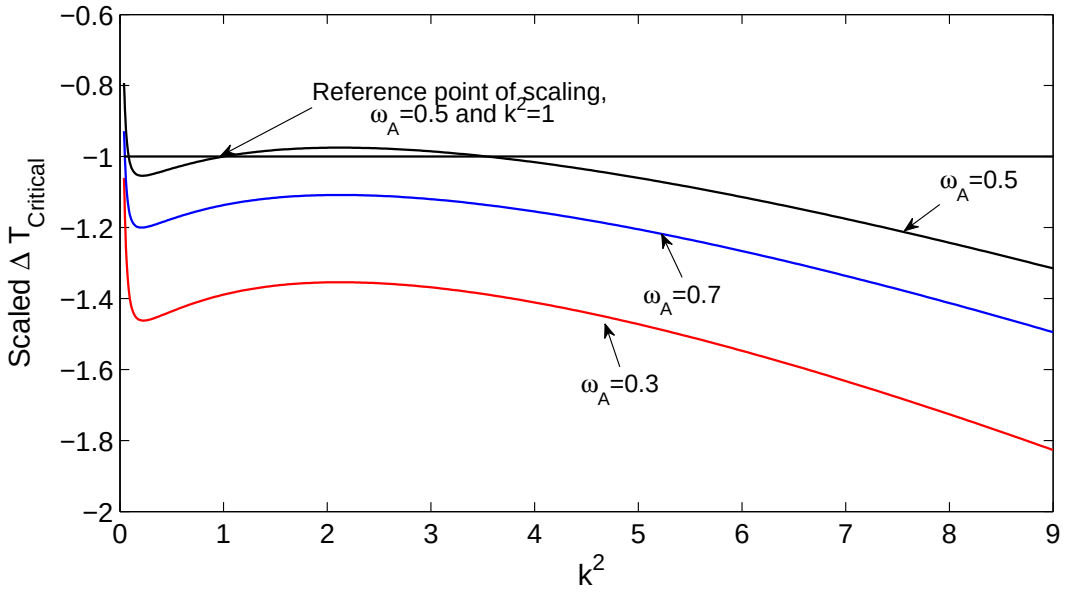

Figure 4-11. Onset of solutal Marangoni driven convection in the presence of phase change. Scaled $\Delta T_{Critical}$ vs. wave number, liquid height=$2\ mm$, and vapor height=$2\ mm$. $\Delta T_{ref} = -7\ ^{\circ}C$.

signature on the instability at the lowest wave numbers and is typical of many interfacial instability problems [36]. The tail is plotted in Figure 4-12 side by side with a result of a model without the surface deflection. This time the figure is plotted $\Delta T_{Critical}$ versus wave number for $_{A} = 0.5$. The model without surface deflection does not exhibit the tail. However, other than the low wave number region the two models give the same results. This means that surface deflection is not the reason for the instability it is just one manifestation and at the onset point its effect is minimal other than the low wave number region.

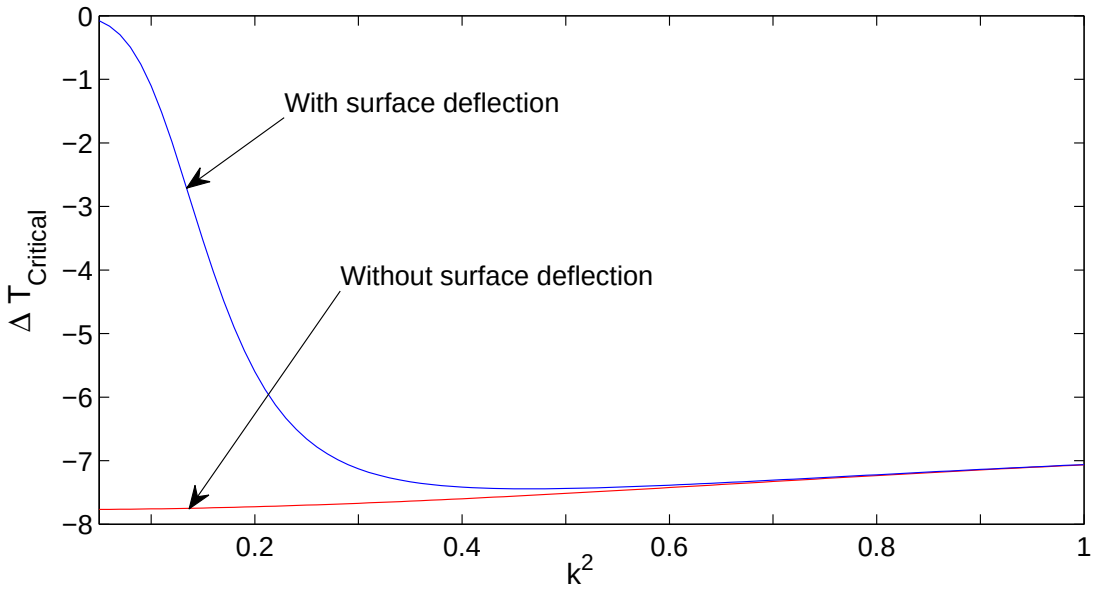

Figure 4-12. Comparison between the model with surface deflection and without for solutal Marangoni driven convection in the presence of phase change. Scaled $\Delta T_{Critical}$ vs. wave number, liquid height=$2\ mm$, and vapor height=$2\ mm$.

Let us go back to Figure 4-11 and observe that the region above the critical curve is in the stable region and the region below is unstable because the physical situation depicts heating from the vapor side, leading to a negative $\Delta T_{Critical}$. The local maximum which depicts the aforementioned competition can be made to disappear by increasing the region of instability. This is done by strengthening the effect of the surface tension gradients and may be achieved by increasing the liquid depth, decreasing the vapor depth or both. Figure 4-13 shows disappearance of the dip by increasing the liquid height from $2\ mm$ to $3\ mm$ by keeping the vapor height constant at $2\ mm$ for mass fraction 0.5. Presence of a local maximum, in Figure 4-13 for a liquid height of $2\ mm$ and a vapor height of $2\ mm$ is also an indication of pattern formation at the onset of instability. In other words, at the onset point there is a wave length that exhibits a maximum growth rate.

In the Figure 4-14 the growth rate is plotted versus the wave number for a mass fraction of 0.5 and applied temperature difference of $-7.3\ ^{\circ}C$ to illustrate the 3 neutral

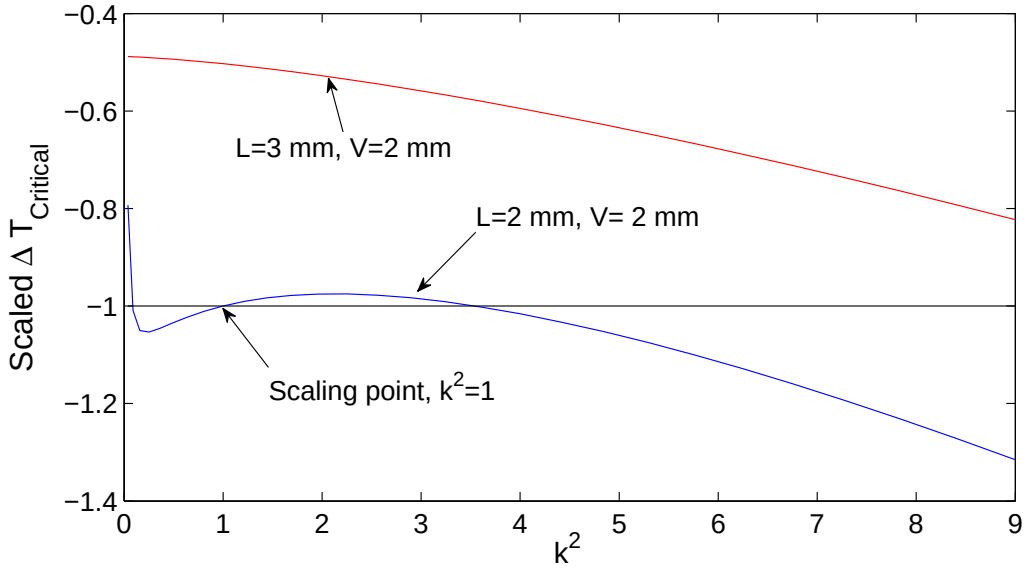

Figure 4-13. Appearance of the local maximum for solutal Marangoni for $\omega_A = 0.5$. $\Delta T_{ref} = -7\ ^\circ C$.

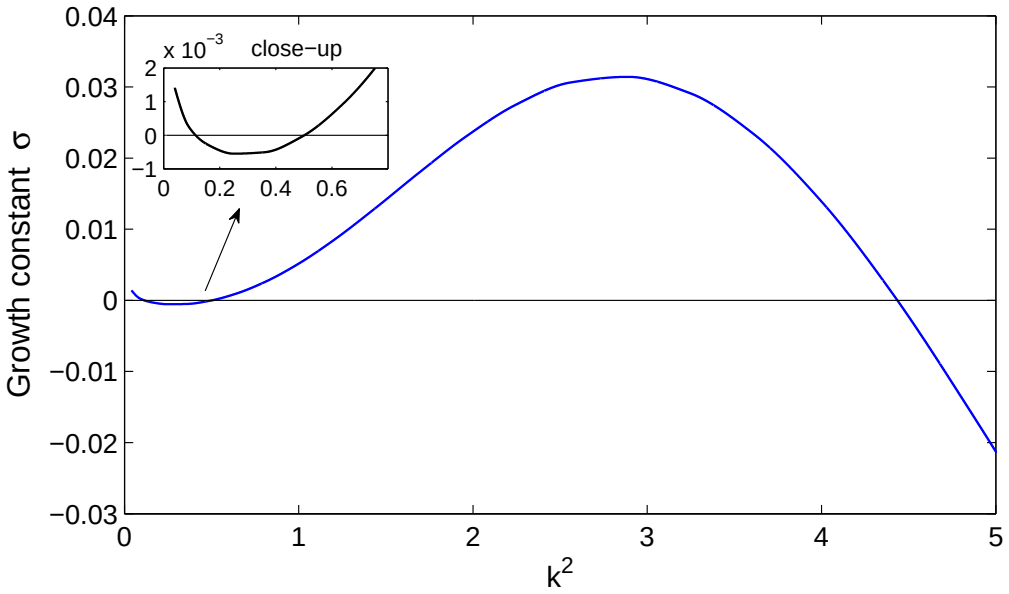

Figure 4-14. Growth constant vs. wave number, liquid height=2 mm, and vapor height=2 mm for $\omega_A = 0.5$. Input $\Delta T = -7.3\ ^\circ C$.

points that appear on account of the local maximum seen in Figure 4-13. The existence of multiple neutral points which confirms the existence of a local maximum assures us of horizontal patterns that may appear at the onset of instability in this problem. If the local maximum in Figure 4-11 were to disappear then only one neutral point would be

obtained in the growth rate curve and the only pattern that would prevail at the onset would be the long wave length flow. Another set of calculations is done to investigate

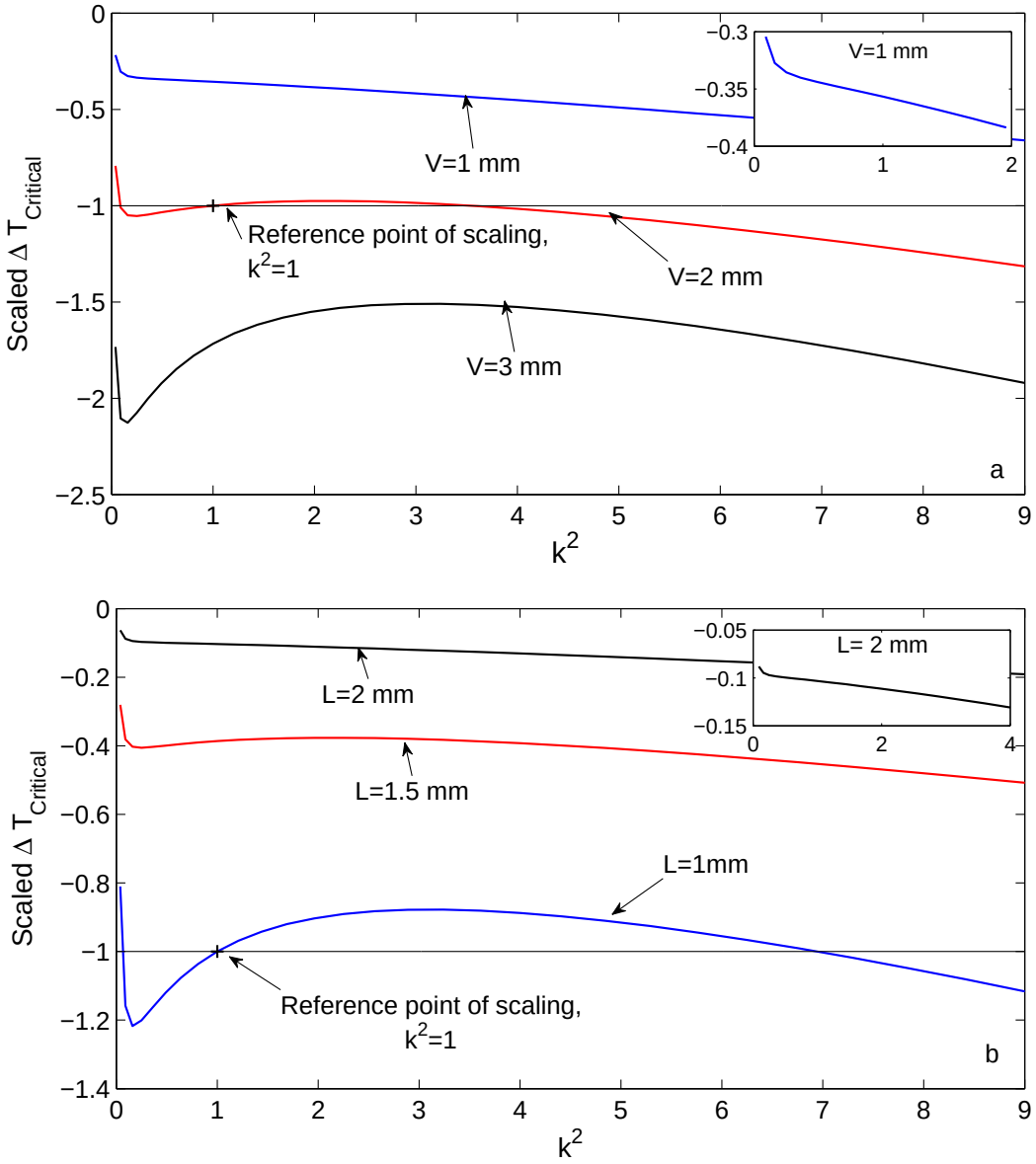

Figure 4-15. Onset of solutal Marangoni driven convection in the presence of phase change for $\omega_A = 0.5$ (a) Effect of the vapor height on the onset, liquid height=$2\ mm$. $\Delta T_{ref} = -7\ ^\circ C$.(b) Effect of the liquid height on the onset, vapor height=$2\ mm$. $\Delta T_{ref} = -14\ ^\circ C$.

the effect of domain heights on the onset point. As indicated in the picture argument given in the introduction section the vapor flow has a stabilizing effect while the liquid flow is destabilizing. That picture argument is supported by the calculations given in

Figure 4-15(a) and 4-15(b); increasing vapor height brings stability shown in part (a) and increasing liquid height makes the system more unstable. This is shown in part (b). Both these figure are also a good representation of how the destabilizing effects can be made strong enough to remove the local maximum similar to Figure 4-10.

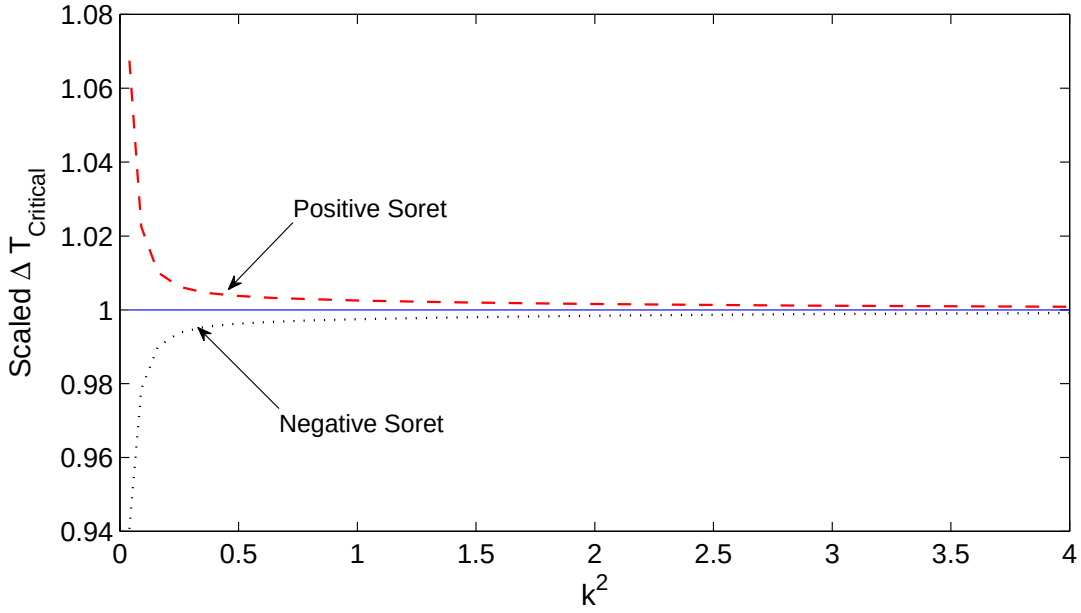

Figure 4-16. Effect of vapor phase Soret diffusion on the onset point. Liquid height=1 mm, vapor height=1 mm for $\omega_A = 0.5$.

In the multi-component systems that are under a temperature gradient there is a second mass diffusion mechanism called the Soret effect. This mechanism is quantified by the Soret coefficient which can be negative or positive depending on the mass fraction and/or the temperature of the mixture. For positive Soret coefficients, the heavy fluid elements move from hot to cold regions and vice versa for negative coefficients. To investigate this effect a new model is developed that includes Soret diffusion in both phases. The modified modeling equations are given in Appendix G. A set of calculations is done to investigate all the possibilities such as negative or positive Soret coefficients, the Soret effect in both phases, or only in one phase. The absolute value of the Soret coefficient is set to be equal to the thermal expansion coefficient. Calculations reveal that the Soret effect in the liquid phase has no effect on the onset point whereas in the

vapor phase it has a minimal effect. To show this minimal effect Figure 4-16 is drawn for $\omega_A = 0.5$, liquid height $1\ mm$, and vapor height $1\ mm$. In the figure both negative and positive Soret coefficient results are scaled using the base model's onset point at corresponding wave number. It is clear that for large wave numbers, due to thermal diffusion dominance, there is almost no difference between the models. The minimal difference manifests itself for small wave numbers where the positive Soret effect introduces a small stability and negative Soret effect introduces a small instability.

4.3.3 Buoyancy Driven Instability with Phase Change

In this section we introduce the additive effect of gravity on the onset point. Gravity has a strong influence on the flow characteristics unless the depths are very shallow or unless the environment is characterized by micro-gravity. In our problem gravity mainly acts on the density gradients. Like surface tension, density is also a function of temperature and concentration. As before the binary mixture consists of ethanol and sec-butanol. In this mixture ethanol is the lighter and more volatile component. In other words, as the ethanol concentration increases the density decreases; likewise as the temperature increases density decreases. The density variation with respect to concentration and temperature is modeled using the Boussinesq approximation and is explained in the Appendix B.

Several calculations are performed to reveal the physics and to do so we see the effect of mass fractions, disturbance wave numbers and domain heights. These calculations not only reveal the physics of the onset of the instability but also reveal the competing effects that come into play when different heating directions are imposed. Again the onset point is represented as scaled $\Delta T_{Critical}$ where the reference scaling point is given in each figure.

The introduction of gravity makes the physics of this problem considerably more involved than the problem that was addressed in the previous parts. We present two situations that are physically realizable. The first is heating from the vapor side, i.e.,

negative critical ΔT and the second is heating from the liquid side, i.e., positive critical ΔT; both situations correspond to neutral conditions. Therefore, upon setting σ equal to zero, we are interested only in the lowest absolute critical ΔT, whether the bilayer is heated from below or from above. In the Figure 4-17 the onset point is drawn versus

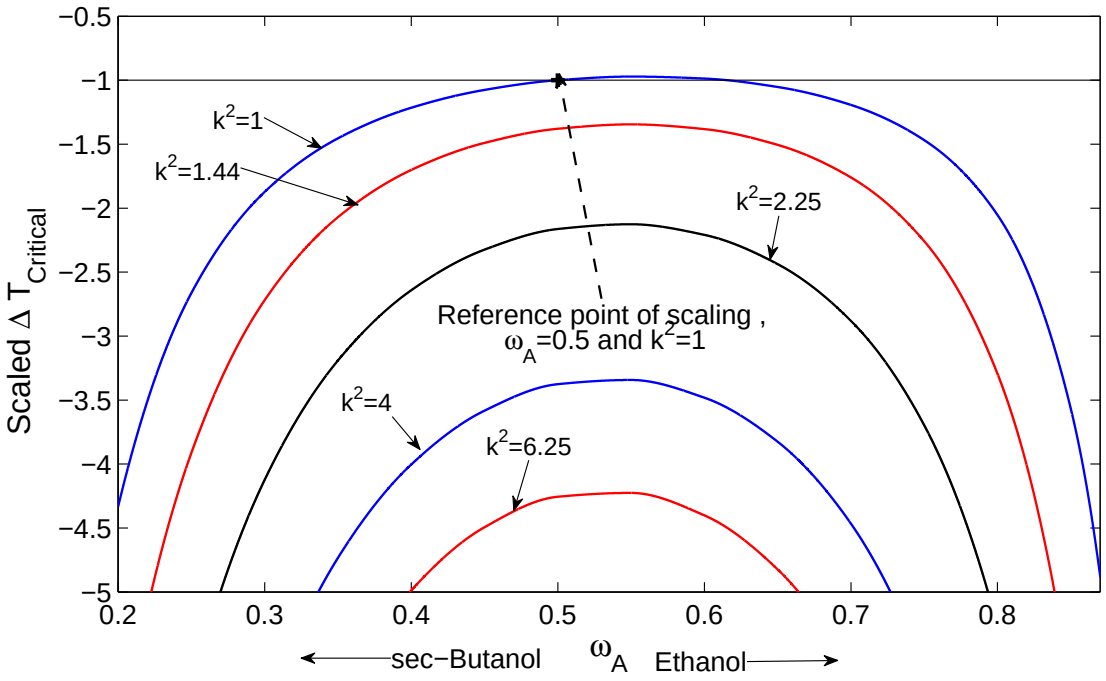

Figure 4-17. Onset of convection for heating from above. Scaled $\Delta T_{Critical}$ vs mass fraction, liquid height=5 mm and vapor height=4 mm. $\Delta T_{ref} = -2.6\,^{\circ}C$.

mass fraction when the heat is supplied from the vapor side, i.e. negative critical ΔT with wave number as the free parameter.

This case is certainly a stable configuration for a single component system and, in fact, we observe that for dilute binary systems this case is also a stable configuration. Figure 4-17, therefore, is drawn within the range of mass fractions that do not include dilute conditions. Now, the negative critical ΔTs are the result of the mass fraction dependence of the surface tension and the density or, in other words, due to solutal Marangoni convection and solutal Rayleigh convection, both in the liquid and in the vapor. Observe that the thermal Rayleigh and the thermal Marangoni effects play

only a stabilizing role, the thermal Marangoni effect being the weak one. Thus, in the presence of gravity a greater negative ΔT is needed to generate the instability than in the absence of gravity. Again observe that the solutal gradients along the interface are caused by the different evaporation rates upon perturbation and the differing surface tensions of the two components. As shown in Figure 4-8 for surface tension gradient driven convection here also the onset point has a strong dependence on the mass fraction. In fact, the critical ΔT increases with the mass fraction, goes through a maximum and then decreases. This maximum occurs in the middle range of mass fractions, principally on account of strong perturbations on the concentration field at the interface in that location. This was an observation made earlier even when gravity was ignored.

To show the stabilization effect of thermal Rayleigh when the heat is supplied from the vapor side Figure 4-18 is drawn for $\Delta T_{Critical}$ versus mass fraction for a liquid height of $3\ mm$ and for a vapor height of $3\ mm$ with a wave number, $k^2 = 1$. In the range of Figure 4-17 the stabilization ratio is around 1.25, i.e., the system in the presence of gravity is 1.25 times more stable than in the absence of gravity. This ratio increases for the dilute case. This ratio may be made smaller by decreasing the liquid height, for example for a liquid height of $2\ mm$ this ratio decreases to 1.05 in the middle range of starting component mass fractions. This supports the fact that for small liquid heights, one can ignore the Rayleigh convection as assumed earlier when Marangoni convection was alone considered.

As can be observed from Figure 4-17 the onset point also depends on the wave number too. This dependence is drawn in Figure 4-19 where the onset point is plotted versus wave number with mass fraction now as the free parameter. As in the previous two sections, i.e. pure evaporative and Marangoni driven convection, appears to be an increase in stability with increasing wave number for any given mass fraction. In the figure this increase is monotonic; however, this is not always the case and we will see,

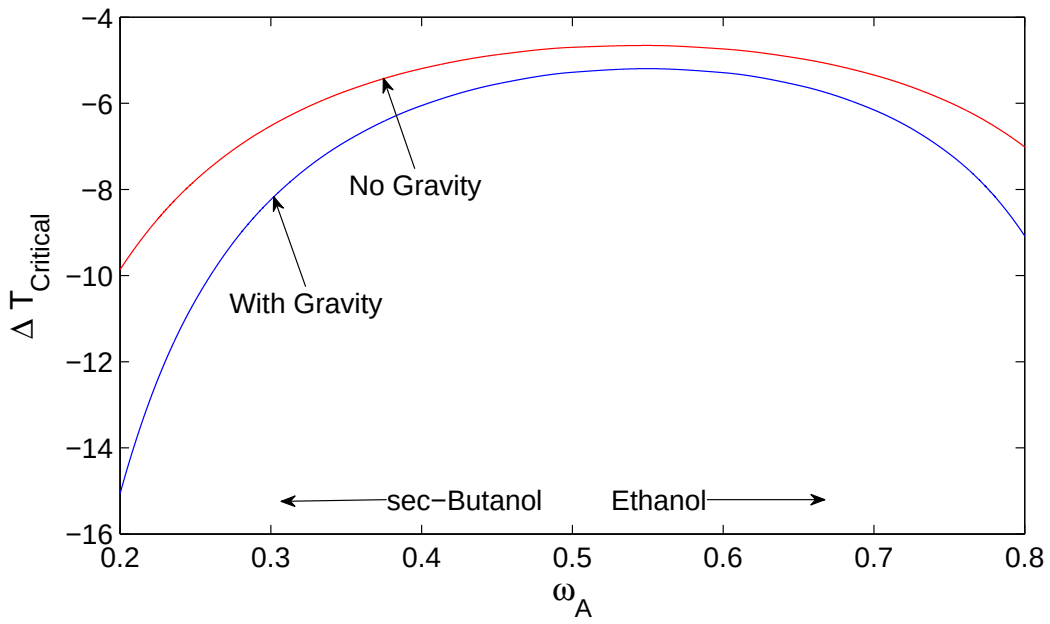

Figure 4-18. Stabilization effect of gravity for liquid height=3 mm and vapor height=3 mm and wave number $k^2 = 1$.

momentarily, why this is so. For small wave numbers, near zero, we always have a tail, i.e., critical ΔT decreases from zero, exhibiting the signature of a deflecting surface or “interfacial mode”.[36] When the liquid heights are large the stabilization offered by the lower horizontal boundary is reduced and inasmuch as the transverse variation of the concentration that is required to precipitate the solutal Marangoni convection is reduced at low wave numbers, even a weak variation is enough to generate some flow. Further increases in the wave number enhance the stability due to diffusion causing the downward trend in the curves of Figure 4-19. To understand why the increase in stability with wave number might not always be monotonic, consider the case of shorter liquid heights and larger vapor heights in which greater convective stabilization obtains. This causes the small wave number regions of the curve to be pulled down and now transverse variation of the concentration enhanced by larger wave numbers can generate the required convective destabilization leading to a local maximum in the curve. This local maximum is a signature of a competition and we see this competition

in our system between the surface tension gradient and the density gradient due to concentration versus the diffusive effects.

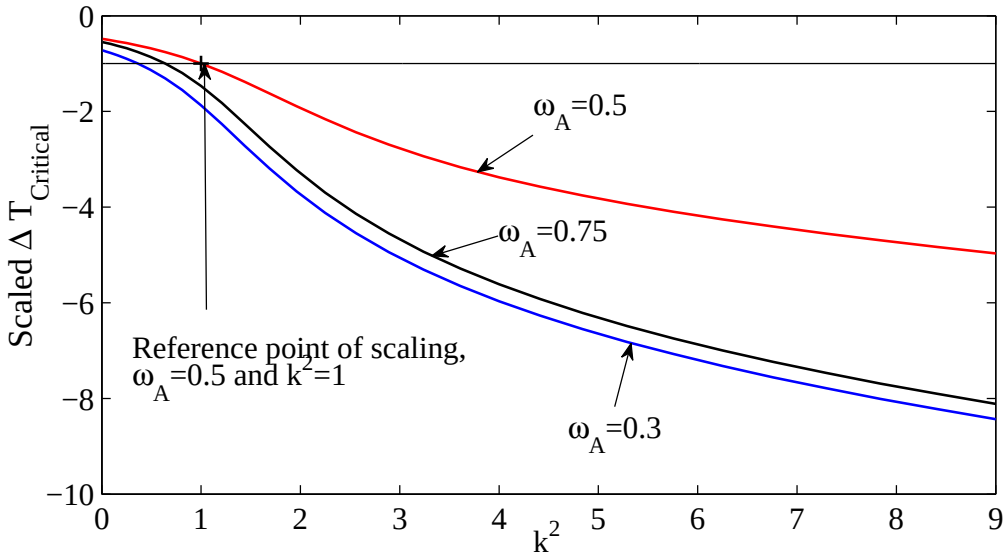

Figure 4-19. Onset of convection for heating from above. Scaled $\Delta T_{Critical}$ vs. wave number, liquid height=5 mm and vapor height=4 mm. $\Delta T_{ref} = -2.6\,^{\circ}C$.

This is made apparent merely by increasing the stability of the system via decreasing the liquid height. Figure 4-20(a) is drawn to show the appearance of a maximum with the decrease of the liquid height, from 5 mm to 2 mm, while Figure 4-20(b) depicts the behavior of the growth constant, σ, for that system for a given applied temperature difference. Both figures are drawn for mass fraction 0.5. In Figure 4-20(b) we see three neutral points where the growth rate is equal to zero. The existence of multiple neutral points also confirms the existence of a local maximum in the critical temperature difference and assures us that horizontal patterns may appear at the onset of instability in this problem.

Unlike the situation where the gravity is absent, the system can also convect when heat is supplied from the liquid side, generating a positive critical ΔT, as depicted in Figure 4-21. In the figure the onset point is plotted versus mass fraction with wave number as a free parameter and for the case of a liquid height of 5 mm and a vapor height of 4 mm. When the heat is supplied from the liquid side the binary mixture

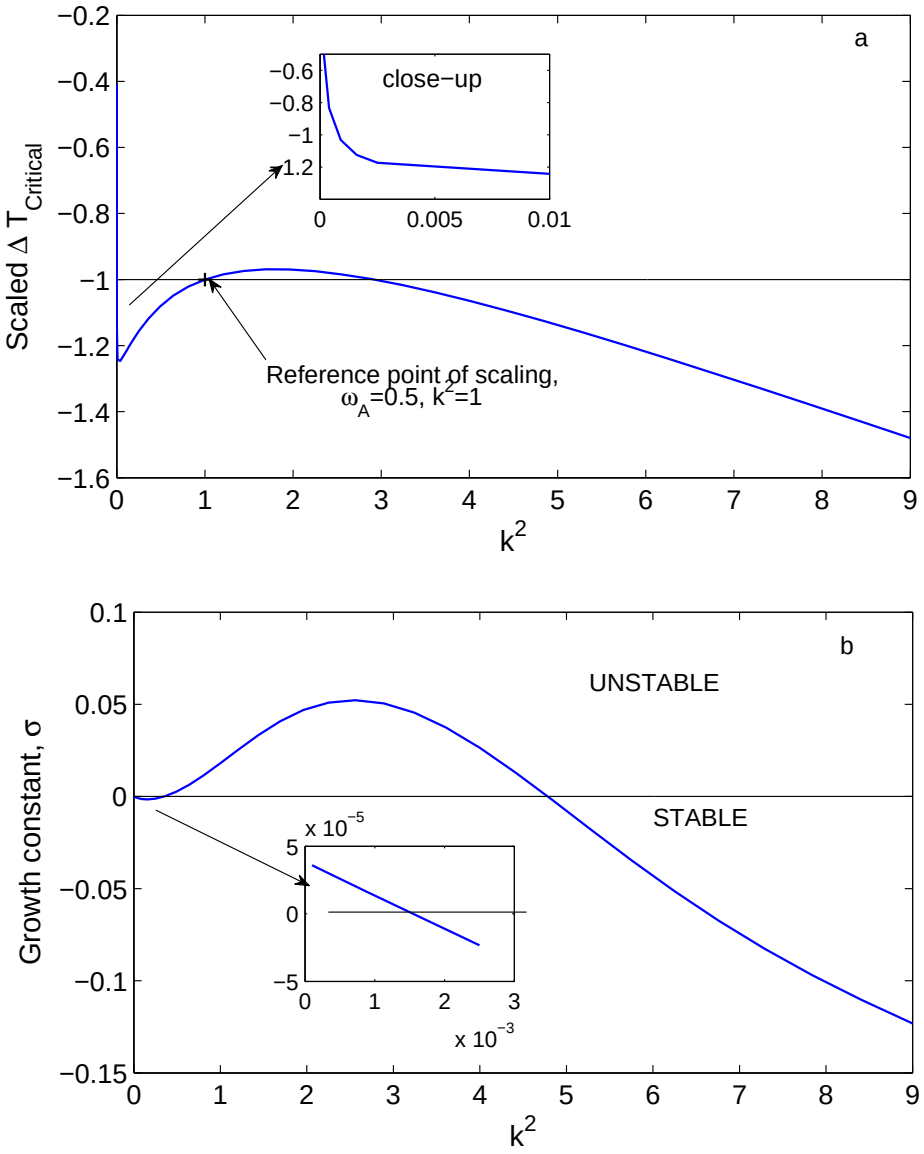

Figure 4-20. Onset of convection for heating from above, liquid height=2 mm and vapor height=4 mm. (a) Scaled $\Delta T_{Critical}$ vs wave number: local maximum. $\Delta T_{ref} = -17.8\ ^{\circ}C$. (b) Growth constant vs wave number: three neutral points. Input $\Delta T_{=} - 20\ ^{\circ}C$.

exhibits a maximum stability in the middle range of mass fraction, analogous to Figure 4-17. This derives principally from the stabilizing effect of solutal convection when the system is heated from the liquid side. The maximum appears near the middle much as in the heating from the above case. The appearance of this maximum near the mid-range mass fractions are due to the concentration perturbations which are the

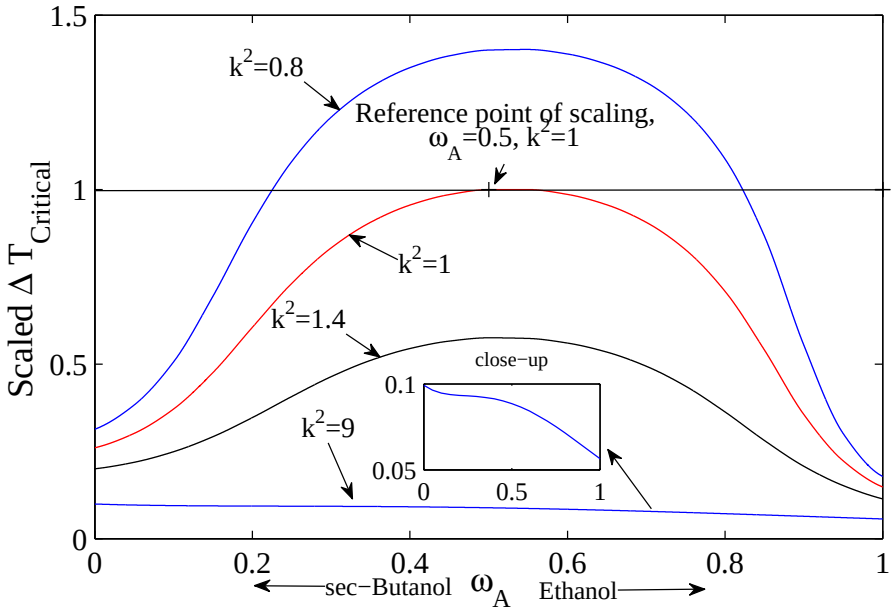

Figure 4-21. Onset of convection for heating from below. Scaled $\Delta T_{Critical}$ vs. mass fraction, liquid height=5 mm and vapor height=4 mm. $\Delta T_{ref} = 13.7\,^{\circ}C$.

strongest there and which only serve to stabilize the system because of the heating arrangement. An additional observation that one can make from the figure is that the maximum of the curves get progressively weaker with the increasing wave number ultimately leading to the monotonic decay with the mass fraction. This requires an explanation. To see why the maximum gets weaker and then disappears consider Figures 4-22(a) to (f) where two curves are depicted in each sub-figure. The upper curve is the usual one drawn in the manner of Figure 4-21; the lower curve on the other hand refers to an artificial case, one where the solutal expansion coefficients in both phases as well as the solutal surface tension gradient are set to zero. This case which is called the pure thermal problem may also be viewed as a single component system that has the thermo-physical properties of a binary mixture for each corresponding mass fraction. A comparison between the two models, as the wave number increases, is made progressively from Figure 4-22(a) to (f). And progressively, we see the increasing effect of the thermal diffusion i.e., the increasing effect of the thermal dominance. What

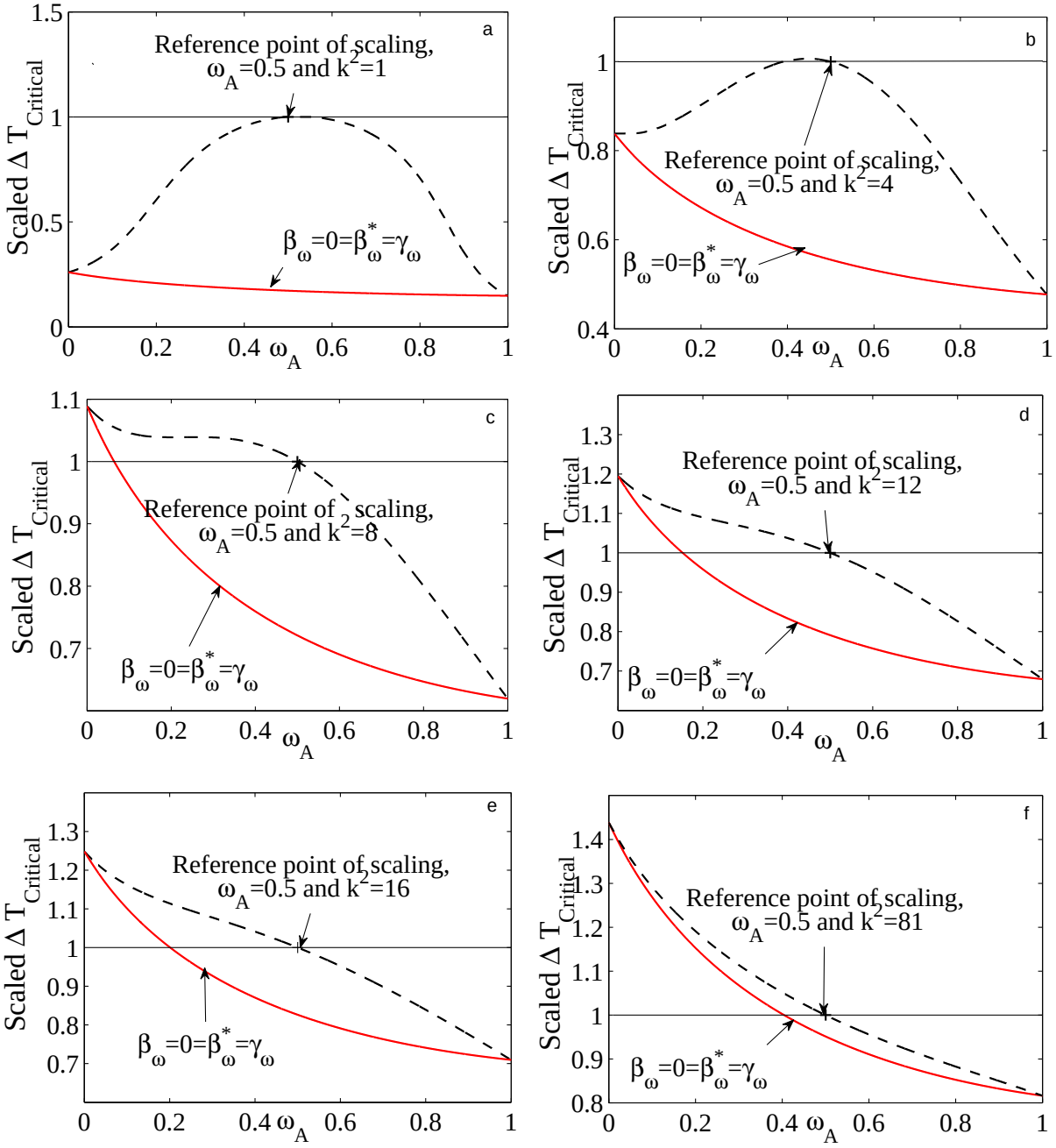

Figure 4-22. Onset of convection for heating from below, the effect of solutal convection (Ra_ω, Ma_ω) with increasing wave number. Scaled $\Delta T_{Critical}$ vs. mass fraction, liquid height=5 mm and vapor height=4 mm. (a) $k^2 = 1$ $\Delta T_{ref} = 13.7\ ^\circ C$ (b)$k^2 = 4$ $\Delta T_{ref} = 1.8\ ^\circ C$ (c)$k^2 = 8$ $\Delta T_{ref} = 1.2\ ^\circ C$ (d)$k^2 = 12$ $\Delta T_{ref} = 1.2\ ^\circ C$ (e)$k^2 = 16$ $\Delta T_{ref} = 1.4\ ^\circ C$ (f)$k^2 = 81$ $\Delta T_{ref} = 8.1\ ^\circ C$.

stands out is that the binary problem, given by the upper curve, approaches the thermal problem, losing its maximum and ultimately merging with it for very large k^2.

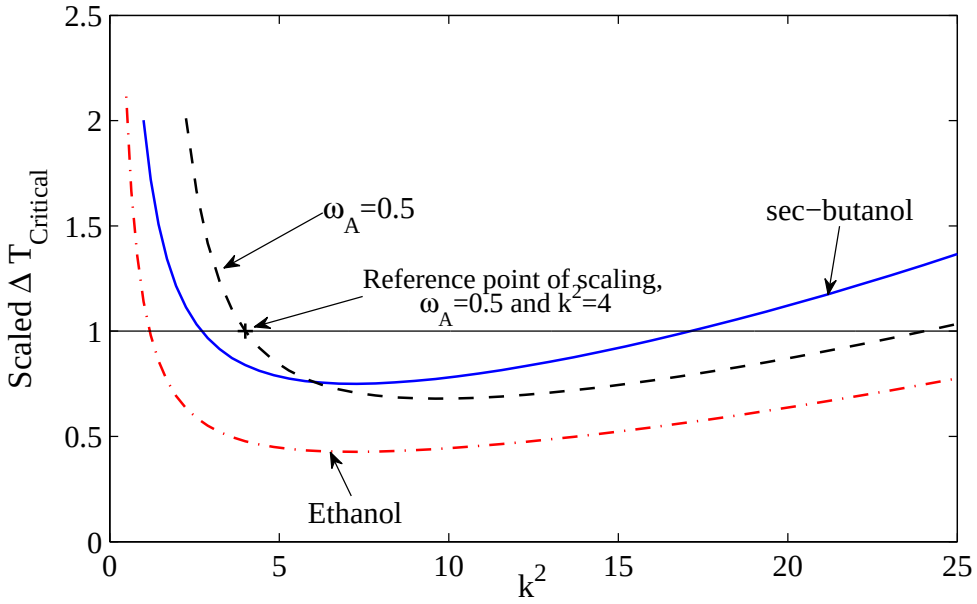

Figure 4-23. Onset of convection for heating from below. Scaled $\Delta T_{Critical}$ vs. wave number, liquid height=5 mm and vapor height=4 mm. $\Delta T_{ref} = 1.8\ ^{\circ}C$.

The behavior of this maximum getting weaker with increasing wave number can also be seen in Figure 4-23 from a different point of view while simultaneously showing the effect of wave number for heating from the liquid side for a fixed mass fraction. As seen in the figure, a 50/50 weight percent mixture is more stable than either pure ethanol or pure sec-butanol in the small wave number region. And since the maximum disappears in the large wave number region, the critical ΔT for the mixture lies between the two pure components. Now, no matter what the concentration of the mixture is, a minimum or a dip is present in Figure 4-23. This dip is a result of a competition between the destabilizing horizontal density gradients caused by the thermal expansion which gets stronger for small wave lengths and the stabilizing thermal diffusion which also gets stronger for small wave lengths. The solutal gradients play only a stabilizing role and their effect is not a cause for the dip. Once again the presence of a dip is indicative of

cellular patterns that can obtain in this problem. And once again one must expect the curves to exhibit a tail descending toward the origin even though it is not depicted within the scale of Figure 4-23.

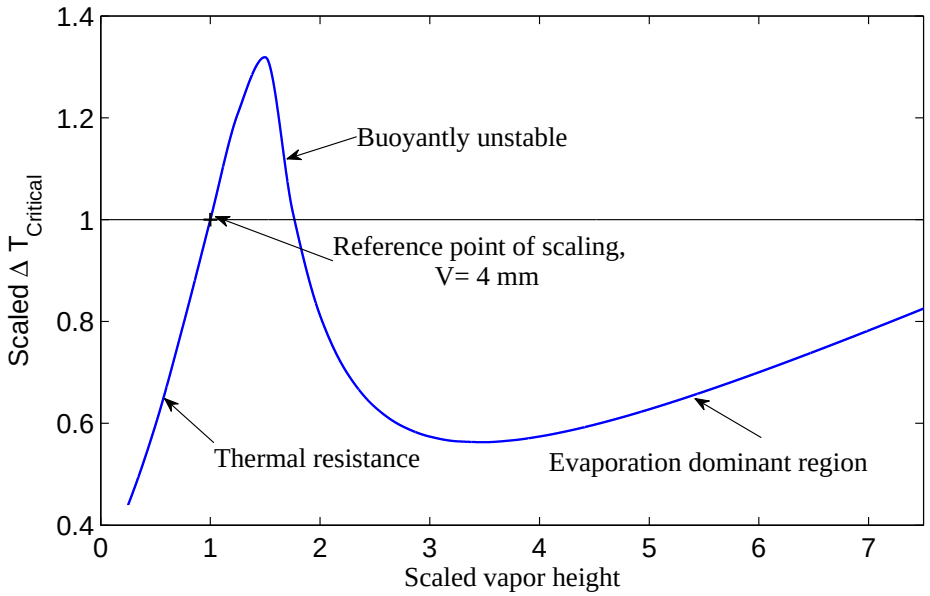

Figure 4-24. Onset of convection for heating from below, the effect of the vapor height. Scaled $\Delta T_{Critical}$ vs. scaled vapor height, liquid height=$4\ mm$, $\omega_A = 0.5$ and $k^2 = 6.25$. $\Delta T_{ref} = 3.7\ ^\circ C$.

Finally, we consider the result of one more calculation that reveals the physics of the problem. This has got to do with the effect of the vapor height and to be concrete we restrict ourselves to heating from the liquid side. Figure 4-24 shows three different physical situations that obtain upon increasing the vapor height for a fixed liquid height. The initial increased instability depicted by an increase in the critical ΔT arises on account of stabilization offered by the increased thermal resistance. The subsequent decrease in the critical ΔT is a result of increasing thermally buoyant flow in the vapor and the final increase in the stability is a result of vapor flow in the evaporation dominant regime. This competition between thermal resistance and thermal buoyancy has been observed both experimentally and theoretically in non-evaporation systems by Ozen et al. [9]

4.3.4 1-D Model to 3-D Model

As described in the first part of this section thanks to stress free condition on a 3-D model we can directly compare a 1-D model to the 3-D model that uses azimuthal expansion modes. The details of this comparison are given in the Appendix J. Using a 1-D model is much simpler than using a 3-D model in many ways such as computation time and the computation power needed. However in an experiment, because of the finite dimensions the system does not have access to all wave numbers. The allowed wave numbers are the origin of the patterns that would be observed in an experiment at the onset point. The azimuthal mode arises from the θ-direction expansion given by,

$$U_1 = \widehat{U}_1(z)e^{\sigma t}e^{im\theta}$$

in the 3-D model. In the following figure some possible patterns are depicted for various azimuthal modes.

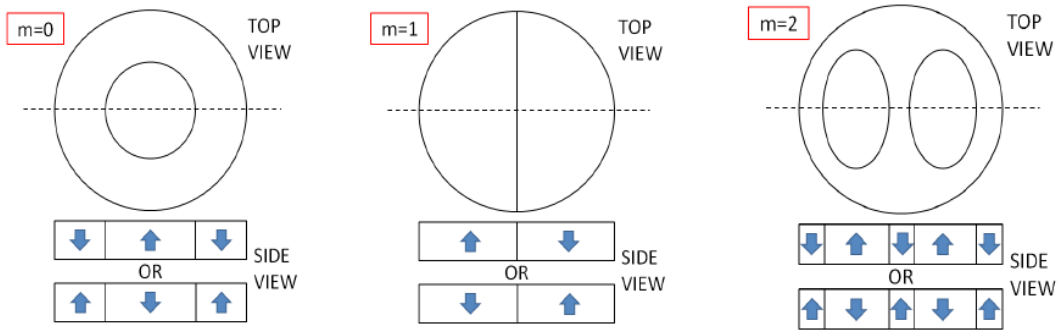

Figure 4-25. Different azimuthal modes.

The Figure 4-27 is drawn to depict the onset point, as in $\Delta T_{Critical}$, versus wave number for liquid height $2\ mm$ and for vapor height $3\ mm$ and mass fraction 0.5. There is a clear dip at $\Delta T_{Critical} = 12.8$ for wave number 1.44. All convective mechanisms are assumed.

The onset curve is a continuous curve; however, a finite system, i.e. a system with sidewalls, does not have access to all those wave numbers. To find out the accessible ones we need to use the wave number to azimuthal conversion formula which is given

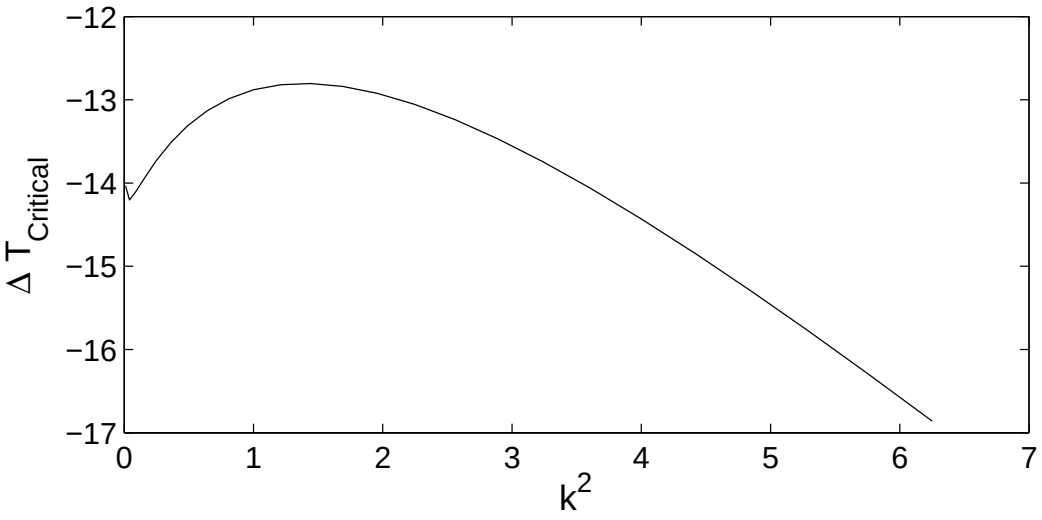

Figure 4-26. Onset of convection versus wave number for liquid height=2 mm and vapor height=3 mm and $\omega_A = 0.5$.

below. For the 1-D model, the inputs to a calculation are the domain heights, wave number of the disturbance, and the initial mass fraction. On the other hand, in the 3-D model, instead of wave number of the disturbance, the radius and the azimuthal mode are the other inputs into a calculation. By inputting the radius the aspect ratio is set, which is radius over the liquid height, and by inputting the azimuthal mode the output planform function is set (this is theoretically given by a Bessels function). Again for details see the Appendix J. With this information the dimensionless wave number is given in terms of the aspect ratio and the root of the derivative of the Bessel function i.e.,

$$k_{\mathrm{m,j}} = \frac{Jr_{m,j}}{\chi} \tag{4–1}$$

Where, χ is the aspect ratio and $Jr_{m,j}$ is the root of the derivative of the Bessel function kind m.

To make the comparison, let us set the radius to $6\ mm$. This sets the aspect ratio to $\chi = 3$. With Bessel's function, $Jr_{m,j}$, we get the corresponding wave numbers for each of the azimuthal modes. These points are given in the Figure 4-28.

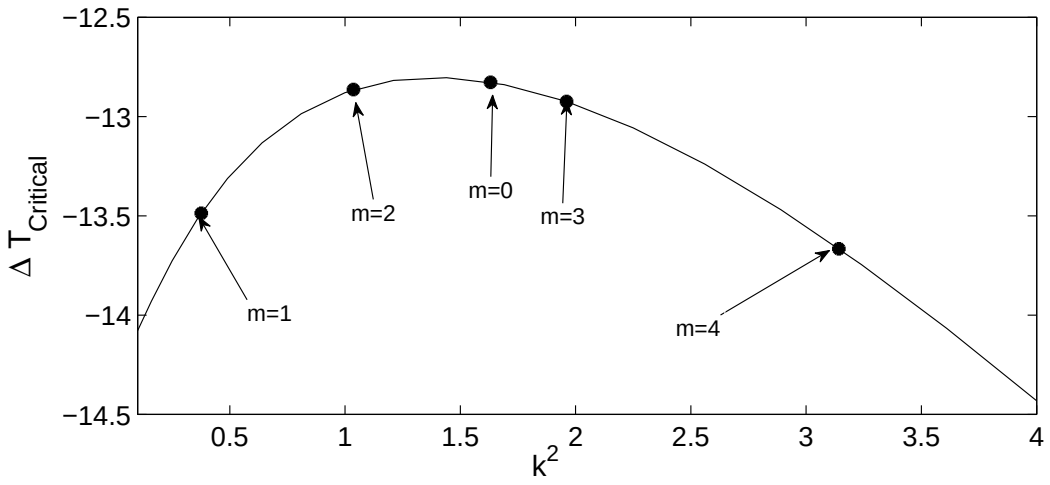

Figure 4-27. Onset of convection versus wave number for liquid height=$2\ mm$ and vapor height=$3\ mm$ and $\omega_A = 0.5$. Available wave numbers with respect to azimuthal modes.

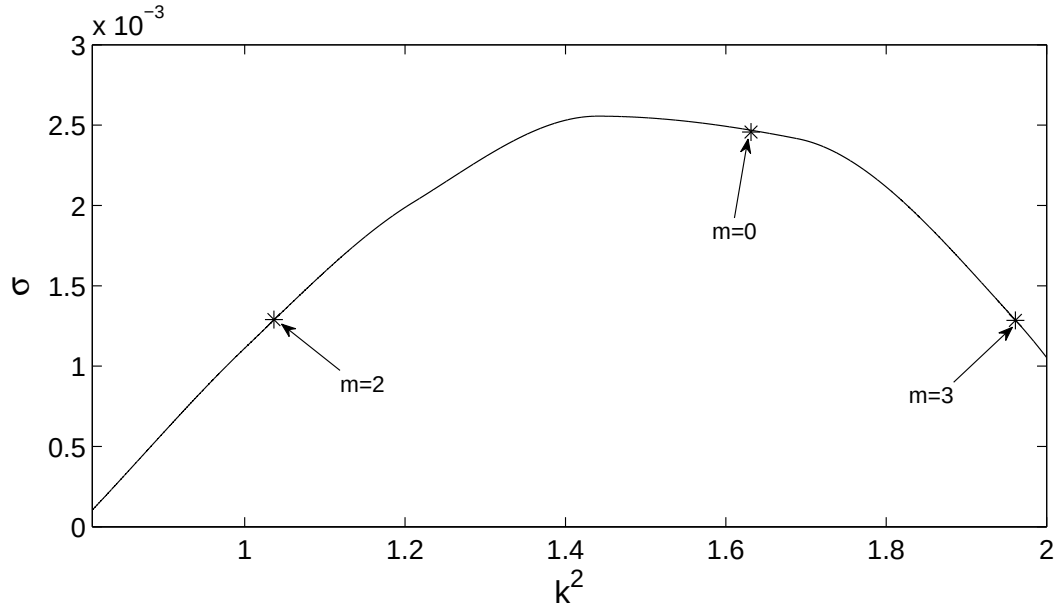

Figure 4-28. Growth rate versus wave number.

In the figure the $m = 0$ mode has the lowest temperature difference meaning that on the onset point the observed pattern would be a donut shape $m = 0$. This is also supported by the growth rate calculation that is given in the Figure 4-28 where the growth rate of the system is calculated using a given ΔT of 12.9 degrees.

One major result that stands out as a consequence of our study is this: Given a thin fluid mixture, we can determine, without any calculation, whether the heating should be from the vapor side or the liquid side in order to avoid an instability. If the fluid mixture is thick in dimension such that gravity plays a role then calculations will determine the direction of heating and the amount of heating to avoid the instability.

CHAPTER 5
EXPERIMENTAL SETUP AND RESULTS

An experimental set-up was built to verify many of the qualitative predictions. For example in pure components the heating from above arrangement is a stable configuration, while for binary systems instability can be triggered when heated from the vapor side. The picture of the experimental setup is given in Figure 5-1 where the whole setup was placed inside a transparent box. The setup consisted of an IR camera or a CCD camera (not shown in the picture) and temperature control systems both for the box and the liquid side of the test section. A schematic of the setup is given in Figure 5-2.

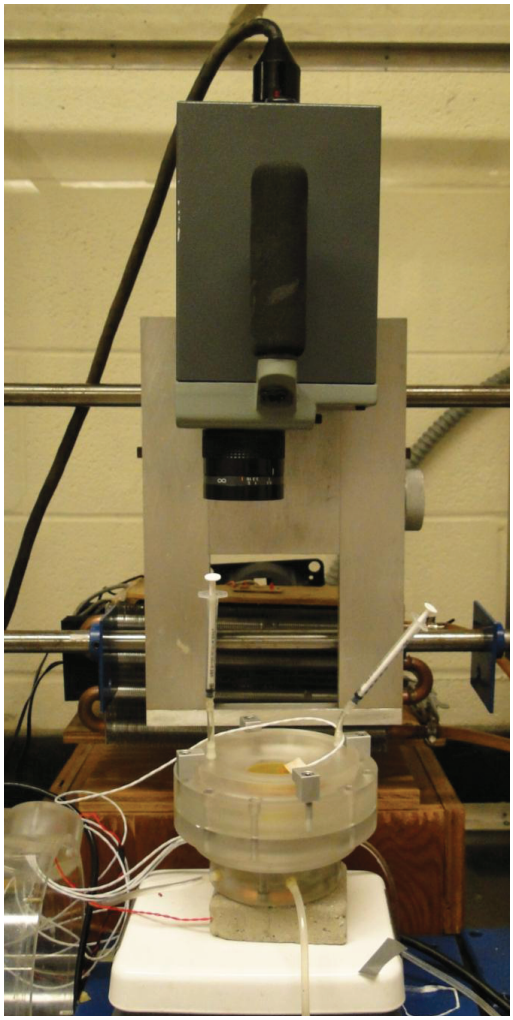

Figure 5-1. Experimental setup.

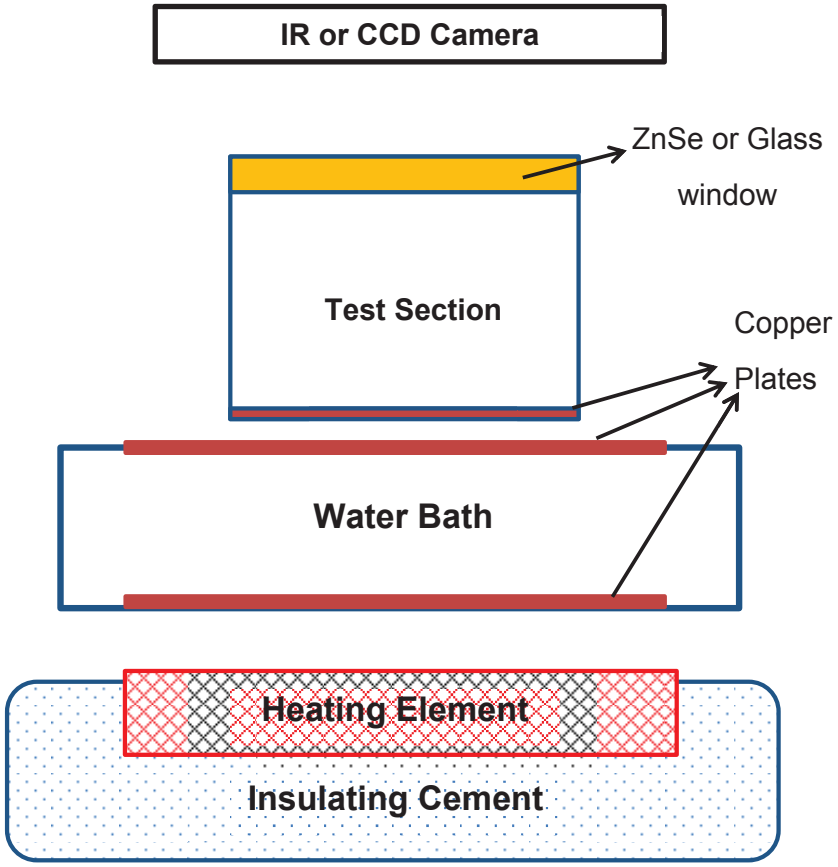

Figure 5-2. Schematic of the experimental setup.

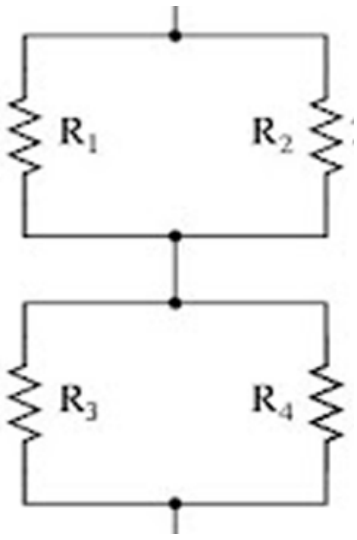

Figure 5-3. Schematic of the RTD connection.

As described previously the only control parameter is the vertical temperature gradient and in an experiment. This gradient is applied to the test section between the zinc selenide window (or glass window) and the copper plate of the test section. As shown in Figure 5-2, the liquid side temperature control system consisted of several sub-parts. The first part was the heating element, which was placed inside insulating cement. This heating element was placed over a magnetic stirrer. On top of the heating element there was a water bath with a magnetic stir bar to ensure the uniform temperature profile in it. The top and the bottom of the water bath were capped with copper plates. To increase the efficiency of the temperature control inside the water bath, cold water was fed into and out of the bath using a mini-pump. To measure the temperature, four resistance temperature detectors (RTDs) from OMEGA® were placed under the upper copper plate. RTDs were used because of their high actuary and their stability, i.e. RTDs do not require frequent calibration. To get an accurate reading from four RTDs require two sets of RTDs connect in parallel and these parallel connected sets combined in series (see Eqn 5–1), this is shown in Figure 5-3. The temperature of the liquid side copper plate temperature and the zinc selenide window were controlled by PI (OMEGA®) controllers. These temperature controllers require an initial calibration in order to find the ideal proportional and integral control parameters for the system. Calibration was done using the automatic calibration sequence option in the controller and further fine tuning was done by the user. Copper plate temperature was controlled only by controlling the heating element not the cold water inlet. This inlet could be controlled by the user depending on the set point of the temperature. The overall control was better than $-/+ 0.1\ ^{\circ}C$.

$$R_1 = R_2 = R_3 = R_4 = R$$
$$R_{Total} = \frac{1}{\left(\frac{1}{R_1} + \frac{1}{R_2}\right)} + \frac{1}{\left(\frac{1}{R_3} + \frac{1}{R_4}\right)} = R \tag{5–1}$$

The test section was placed over the water bath. It was consists of lucite-air-tight containers. The accuracy of each piece was machined within $0.1\ mm$. This section housed the liquid and vapor mixture. The inside of the test section was made accessible from the outside using inlet and outlet holes, piping, and valves.

Two different test sections were used during the experiments. The first test section was made up of two pieces: liquid insert and vapor insert. Air-tightness of this test section was ensured by using O-rings and screws. The liquid side's bottom boundary was a copper plate placed over the water bath. The vapor insert was screwed over the liquid insert between those two O-rings, which were placed to ensure the air-tightness. The top boundary of the vapor insert was the zinc selenide window that is situated inside a lucite holder. The holder was clamped to the vapor insert. Here, also, O-rings were employed. The second insert was a one-piece insert designed to be see-through to obtain a side view of the convective flow. It had a copper plate at bottom boundary and a glass window at the top boundary.

For both inserts zinc selenide (glass windows) were used to apply the upper temperature set point to the test section. The temperature was measured using an RTD that was placed over the windows. The set point was the temperature inside the box that housed the whole set-up. A heater, fan, and car radiator were used to control this temperature. Here also the PI controller only controlled the heating element with an overall control which was better than $-/+\ 0.1\ ^{\circ}C$.

An Inframetrics, model 760, infrared camera was used to visualize the flow patterns when the zinc selenide window was used. This particular model of infrared camera is capable of measuring in the 3 to $5\ \mu m$ range or the 8 to $12\ \mu m$ range; however, only the 8 to $12\ \mu m$ range was used due to the temperature range of the experiments, i.e. 20 to $40\ ^{\circ}C$, and also in that range the zinc selenide window is 60% transparent to infrared radiation. The infrared camera was placed directly above the test section and measured the infrared radiation being emitted by the liquid. An effective emissivity

could be calibrated and programmed into the infrared camera to find the temperature of the interface. The IR camera was never used to measure the temperature, rather it was used to detect the variation in interfacial temperature from which the flow structure could be deduced. Additionally, an anti-reflective infrared polymer was coated on the zinc selenide window by II-VI Inc. This coating was useful to decrease the false images generated by reflected, ambient infrared radiation.

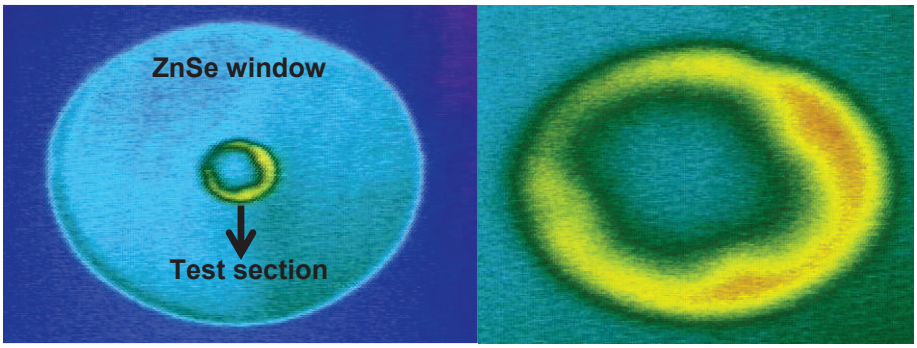

Figure 5-4. Thin film condensation on the ZnSe window. Heating from below for $\Delta T = 1.2\,^{\circ}C$.

For the glass window setup, Kalliroscope tracer or aluminum flakes and CCD camera couple were used to visualize the flow. Both the CCD and IR camera were directly connected to a computer where a time lapse video was captured.

In a separate air-tight-metal container alcohol vapors were produced to flush the air inside the test section. This metal container had one outlet and one inlet hole that were controlled by valves. To produce the alcohol vapor, liquids were fed into the container and placed over a heater. First, both valves were kept open to allow air to escape. After closing the valves, but keeping the heater on, the vapor was sucked by syringes. However, the vapor equal to 4 times of the metal container volume was not used to flush the air inside the test section to ensure very low air concentration. Further vapor that was produced fed into the test section using the inlet holes and valve system. Again to ensure a very low concentration of air the test section was flushed by alcohol vapor (either pure or mixture) at least 20 times of its volume.

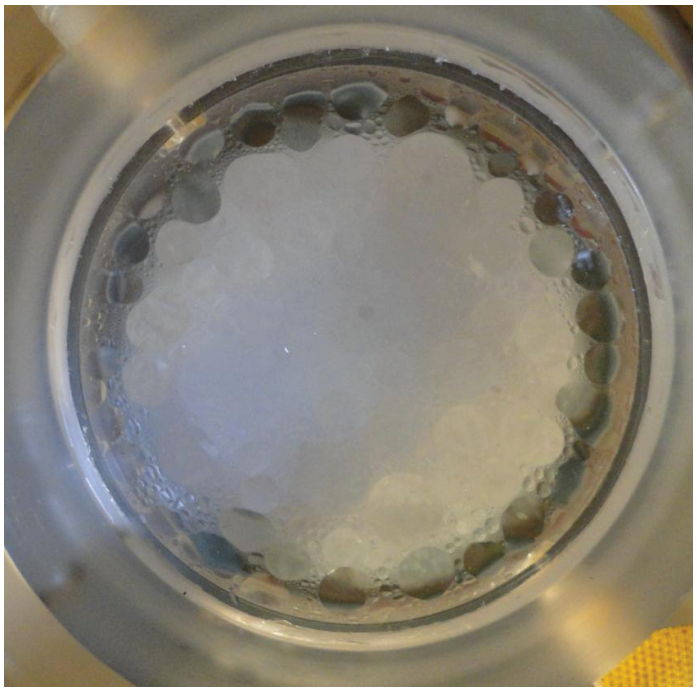

Figure 5-5. Condensation on the glass window. Heating from below for a binary mixture of 50/50. Input $\Delta T = 5$. Liquid height=$10\ mm$, vapor height=$15\ mm$, and diameter=$38.1\ mm$.

Sigma-Aldrich ethanol $99.5 + \%$ purity and Sigma-Aldrich sec-butanol $99 + \%$ purity were used during the experiments. There are several reasons using ethanol and sec-butanol for the experiments. These can be listed as;

- They are both safe to use in a laboratory environment.
- Thermo-physical properties for both vapor and liquid phases are well documented from a single source.
- Both liquids are compatible with the rest of the experimental setup in experimental conditions.
- They are low-weight alcohols and similar in structure which allows to assume ideal mixing.

In the heating from below experiments due to ZnSe or glass window being colder than the interface, a condensation occurred on the windows even for the temperature differences less than a degree. This condensation blocks the IR radiation going through the ZnSe window; therefore, no signal was received from the interface. This is shown

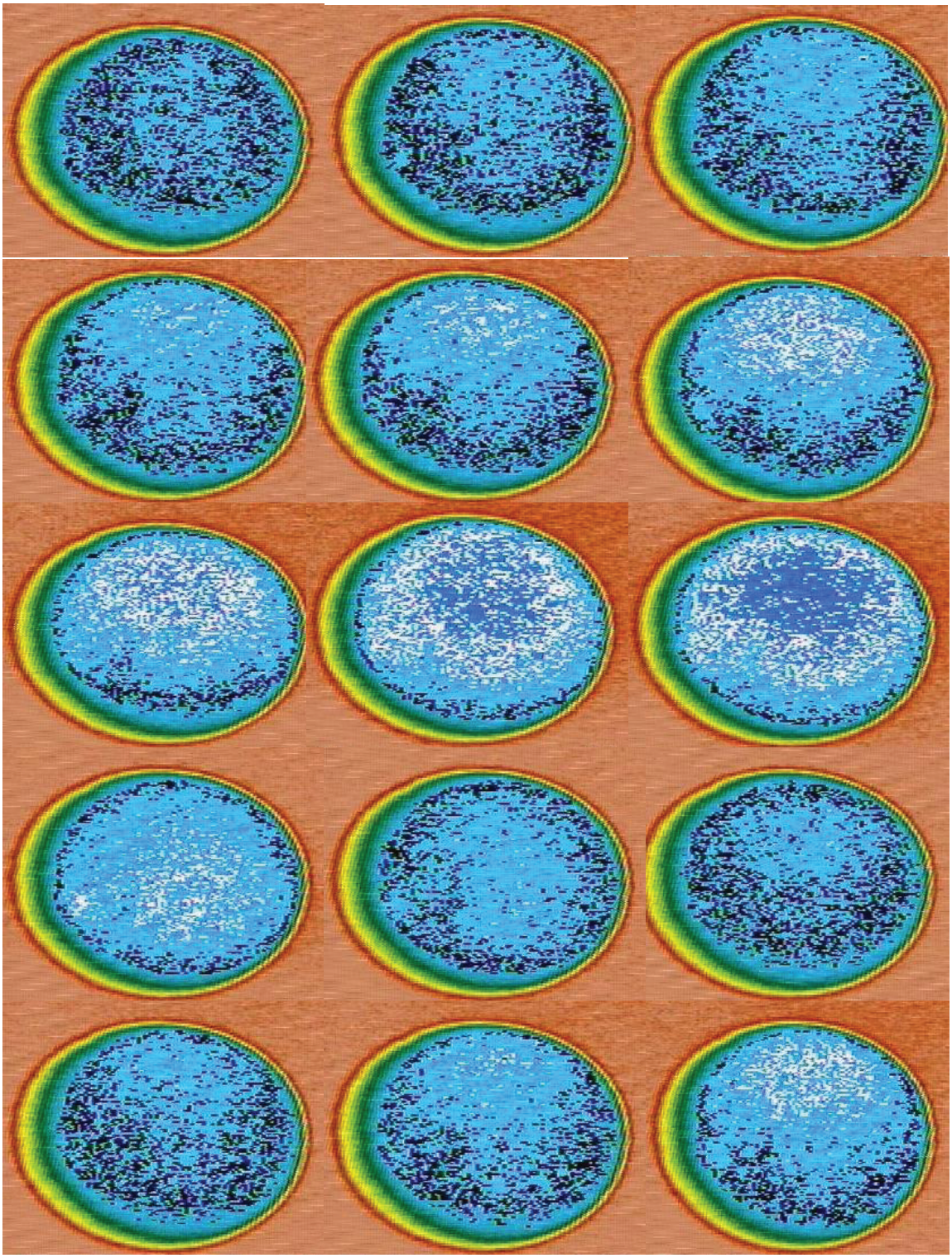

Figure 5-6. Heating from above convective flow for $\Delta T = -7.5$. Long wave length instability for 50/50 binary mixture.Liquid height=$6\ mm$, vapor height=$14\ mm$, and diameter=$18\ mm$.

in Figure 5-4 for ethanol. In the left picture the big circle is the ZnSe window, which has a uniform temperature profile. The test section is the little inner circle; it is made clearer in the right picture. Condensation was unavoidable when the heat was supplied from the liquid side with this set-up. A possible reason why sub-cooling of vapor phase was not possible could be the presence of dust particles in the vapor phase or on the viewing window which serves as nucleation center for condensation. Working in a clean room environment and a pre-treatment of ZnSe or glass window might help to avoid the condensation problem. Although condensation is an unwanted phenomena for this work, for a larger temperature difference the condensation on the window also manifested an instability which might be worth researching about. This is given in Figure 5-5.

Although condensation on the top plate was not part of our model to observe the phenomena, several side views of the convective flow were obtained using Kalliroscope particles; However, these particles did not create enough contrast to have clear, still images. Additionally, aluminum flakes were used for flow visualization with both ethanol and sec-butanol; thus, these particles settled down really fast and had a tendency to collide together. This is a problem of low viscosities of the alcohols which is not easy to avoid. One possible solution is to increase the viscosity of the mixture by adding small amount of silicone oil. However, adding a non-volatile third component will not only modify the viscosity but also modify the physics of the liquid phase behavior.

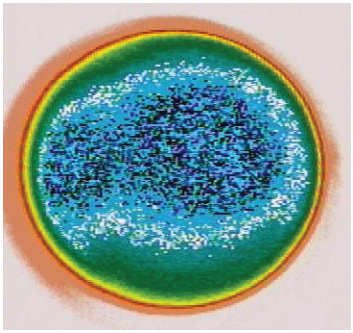

Figure 5-7. Heating from above convective flow for $\Delta T = -15$ for $50/50$ binary mixture. Liquid height=$12\ mm$, vapor height=$13\ mm$, and diameter=$38.1\ mm$.

In the heating from above experiments due to constant evaporation and condensation the temperature at the interface fluctuates; therefore, it was not possible to observe a clear no-flow state. The convective flow that is shown in Figures 5-6 and 5-7 for a binary mixture were principally done to verify the phenomena. In the Figure 5-6 a long-wavelength instability is observed. The liquid coming from the bottom of the domain rises from the upper part of the insert that goes along the interface and falls down from the domain part of the insert. In Figure 5-7 the azimuthal mode 2 is shown. As is expected in a similar experiment for a single component system, no pattern formation was observed.

Meanwhile, to overcome the thermal reading problems for both heating from above and below, the ZnSe window was replaced by a glass window. A glass window allowed visualizing the flow by using some tracer particles; however, as previously mentioned, it was not easy to avoid the settling down problem and, the contrast issue as well. Thus, no figure is displayed with those particles presented.

To overcome the problems that are faced during these experiments using a different binary mixture can be a good proposal for the future. Keep in mind that our model is applicable for ideal mixing and simple mixture property calculations.

CHAPTER 6
CONCLUDING REMARKS AND FUTURE SCOPE

In this chapter a summary of the results with some ideas for possible future works is given.

Evaporative instability in binary mixture was investigated using ethanol and sec-butanol as the two components of the binary mixture. It is shown that due to the concentration dependence of surface tension and density the evaporative instability problem in a binary mixture is more complicated than a single component systems. The research problem is divided into mainly three parts; pure evaporative convection, surface tension driven convection, and the added effect of the gravity. In all of these convective modes having a second component in the system shows its signature on the onset point.

In the pure evaporative convection the onset point has maximum stability with respect to mass fraction for a certain range of wave number. This maximum is the result of a change in the thermo-physical properties with mass fraction even though the mixture properties are calculated by using simple mixing rules.

With the addition of the surface tension gradient effects into the model the binary mixture physics depart greatly from a single component system. It is important to point out that the solutal effects strongly depend on the choice of the components. In the ethanol and sec-butanol mixture the more volatile component ethanol has a lower surface tension; therefore, with increasing ethanol concentration the surface tension of the mixture is lowered. Due to this property, unlike a single component system the binary system can be made unstable by heating from the vapor side, i.e., negative critical temperature difference. The onset point exhibits a strong dependence on the mass fraction and wave number. The mass fraction dependence of the onset point results in a less stable region in the middle range. It is found that this is due to stronger mass fraction perturbations in that region than the remaining mass fraction ranges. The

liquid and vapor heights effect on the onset point show that with increasing vapor height, the system gets more stable while the contrary holds with increasing liquid height i.e., the system get more unstable.

In the last part gravity is introduced into the problem and with introduction of gravity the density gradients start to play a role on the physics. The density of the mixture decreases both by increasing temperature and by increasing ethanol concentration. In this section we start to have two physically realizable possibilities to get an instability in our system; one is by heating from above, i.e., a negative temperature difference, and the second is by heating from below, i.e., a positive critical temperature difference. The instability obtained by heating from above is the consequence of solutal dependence of surface tension and density. As in the absence of gravity the onset point shows a minimum stability region in the middle range of mass fraction. The second possibility, that is heating from the liquid side, occurs on account of the temperature dependence of density much like in a single component system. In this heating arrangement the middle range of mass fraction of the binary mixture is more stable than the rest, i.e. larger positive critical temperature differences obtain until the wave number of the disturbance exceeds a certain level. In the presence of gravity an increase in the vapor height leads to an increase in stability reached a maximum and with further increase of vapor height leads to a decrease in the stability before attaining a second region of stability increase for further height increases. The first rise in stability is due to increase in the thermal resistance of the vapor phase. A further increase in height causes the vapor phase to become gravitationally unstable; finally an increase in the height even more brings about stabilization of the evaporation mode.

The existence of instability when heated from above results are supported by experiments.

The physics of the problem shows that there is a competition between thermal convection modes and solutal convection modes. Nowhere does oscillatory behavior

show its presence at the onset. The oscillatory behavior can be ignited by decreasing the effect of the solutal dependence of the surface tension. In other words, if the two components have a closer surface tension value, we could see oscillations at the onset. Preliminary calculations show that 1-Pentanol and Hexanol binary pair is a good candidate for future investigation of the oscillations. The other point that would be worth investigating is the effect of inerts in both phases such as air in the vapor phase and non-evaporating silicone oil in the liquid phase. Air in the vapor phase will modify the partial pressures and therefore modify the composition at the interface. The presence of oil will greatly modify the viscosity of the liquid bringing the stability to the problem also modify the dynamics of evaporation. Keep in mind that these modifications are not trivial and might require non-ideal mixing to be accounted for in the model as more complicated mixture properties calculations.

Controlling the convective flow in evaporative processes such as thin film evaporation or coating is crucial to ensure quality of the final product. These processes are used to functionalize surfaces such as producing self-cleaning, hydrophobic glasses, and in semiconductor production etc . Also controlling the evaporative convective flow is important in heat pipes to increase the heat transfer, therefore, increase the efficiency of cooling.

APPENDIX A
THERMODYNAMIC EQUILIBRIUM

Consider an evaporating liquid underlying its own vapor at equilibrium. In thermodynamic terms this equilibrium is represented by the equality in specific Gibbs free energies which is given by,

$$\hat{G}^{L} = \hat{G}^{V}$$

where $\hat{G}^{L}$ and $\hat{G}^{V}$ are the liquid and vapor specific Gibbs free energies, respectively.

This relation is valid for any interface shape; therefore, we can write

$$\hat{G}^{L}_{curved} = \hat{G}^{V}_{curved}$$

and

$$\hat{G}^{L}_{flat} = \hat{G}^{G}_{flat}$$

Sum and rearrange the above two equations,

$$\left(\hat{G}^{L}_{curved} - \hat{G}^{L}_{flat}\right) - \left(\hat{G}^{G}_{curved} - \hat{G}^{G}_{flat}\right) = 0$$

The Gibbs free energy is given by

$$d\hat{G} = -\hat{S}dT + \hat{V}dP$$

where $\hat{S}$ and $\hat{V} = \frac{1}{\rho}$are the specific entropy and volume, respectively.

Assuming that the specific entropy and volume do not change much on account of small changes in T and P, we get

$$\left(S^{G} - S^{L}\right) dT + V^{L}dP^{L} - V^{G}dP^{G} = 0$$

Using the ideal gas law, we can write

$$\left(S^{G} - S^{L}\right) dT + V^{L}dP^{L} - \frac{RT}{P^{G}}dP^{G} = 0$$

And inserting $(G^G - G^L) = (H^G - H^L) - (S^G - S^L)T$ into above equation

$$\frac{H^G - H^L}{T}dT + V^L dP^L - \frac{RT}{P^G}dP^G = 0$$

Observe that $H^G - H^L$ is equal to the latent heat of evaporation,$\hbar$. Therefore,

$$\frac{\hbar}{T^2}dT + \frac{V^L}{T}dP^L - \frac{R}{P^G}dP^G = 0$$

We can integrate both sides to get a relation between the temperature and pressure at the interface from the flat to curved states. Hence

$$\int_{T_F}^{T_C} \frac{\hbar}{T^2}dT + \int_{P_F^L}^{P_C^L} \frac{V^L}{T}dP^L - \int_{P_F^G}^{P_C^G} \frac{R}{P^G}dP^G = 0$$

Integration gives,

$$\hbar \left.\frac{1}{T}\right|_{T_F}^{T_C} + \left.\frac{V^L}{T}\right|_{P_F^L}^{P_C^L} - R \ln P\Big|_{P_F^G}^{P_C^G} = 0$$

and

$$\hbar\left(\frac{1}{T_C} - \frac{1}{T_F}\right) + \frac{V^L}{T}\left(\frac{1}{P_C^L} - \frac{1}{P_F^L}\right) - R\left(\ln P_C^G - \ln P_F^G\right) = 0$$

In the equation above the second term shows the pressure change in the liquid phase which is negligible compare to the rest. Therefore, we can write the thermodynamic equilibrium as,

$$\hbar\left(\frac{1}{T_C} - \frac{1}{T_F}\right) - R\left(\ln P_C^G - \ln P_F^G\right) = 0$$

The above equation is called the Clapeyron equation and it gives the vapor pressure of a component as a function of temperature. The vapor pressure of the ideal binary mixture is given by the molar weighted sum of the pure component vapor pressures. This can be done in two ways; first using a Clapeyron equation for each components and take the molar weighted sum or by using a mixture form of the Clapeyron equation. Let's quantify this approach with an example.

As an example assume that the flat state is state 1 and the curved state is state 2 with $T_1 = 303.15K$,$T_2 = 304.15K$

$$P_{eth(2)}^{Vap} = \exp\left(-\left(\left(\frac{\hbar}{R}\right)\left(\frac{1}{T_2} - \frac{1}{T_1}\right) - \ln\left(P_{eth(1)}^{Vap}\right)\right)\right)$$

$$P_{but(2)}^{Vap} = \exp\left(-\left(\left(\frac{\hbar}{R}\right)\left(\frac{1}{T_2} - \frac{1}{T_1}\right) - \ln\left(P_{but(1)}^{Vap}\right)\right)\right)$$

and the vapor pressure of the mixture, or total pressure, is given by,

$$P_2 = P_{eth(2)}^{Vap} \cdot x_{eth} + P_{but(2)}^{Vap}\left(1 - x_{eth}\right)$$

The other way of calculating the total pressure is using the latent heat of the mixture and the vapor pressure of the mixture at state 1.

$$P_{mix(2)}^{Vap} = \exp\left(-\left(\left(\frac{\hbar_{mix}}{R}\right)\left(\frac{1}{T_2} - \frac{1}{T_1}\right) - \ln\left(P_{mix(1)}^{Vap}\right)\right)\right)$$

The difference between these two approaches is less than 0.3 %.

The perturbed version of the Clayperon equation is given by,

$$\prod_{KE} \mathrm{P}_1^* - \prod_{PE} \mathrm{Z}_1 = \frac{\mathrm{T}_1^* + \frac{\mathrm{d}\mathrm{T}_0^*}{\mathrm{dz}}\mathrm{Z}_1}{\mathrm{T}_{\mathrm{base}}^*}$$

where $\prod_{KE}$ and $\prod_{PE}$ are the dimensionless parameters from the linearized Clapeyron equation defined as $\prod_{KE} = \left(\frac{\rho}{\rho^*}\right)\left(\frac{\mu\kappa}{\hbar d^2}\right)$ and $\prod_{PE} = \left(\frac{gd}{\hbar}\right)$.

APPENDIX B
BOUSSINESQ APPROXIMATION

In the Rayleigh problem, it is clear that fluids cannot be strictly incompressible because density variations create the convection. The fact that fluid density is a function of temperature and concentration makes the problem dependent on the heat transfer. For that reason, the Boussinesq approximation is employed. Clearly, density being a function of temperature and also concentration makes the Rayleigh problem very complicated. This approximation allows a fluid to be treated as incompressible in all terms of the momentum equation except those multiplied by gravity.

In other words, in the Boussinesq approximation the density of a fluid is a function of temperature and concentration only when it is multiplied by gravity, in the rest of the terms density is taken as constant.

Boussinesq approximation is given by,

$$\rho = \rho_R \left(1 + \frac{1}{\rho_R} \frac{\partial \rho}{\partial T}\bigg|_{T_R} (T - T_R) + \frac{1}{\rho_R} \frac{\partial \rho}{\partial \omega_A}\bigg|_{\omega_{A_R}} (\omega_A - \omega_{A_R}) \right)$$

here $\frac{1}{\rho_R}\frac{\partial \rho}{\partial T}\Big|_{T=T_R}$ and $\frac{1}{\rho_R}\frac{\partial \rho}{\partial \omega}\Big|_{\omega=\omega_R}$ are the density variation of temperature and concentration with subscript R represents a reference state. Let us apply Bossinesq approximation to a momentum equation given below

$$\rho \frac{\partial \vec{v}}{\partial t} + \rho \vec{v} \cdot \nabla \vec{v} = -\nabla P + \rho \vec{g} + \nabla \cdot \vec{\vec{S}}$$

Upon employing the approximation we have

$$\rho_R \frac{\partial \vec{v}}{\partial t} + \rho_R \vec{v} \cdot \nabla \vec{v} = -\nabla P + \rho_R \left(1 + \frac{1}{\rho_R} \frac{\partial \rho}{\partial T}\bigg|_{T_R} (T - T_R) + \frac{1}{\rho_R} \frac{\partial \rho}{\partial \omega_A}\bigg|_{\omega_{A_R}} (\omega_A - \omega_{A_R}) \right) \vec{g} + \nabla \cdot \vec{\vec{S}}$$

$\beta_T = -\frac{1}{\rho}\frac{\partial \rho}{\partial T}\Big|_{T=T_R}$ and $\beta_\omega = -\frac{1}{\rho}\frac{\partial \rho}{\partial \omega}\Big|_{\omega=\omega_R}$ with $\beta_T \& \beta_\omega$ are positive when the derivative of density with respect to temperature and concentration are negative.

APPENDIX C
RAOULT'S LAW

To derive the Raoult's law for vapor-liquid equilibrium in a multi-component system we assume that the vapor phase behaves as an ideal gas and the liquid phase as an ideal solution. The equilibrium defined as the equality of the chemical potentials, is given by

$$\varphi_A^L = \varphi_A^V$$

For an ideal liquid mixture we can write

$$\varphi_A^L = \varphi_A^{0,L}(T, P_A) + RT \ln x_A$$

$$\varphi_A^L = \varphi_A^{0,L}(T, P_{A^{vap}}) + \int_{P_{A^{vap}}}^{P_A} \frac{\partial \varphi_A^{0,L}(T, P'_A)}{\partial P} dP' + RT \ln x_A$$

where $\frac{\partial \varphi_A^{0,L}(T, P'_A)}{\partial P} = V_A^{0,L}$, is the molar volume of pure liquid A and if we assume the liquid volume is not changing with pressure the above equation becomes

$$\varphi_A^L = \varphi_A^{0,L}(T, P_A^{vap}) + V_A^{0,L}(P - P_A^{vap}) + RT \ln x_A$$

The same derivation is valid for the vapor phase but for the vapor phase we need to employ the ideal gas law to calculate the volume change with respect to pressure change. The chemical potential of an ideal vapor phase is given by,

$$\varphi_A^V = \varphi_A^{0,V}(T, P_A^{vap}) + RT \ln\left(\frac{P}{P_A^{vap}}\right) + RT \ln y_A$$

Recall that $\varphi_A^L = \varphi_A^V$ and also $\varphi_A^{0,L}(T, P_A^{vap}) = \varphi_A^{0,V}(T, P_A^{vap})$ leads to

$$V_A^{0,L}(P - P_A^{vap}) + RT \ln x_A = RT \ln\left(\frac{P}{P_A^{vap}}\right) + RT \ln y_A$$

after rearranging we get,

$$y_A P = x_A P_A^{vap} \exp\left[\frac{V_A^{0,L}(P - P_A^{vap})}{RT}\right]$$

The exponential term is called the Poynting factor which is close to 1 for most of the systems at low pressures. And the Raoult's law in its final from for ideal vapor and ideal liquid mixture is given by,

$$y_A P = x_A P_A^{vap}$$

For the systems where the liquid and the vapor phases cannot be assumed ideal a modified Raoult's law should be used. The modified Raoult's law and the definition of the terms are giving below to give an idea to the reader; although, non-ideal systems are not discussed in this study.

$$\widehat{\phi}_A y_A P = \gamma_A \phi_A^{vap} x_A P_A^{vap} \exp\left[\frac{V_A^{0,L}(P - P_A^{vap})}{RT}\right]$$

Where;

$\widehat{\phi}_A$ is the fugacity coefficient of A in mixture at given T and P, accounts for non-ideality in the mixture.

γ_A is the activity coefficient for A in mixture at T, P can be a function of all x_A, T, and P accounts for non-ideality in liquid mixture.

ϕ_A^{vap} is the fugacity coefficient for pure A at T, P^{vap}.

APPENDIX D
DERIVATION OF THE UNIT NORMAL AND THE INTERFACE SPEED FOR 1-D SYSTEM

Let a surface be denoted by

$$f = z - Z(x, t) = 0$$

Then, f, is positive on one side of $f = 0$, negative on the other, and the normal pointing into the region where f is positive given by,

$$\vec{n} = \frac{\nabla f}{|\nabla f|}$$

Here,

$$\nabla f = \frac{\partial f}{\partial x}\vec{i} + \frac{\partial f}{\partial x}\vec{k}$$

Then, the equation for the normal stress balance is given by

$$\vec{n} = \frac{-\frac{\partial Z}{\partial x}\vec{i} + \vec{k}}{\left[1 + \left(\frac{\partial Z}{\partial x}\right)^2\right]^{1/2}}$$

The derivation of the unit tangent vector is straightforward using the definition $\vec{n} \cdot \vec{t} = 0$ from which we get

$$\vec{t} = \frac{\vec{i} + \frac{\partial Z}{\partial x}\vec{k}}{\left[1 + \left(\frac{\partial Z}{\partial x}\right)^2\right]^{1/2}}$$

To get the interface speed, let a surface be denoted by,

$$f(\vec{r}, t) = 0$$

$\vec{r} = \vec{r}(x, y, z)$. Recall unit normal of the surface is given by $\vec{n} = \frac{\nabla f}{|\nabla f|}$

Let the surface move a small distance Δs along its normal in time Δt. Then, $f(\vec{r} \pm \Delta s\vec{n}, t + \Delta t)$ is given by,

$$f(\vec{r} \pm \Delta s\vec{n}, t + \Delta t) = f(\vec{r}, t) \pm \Delta s\vec{n} \cdot \nabla f(\vec{r}, t) + \Delta t\frac{\partial f(\vec{r}, t)}{\partial \mathrm{t}} + \ldots$$

whence $f(\vec{r} \pm \Delta s\vec{n}, t + \Delta t) = 0 = f(\vec{r}, t)$ requires

$$\pm \Delta s\vec{n} \cdot \nabla f(\vec{r}, t) = -\Delta t \frac{\partial f(\vec{r}, t)}{\partial \mathrm{t}}$$

The normal speed of the surface, u, is then given by,

$$\vec{u} = \pm \frac{\Delta s}{\Delta t} = -\frac{\frac{\partial f(\vec{r},t)}{\partial t}}{\vec{n} \cdot \nabla f(\vec{r}, t)}$$

Now, using the definition of the unit normal given earlier we get

$$\vec{u} = -\frac{\frac{\partial f}{\partial t}}{|\nabla f|}$$

In our problems, the definition of u becomes

$$\vec{u} = \frac{\frac{\partial Z}{\partial t}}{\left(\left(\frac{\partial Z}{\partial x}\right)^2 + 1\right)^{1/2}}$$

APPENDIX E
ENERGY BALANCE FOR 1-D BINARY SYSTEM

The energy balance in its raw form is given by,

$$\left[(\vec{v}-\vec{u})\,\rho\left(\widehat{U}+\frac{1}{2}\vec{v}^2\right)+\vec{q}-\vec{\vec{T}}\cdot\vec{v}\right]\cdot\vec{n}+\gamma 2H\vec{n}\cdot\vec{u}=\left[(\vec{v}^*-\vec{u})\,\rho^*\left(\widehat{U}^*+\frac{1}{2}\vec{v}^{*^2}\right)+\vec{q}^*-\vec{\vec{T}}^*\cdot\vec{v}\right]$$

and the momentum balance by,

$$\left[(\vec{v}-\vec{u})\,\rho\vec{v}-\vec{\vec{T}}\right]\cdot\vec{n}+\gamma 2H\vec{n}=\left[(\vec{v}^*-\vec{u})\,\rho^*\vec{v}^*-\vec{\vec{T}}^*\right]\cdot\vec{n}$$

In order to convert the energy balance into an observer invariant form the dot product of the momentum balance with $\vec{u}$ is subtracted from the energy balance. Working only with the right hand side of the equations we get

$$\left[(\vec{v}-\vec{u})\,\rho+(\vec{v}-\vec{u})\,\rho\left(\frac{1}{2}\vec{v}^2-\vec{v}\cdot\vec{u}\right)+\vec{q}-\vec{\vec{T}}\cdot(\vec{v}-\vec{u})\right]\cdot\vec{n}$$

Using the definition of $\vec{\vec{T}}$ the stress tensor, $\vec{\vec{T}}=-P\vec{\vec{I}}+\vec{\vec{S}}$, we get

$$\left[(\vec{v}-\vec{u})\,\rho+(\vec{v}-\vec{u})\,\rho\left(\frac{1}{2}\vec{v}^2-\vec{v}\cdot\vec{u}\right)+\vec{q}-\left(-P\vec{\vec{I}}+\vec{\vec{S}}\right)\cdot(\vec{v}-\vec{u})\right]\cdot\vec{n}$$

and using the internal energy definition, $\widehat{H}=\widehat{U}+\frac{P}{\rho}$ we get

$$\left[(\vec{v}-\vec{u})\,\rho+(\vec{v}-\vec{u})\,\rho\left(\frac{1}{2}(\vec{v}-\vec{u})^2-\frac{1}{2}\vec{u}^2\right)+\vec{q}-\vec{\vec{S}}\cdot(\vec{v}-\vec{u})\right]\cdot\vec{n}$$

The $(\vec{v}-\vec{u})$ is an observer invariant term but $\vec{u}^2$ term is not observer invariant, however, employing

$$\frac{1}{2}(\vec{v}-\vec{u})^2-\frac{1}{2}\vec{u}^2=\frac{1}{2}\vec{v}^2-\vec{v}\cdot\vec{u}\rightarrow\frac{1}{2}\left(\vec{v}^2-2\vec{v}\vec{u}+\vec{u}^2\right)-\frac{1}{2}\vec{u}^2=\frac{1}{2}\vec{v}^2-\vec{v}\cdot\vec{u}$$

and from the total mass balance $\frac{1}{2}(\vec{v}-\vec{u})\,\rho\vec{u}^2=\frac{1}{2}(\vec{v}^*-\vec{u})\,\rho^*\vec{u}^2$.

We get the observer invariant energy balance,

$$\left[(\vec{v}-\vec{u})\,\rho\left(\widehat{H}+\frac{1}{2}(\vec{v}-\vec{u})^2\right)+\vec{q}-\vec{\vec{S}}\cdot(\vec{v}-\vec{u})\right]\cdot\vec{n}\ldots$$

$$= \left[(\vec{v}^* - \vec{u})\, \rho^* \left(\widehat{H}^* + \frac{1}{2} (\vec{v}^* - \vec{u})^2 \right) + \vec{q}^* - \vec{\vec{S}}^* \cdot (\vec{v}^* - \vec{u}) \right] \cdot \vec{n}$$

For a binary mixture $\vec{q} = -\lambda \nabla T + \sum_i^N J_i \widehat{H}_i$ and the total mixture enthalpy is $= \sum_i^N \omega_i \widehat{H}_i$.

Observe that for individual components the reference states enthalpies for liquid and vapor are the same; therefore, reference states cancel out from left hand side to right hand side.

For now let us just work with $\left[(\vec{v} - \vec{u})\, \rho \widehat{H} \right] \cdot \vec{n}, \vec{n} \cdot \sum_i^N J_i \widehat{H}_i$ from the left hand side (LHS) and with $\left[(\vec{v}^* - \vec{u})\, \rho^* \widehat{H}_i^* \right] \cdot \vec{n}, \vec{n} \cdot \sum_i^N J_i^* \widehat{H}_i^*$ from the right hand side (RHS). For a binary mixture using the above relations

$$\left[\widehat{H}_A \left(\underline{\rho \omega_A (\vec{v} - \vec{u})} + \underline{\underline{J_A}} \right) + \widehat{H}_B \left(\rho \omega_B (\vec{v} - \vec{u}) + J_B \right) \right]^{LHS}$$

and

$$\left[\widehat{H}_A^* \left(\underline{\rho^* \omega_A^* (\vec{v}^* - \vec{u})} + \underline{\underline{J_A^*}} \right) + \widehat{H}_B^* \left(\rho^* \omega_B^* (\vec{v}^* - \vec{u}) + J_B^* \right) \right]^{RHS}$$

by using component balance, $\underline{\rho \omega_A (\vec{v} - \vec{u})} + \underline{\underline{J_A}} = \underline{\rho^* \omega_A^* (\vec{v}^* - \vec{u})} + \underline{\underline{J_A^*}}$ for combining the LHS and RHS (This is also valid for component B). The nonlinear energy balance at the interface for an ideal binary mixture becomes,

$$\left[\left(\widehat{H}_A - \widehat{H}_A^* \right) (\rho \omega_A (\vec{v} - \vec{u}) + J_A) + \left(\widehat{H}_B - \widehat{H}_B^* \right) (\rho \omega_B (\vec{v} - \vec{u}) + J_B) \right] \cdot \vec{n} + \ldots$$

$$\left[\rho (\vec{v} - \vec{u}) \frac{1}{2} (\vec{v} - \vec{u})^2 + (-\lambda \nabla T) - \vec{\vec{S}} \cdot (\vec{v} - \vec{u}) \right] \cdot \vec{n} \ldots$$

$$= \left[\rho^* (\vec{v}^* - \vec{u}) \frac{1}{2} (\vec{v}^* - \vec{u})^2 + (-\lambda^* \nabla T^*) - \vec{\vec{S}}^* \cdot (\vec{v}^* - \vec{u}) \right] \cdot \vec{n}$$

Here $-\left(\widehat{H}_A - \widehat{H}_A^* \right) = \hbar_A$ is the latent heat of the component A and $-\left(\widehat{H}_B - \widehat{H}_B^* \right) = \hbar_B$ is the latent heat of the component B.

$$\left[-\hbar_A (\rho \omega_A (\vec{v} - \vec{u}) + J_A) - \hbar_B (\rho \omega_B (\vec{v} - \vec{u}) + J_B) \right] \cdot \vec{n} + \ldots$$

$$\left[\rho (\vec{v} - \vec{u}) \frac{1}{2} (\vec{v} - \vec{u})^2 + (-\lambda \nabla T) - \vec{\vec{S}} \cdot (\vec{v} - \vec{u}) \right] \cdot \vec{n}$$

$$= \left[\rho^* \left(\vec{v}^* - \vec{u}\right) \frac{1}{2} \left(\vec{v}^* - \vec{u}\right)^2 + \left(-\lambda^* \nabla T^*\right) - \vec{\vec{S}}^* \cdot \left(\vec{v}^* - \vec{u}\right)\right] \cdot \vec{n}$$

Scaling the energy balance term by term gives

$$\left\{1 + K_{PC} \left[\frac{1}{2} \left(\vec{v} - \vec{u}\right)^2 - \frac{1}{2} \left(\vec{v}^* - \vec{u}\right)^2\right]\right\} \left(\vec{v} - \vec{u}\right) \cdot \vec{n} + E_2 \nabla \omega_A \cdot \vec{n} + \ldots$$

$$-V_{PC} \left[\vec{\vec{S}} \cdot \left(\vec{v} - \vec{u}\right) - \frac{\mu^*}{\mu} \vec{\vec{S}}^* \cdot \left(\vec{v}^* - \vec{u}\right)\right] \cdot \vec{n} - E_1 \left(\nabla T - \frac{\lambda^*}{\lambda} \nabla T^*\right) \cdot \vec{n} = 0$$

where

$$K_{PC} = \frac{\kappa^2}{d^2 \left(-\hbar_A \omega_A - \hbar_B \omega_B\right)}$$

$$V_{PC} = \frac{\nu \kappa}{d^2 \left(-\hbar_A \omega_A - \hbar_B \omega_B\right)}$$

$$E_1 = \frac{\lambda \Delta T}{\kappa \rho \left(-\hbar_A \omega_A - \hbar_B \omega_B\right)}$$

$$E_2 = \frac{D_{AB} \left(\hbar_A - \hbar_B\right)}{\kappa \left(-\hbar_A \omega_A - \hbar_B \omega_B\right)}$$

APPENDIX F
COMPONENT BALANCE FOR 1-D BINARY SYSTEM

The component balance in raw from is given by,

$$\rho_{\mathrm{A}} \left(\vec{v}_A - \vec{u} \right) \cdot \vec{n} = \rho_A^* \left(\vec{v}_A^* - \vec{u} \right) \cdot \vec{n}$$

where ρ_A is the density of component A and $\vec{v}_A$ is the component velocity at the interface. Because of the component velocity term the component balance is not user friendly in this representation; therefore, to reach more usable form of the component balance we add and subtract $\vec{v}$ from right hand side and add and subtract $\vec{v}^*$ from left hand side.

$$\rho_{\mathrm{A}} \left(\vec{v}_A - \vec{v} + \vec{v} - \vec{u} \right) \cdot \vec{n} = \rho_A^* \left(\vec{v}_A^* - \vec{v} + \vec{v} - \vec{u} \right) \cdot \vec{n}$$

Here we can define the mass flux as $J_A = \rho_{\mathrm{A}} \left(\vec{v}_A - \vec{v} \right) = \rho \omega_{\mathrm{A}} \left(\vec{v}_A - \vec{v} \right)$ and put the component balance in its final nonlinear form.

$$J_A \cdot \vec{n} + \rho \omega_{\mathrm{A}} \left(\vec{v} - \vec{u} \right) \cdot \vec{n} = J_A^* \cdot \vec{n} + \rho^* \omega_A^* \left(\vec{v}^* - \vec{u} \right) \cdot \vec{n}$$

Upon scaling component balance becomes,

$$\left[-\nabla \omega_A + Le \omega_{\mathrm{A}} \left(\vec{v} - \vec{u} \right) \right] \cdot \vec{n} = \frac{\rho^*}{\rho} \left[-\frac{D_{AB}^*}{D_{AB}} \nabla \omega_A^* + Le \omega_A^* \left(\vec{v}^* - \vec{u} \right) \right] \cdot \vec{n}$$

Note that $J_A = -\rho D_{AB} \nabla \omega_A$

APPENDIX G
SORET EFFECT FOR 1-D BINARY SYSTEM

The Soret effect also called thermodiffusion, is the diffusion of the species in a multi-component mixture when the system is subject to a temperature gradient. For positive Soret coefficient, the heavy particles move from hot to cold region and vice versa. The Soret coefficient is a function of both temperature and concentration where the sign of the coefficient can also change depending on both temperature and concentration.

Introducing the Soret effect to our base model would only modifies the equations that has the mass flux term, J_A,

$$J_A = -\rho \left(D_{AB} \nabla \omega_A + D_T \omega_{A_0} \left(1 - \omega_{A_0} \right) \nabla T \right)$$

where D_T is the thermal diffusion term.

The Soret effect modifies total 6 equations in our system; the concentration balance equations in both phases, bottom and top boundary conditions on concentration, and the two interface conditions.

The liquid phase non-linear concentration balance with the Soret effect is

$$\frac{\partial \omega_A}{\partial t} + \vec{v} \cdot \nabla \omega_A = -\frac{1}{\rho} \nabla J_A$$

$$\frac{\partial \omega_A}{\partial t} + \vec{v} \cdot \nabla \omega_A = D_{AB} \nabla^2 \omega_A + D_T \omega_{A_0} \left(1 - \omega_{A_0} \right) \nabla^2 T$$

Upon scaling the liquid phase non-linear concentration balance we get,

$$\frac{\partial \omega_A}{\partial t} + \vec{v} \cdot \nabla \omega_A = \frac{1}{Le} \left(\nabla^2 \omega_A + \left(S_T \Delta T \right) \nabla^2 T \right)$$

where $S_T = \dfrac{D_T}{D_{AB}} \omega_{A_0} \left(1 - \omega_{A_0} \right)$ is called the Soret coefficient and the linearized concentration balance given by

$$\frac{\partial \omega_{A1}^*}{\partial t} + \vec{v}^* \cdot \nabla \omega_{A1}^* = \frac{D_{AB}^*}{D_{AB}} \frac{1}{Le} \left(\nabla^2 \omega_{A1}^* + \left(S_T^* \Delta T \right) \nabla^2 T_1^* \right)$$

Likewise, the vapor phase scaled non-linear concentration balance is given by,

$$\frac{\partial \omega_A^*}{\partial t} + \vec{v}^* \cdot \nabla \omega_A^* = \frac{D_{AB}^*}{D_{AB}} \frac{1}{Le} \left(\nabla^2 \omega_A^* + \left(S_T^* \Delta T \right) \nabla^2 T^* \right)$$

In it's linear from

$$\frac{\partial \omega_{A1}^*}{\partial t} + \vec{v}^* \cdot \nabla \omega_{A1}^* = \frac{D_{AB}^*}{D_{AB}} \frac{1}{Le} \left(\nabla^2 \omega_{A1}^* + \left(S_T^* \Delta T \right) \nabla^2 T_1^* \right)$$

The top and bottom boundary conditions on mass fraction are

$$J_A^* \cdot \vec{n} = \frac{\partial \omega_A^*}{\partial z} + \frac{D_T^*}{D_{AB}^*} \omega_{A_0}^* \left(1 - \omega_{A_0}^* \right) \frac{\partial T^*}{\partial z} = 0 \rightarrow \frac{\partial \omega_{A1}^*}{\partial z} + \left(S_T^* \Delta T \right) \frac{\partial T_1^*}{\partial z} = 0$$

and

$$J_A \cdot \vec{n} = \frac{\partial \omega_A}{\partial z} + \frac{D_T}{D_{AB}} \omega_{A_0} \left(1 - \omega_{A_0} \right) \frac{\partial T}{\partial z} = 0 \rightarrow \frac{\partial \omega_{A1}}{\partial z} + \left(S_T \Delta T \right) \frac{\partial T_1}{\partial z} = 0$$

There are two interface conditions left that needs modification due to the mass flux term and one of them is the component balance and in its non-linear form it is given by,

$$J_A \cdot \vec{n} + \rho \omega_{\mathrm{A}} \left(\vec{v} - \vec{u} \right) \cdot \vec{n} = J_A^* \cdot \vec{n} + \rho^* \omega_A^* \left(\vec{v}^* - \vec{u} \right) \cdot \vec{n}$$

and the linear form is given by,

$$-\frac{\partial \omega_{A1}}{\partial z} - \left(S_T \Delta T \right) \frac{\partial T_1}{\partial z} + Le \omega_{A0} \left(v_{z1} - \frac{\partial Z_1}{\partial t} \right) = \ldots$$

$$-\frac{\rho^*}{\rho} \frac{D_{AB}^*}{D_{AB}} \left(\frac{\partial \omega_{A1}^*}{\partial z} + \left(S_T^* \Delta T \right) \frac{\partial T_1^*}{\partial z} \right) + \frac{\rho^*}{\rho} Le \omega_{A0}^* \left(v_{z1}^* - \frac{\partial Z_1}{\partial t} \right)$$

The last equation that requires modification when the Soret effect is present is the energy balance at the interface i.e.,

$$\frac{\partial \omega_{A_1}}{\partial z} + Le \frac{\left(-\hbar_A \omega_{\mathrm{A}_0} + \hbar_B \left(\omega_{A_0} - 1 \right) \right)}{\left[\hbar_A - \hbar_B \right]} \left[v_{z_1} - \frac{\partial Z_1}{\partial t} \right] + \left(S_T \Delta T \right) \frac{\partial T_1}{\partial z} = \ldots$$

$$\frac{\Delta T}{\left(\rho D_{AB} \left[\hbar_A - \hbar_B \right] \right)} \left(\lambda \frac{\partial T_1}{\partial z} - \lambda^* \frac{\partial T_1^*}{\partial z} \right)$$

APPENDIX H
3-D SCALED LINEAR EQUATIONS FOR SINGLE COMPONENT SYSTEM

In this Appendix we will give only the scaled linear form of the 3-D modeling equations of the system that is depicted in Figure H-1. The figure represents the closed impermeable container with a conductive top plate, at $z = \delta$, a conductive bottom plate, at $z = -1$, and an insulated sidewall at $r = ASP$. The liquid-vapor interface is located at $z = 0$.

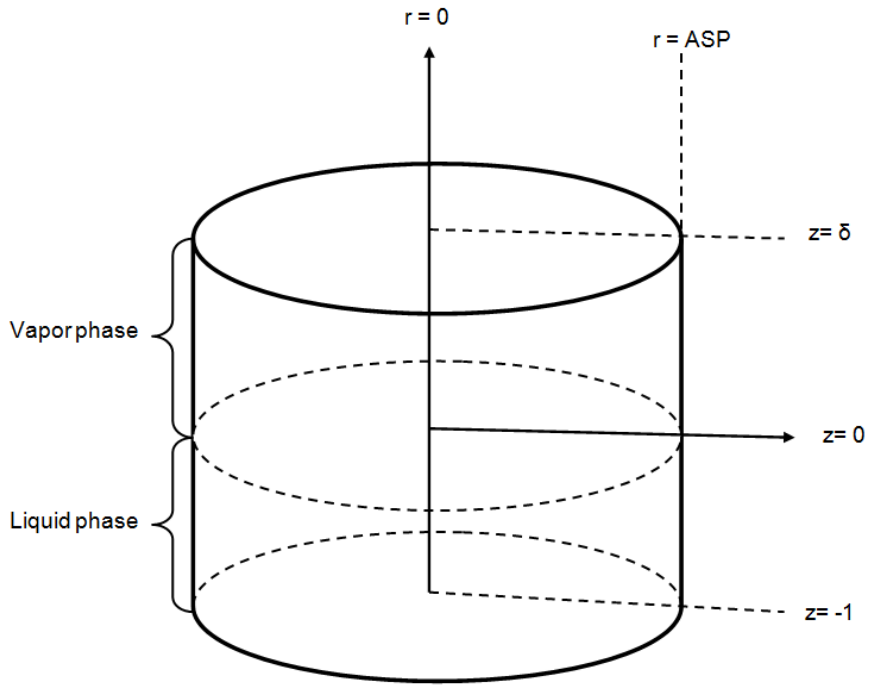

Figure H-1. 3-D model illustration.

Before giving the linear modeling equations let us first introduce the unit normal, unit tangents, and the surface speed for 3-D system. The derivations of these vectors are similar to 1-D system.

$$\vec{n} = \frac{\vec{i}_z - \frac{\partial Z}{\partial r}\vec{i}_r - \frac{\partial Z}{\partial \theta}\vec{i}_\theta}{\left(1 + \left(\frac{\partial Z}{\partial r}\right)^2 + \frac{1}{r}\left(\frac{\partial Z}{\partial \theta}\right)^2\right)^{1/2}}$$

$$\vec{t}_1 = \frac{\frac{\partial Z}{\partial \theta}\frac{1}{r}\vec{i}_z + \vec{i}_\theta}{\left(\left(\frac{\partial Z}{\partial \theta}\right)^2 + 1\right)^{1/2}} \;\&\; \vec{t}_2 = \frac{\frac{\partial Z}{\partial r}\vec{i}_z + \vec{i}_r}{\left(1 + \left(\frac{\partial Z}{\partial r}\right)^2\right)^{1/2}}$$

and

$$\vec{u} = \frac{\frac{\partial Z}{\partial t}}{\left(1 + \left(\frac{\partial Z}{\partial r}\right)^2 + \frac{1}{r}\left(\frac{\partial Z}{\partial \theta}\right)^2\right)^{1/2}}$$

Above $\vec{i}_z$, $\vec{i}_r$, and $\vec{i}_\theta$ are the unit vectors in positive z, r, and θ direction. Linearization and scaling are done in the same manner with 1-D model; however, in the normal mode expansion here we use $U_1 = \hat{U}_1(z, r)e^{\sigma t}e^{im\theta}$ where m represent azimuthal symmetry of the solution and σ is still the growth constant. Due to this azimuthal expansion there are no derivatives in the following equations.

Liquid phase momentum balance, energy balance, and total continuity in their linearized and scaled forms are given by,

$$\frac{\sigma}{\mathrm{Pr}}v_{r1} = -\frac{1}{\chi}\frac{\partial P_1}{\partial r} + \frac{1}{\chi^2}\left(\frac{\partial^2 v_{r1}}{\partial r^2} + \frac{1}{r}\frac{\partial v_{r1}}{\partial r} - \frac{m^2}{r^2}v_{r1} - \frac{v_{r1}}{r^2} - 2imv_{\theta 1}\right) + \frac{\partial^2 v_{r1}}{\partial z^2}$$

$$\frac{\sigma}{\mathrm{Pr}}v_{\theta 1} = -\frac{1}{\chi}\frac{1}{r}imP_1 + \frac{1}{\chi^2}\left(\frac{\partial^2 v_{\theta 1}}{\partial r^2} + \frac{1}{r}\frac{\partial v_{\theta 1}}{\partial r} - \frac{m^2}{r^2}v_{\theta 1} - \frac{v_{\theta 1}}{r^2} + \frac{2im}{r^2}v_{r1}\right) + \frac{\partial^2 v_{\theta 1}}{\partial z^2}$$

$$\frac{\sigma}{\mathrm{Pr}}v_{z1} = -\frac{\partial P_1}{\partial z} + \frac{1}{\chi^2}\left(\frac{\partial^2 v_{z1}}{\partial r^2} + \frac{1}{r}\frac{\partial v_{z1}}{\partial r} - \frac{m^2}{r^2}v_{z1}\right) + \frac{\partial^2 v_{z1}}{\partial z^2} + RaT$$

$$\frac{\sigma}{\mathrm{Pr}}T_1 + v_{z1}\frac{dT_0}{dz_0} = \frac{1}{\chi^2}\left(\frac{\partial^2 T_1}{\partial r^2} + \frac{1}{r}\frac{\partial T_1}{\partial r} - \frac{m^2}{r^2}T_1\right) + \frac{\partial^2 T_1}{\partial z^2}$$

and

$$\frac{1}{\chi r}\frac{\partial (rv_{r1})}{\partial r} + \frac{1}{\chi r}\frac{\partial v_{\theta 1}}{\partial \theta} + \frac{\partial v_{z1}}{\partial z} = 0$$

In above equations χ is the aspect ratio.

Likewise in the vapor phase the momentum and energy balances with total continuity are given by,

$$\frac{\nu}{\nu^*}\frac{\sigma}{\mathrm{Pr}}v^*_{r1} = -\frac{\mu}{\mu^*}\frac{1}{\chi}\frac{\partial P_1}{\partial r} + \frac{1}{\chi^2}\left(\frac{\partial^2 v^*_{r1}}{\partial r^2} + \frac{1}{r}\frac{\partial v^*_{r1}}{\partial r} - \frac{m^2}{r^2}v^*_{r1} - \frac{v^*_{r1}}{r^2} - 2imv^*_{\theta 1}\right) + \frac{\partial^2 v^*_{r1}}{\partial z^2}$$

$$\frac{\nu}{\nu^*}\frac{\sigma}{\mathrm{Pr}}v^*_{\theta 1} = -\frac{\mu}{\mu^*}\frac{1}{\chi}\frac{1}{r}imP_1 + \frac{1}{\chi^2}\left(\frac{\partial^2 v^*_{\theta 1}}{\partial r^2} + \frac{1}{r}\frac{\partial v^*_{\theta 1}}{\partial r} - \frac{m^2}{r^2}v^*_{\theta 1} - \frac{v^*_{\theta 1}}{r^2} + \frac{2im}{r^2}v^*_{r1}\right) + \frac{\partial^2 v^*_{\theta 1}}{\partial z^2}$$

$$\frac{\nu}{\nu^*}\frac{\sigma}{\mathrm{Pr}}v^*_{z1} = -\frac{\mu}{\mu^*}\frac{\partial P_1}{\partial z} + \frac{1}{\chi^2}\left(\frac{\partial^2 v^*_{z1}}{\partial r^2} + \frac{1}{r}\frac{\partial v^*_{z1}}{\partial r} - \frac{m^2}{r^2}v^*_{z1}\right) + \frac{\partial^2 v^*_{z1}}{\partial z^2} + \frac{\nu}{\nu^*}\frac{\beta^*_T}{\beta_T}RaT^*_1$$

$$\frac{\sigma}{\mathrm{Pr}}T^*_1 + v^*_{z1}\frac{dT^*_0}{dz_0} = \frac{\kappa^*}{\kappa}\frac{1}{\chi^2}\left(\frac{\partial^2 T^*_1}{\partial r^2} + \frac{1}{r}\frac{\partial T^*_1}{\partial r} - \frac{m^2}{r^2}T^*_1\right) + \frac{\kappa^*}{\kappa}\frac{\partial^2 T^*_1}{\partial z^2}$$

and

$$\frac{1}{\chi r}\frac{\partial(rv^*_{r1})}{\partial r} + \frac{1}{\chi r}\frac{\partial v^*_{\theta 1}}{\partial \theta} + \frac{\partial v^*_{z1}}{\partial z} = 0$$

We need a total of 16 boundary conditions and also a condition to identify the surface deflection, Z_1.

The solid bottom wall with uniform temperature give rise to, at $z = -1$,

$$v_{r1} = 0 = v_{\theta 1} = v_{z1} = T_1$$

and likewise the top wall, at $z = \delta$

$$v^*_{r1} = 0 = v^*_{\theta 1} = v^*_{z1} = T^*_1$$

The periodic sidewall conditions for the liquid and vapor phases are, at $r = \chi$

$$v_{r1} = 0 = \frac{\partial(rv_{\theta 1})}{\partial r} = \frac{\partial v_{z1}}{\partial r} = \frac{\partial T_1}{\partial r}$$

and

$$v^*_{r1} = 0 = \frac{\partial(rv^*_{\theta 1})}{\partial r} = \frac{\partial v^*_{z1}}{\partial r} = \frac{\partial T^*_1}{\partial r}$$

For non-periodic sidewall the boundary conditions for both phases are given by,

$$v_{r1} = 0 = v_{\theta 1} = v_{z1} = \frac{\partial T_1}{\partial r}$$

and

$$v_{r1}^* = 0 = v_{\theta 1}^* = v_{z1}^* = \frac{\partial T_1^*}{\partial r}$$

The total mass balance and the continuity of the temperature at the interface given by

$$\rho v_{z1} - \rho^* v_{z1}^* = \sigma(\rho - \rho^*) Z_1$$

and

$$T_1 + \frac{dT_0}{dz} Z_1 = T_1^* + \frac{dT_0^*}{dz} Z_1$$

At the interface the tangential components of the velocities of both fluids are equal to each other, i.e., no-slip conditions

$$v_{r1} = v_{r1}^*$$

$$v_{\theta 1} = v_{\theta 1}^*$$

The tangential stress balances assume the following linear dimensionless form

$$-\frac{\mu}{\mu^*}\left(\frac{\partial v_{r1}^*}{\partial z} + \frac{1}{\chi}\frac{\partial v_{z1}^*}{\partial r}\right) + \left(\frac{\partial v_{r1}}{\partial z} + \frac{1}{\chi}\frac{\partial v_{z1}}{\partial r}\right) + \frac{1}{\chi} Ma \left(\frac{\partial T_1}{\partial r} + \frac{dT_0}{dz}\frac{\partial Z_1}{\partial r}\right) = 0$$

$$-\frac{\mu}{\mu^*}\left(\frac{\partial v_{\theta 1}^*}{\partial z} + \frac{im}{\chi} v_{z1}^*\right) + \left(\frac{\partial v_{\theta 1}}{\partial z} + \frac{im}{\chi} v_{z1}\right) + \frac{1}{\chi}\frac{im}{r} Ma \left(T_1 + \frac{dT_0}{dz} Z_1\right) = 0$$

where $Ma = \frac{\gamma_T \Delta T d}{\mu \kappa}$ is the thermal Marangoni number.

The energy balance at the interface is

$$v_{z1} - E\left(\frac{\lambda^*}{\lambda}\frac{dT_1^*}{dz} - \frac{dT_1}{dz}\right) = \sigma Z_1$$

Here E stands for the Evaporation number and is given by $E = \dfrac{\lambda \Delta T}{\rho \hbar \kappa}$.

The local thermodynamic equilibrium condition at the interface leads to Clausius-Clapeyron, i.e.,

$$\prod\nolimits_{KE} P_1^* - \prod\nolimits_{PE} Z_1 = \frac{T_1^* + \frac{dT_0^*}{dz} Z_1}{T_0^*}$$

where $\prod_{KE}$ and $\prod_{PE}$ are the dimensionless parameters from the linearized Clapeyron equation defined as $\prod_{KE} = \left(\frac{\rho}{\rho^*}\right)\left(\frac{\mu\kappa}{\hbar d^2}\right)$ and $\prod_{PE} = \left(\frac{gd}{\hbar}\right)$.

The last equation to close the system is the normal stress balance is .

$$Ca(P_1 - P_1^*) + BoZ_1 - 2Ca\left(\frac{dv_{z1}}{dz} - \frac{\mu^*}{\mu}\frac{dv_{z1}^*}{dz}\right) + \frac{1}{\chi^2}\left(\frac{d^2Z_1}{dr^2} + \frac{1}{r}\frac{dZ_1}{dr} - \frac{m^2}{r^2}Z_1\right) = 0$$

where $Ca = \frac{\mu\kappa}{d\gamma}$ and $Bo = \frac{(\rho - \rho^*)gd^3}{\gamma}$ are the Capillary number and the Bond number.

APPENDIX I
MODIFICATIONS TO THE 3-D MODEL FOR NON-CONSTANT VISCOSITY

In this part of the appendix we present the modifications for non-constant viscosity for a single component system in 3-D. Although, viscosity is a non-linear function of temperature for a large range of temperature change, shown in Figure I-1, it can be represented as a linear function of temperature for a smaller range of temperature, shown in Figure I-2. This approach will simply the derivation and the coding considerably.

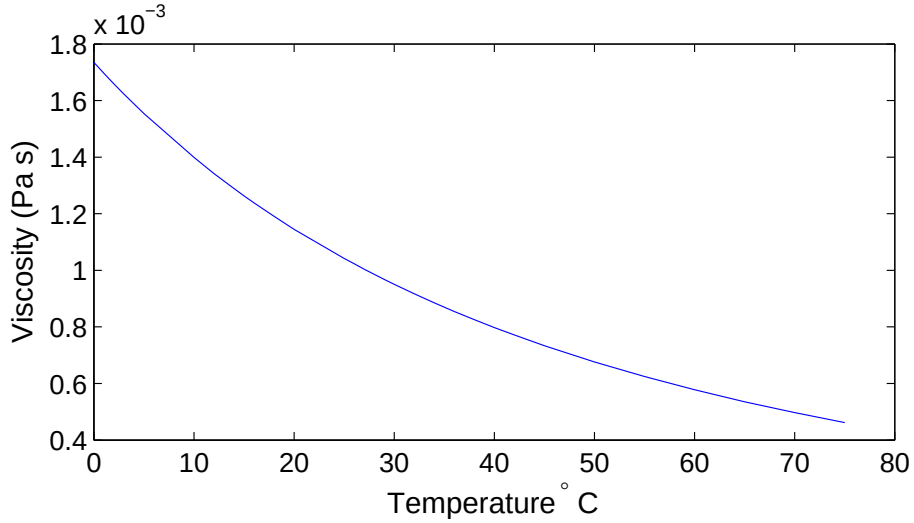

Figure I-1. Viscosity of Liquid Ethanol versus Temperature (For large range).

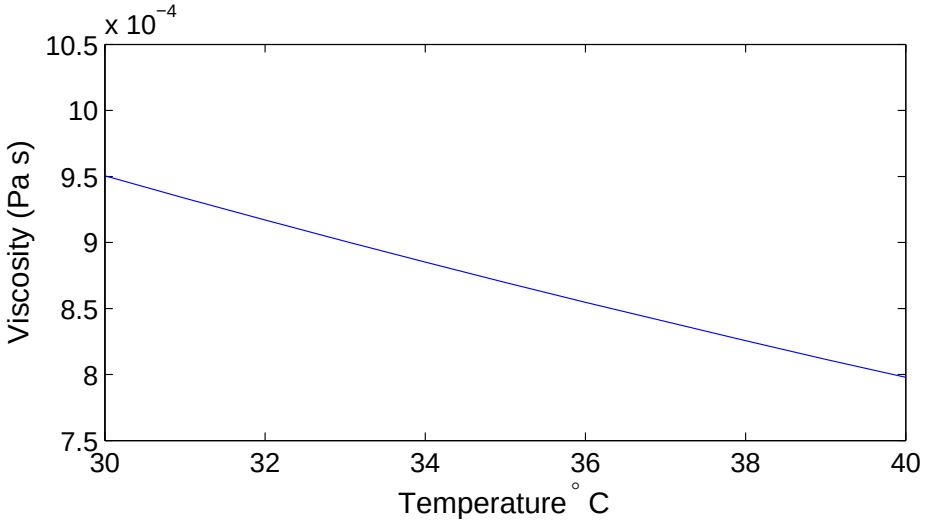

Figure I-2. Viscosity of Liquid Ethanol versus Temperature (For small range).

To represent viscosity dependence of the temperature a Boussinesq like approach is used. Recall that density dependence of temperature is given by

$$\rho = \rho_{ref}\left[1 + \beta\left(T - T_{ref}\right)\right] \& \rho^* = \rho^*_{ref}\left[1 + \beta^*\left(T^* - T_{ref}\right)\right]$$

and viscosity dependence is

$$\mu = \mu_{ref} + \psi\left(T - T_{ref}\right) \ \& \ \mu^* = \mu^*_{ref} + \psi^*\left(T^* - T_{ref}\right)$$

where, μ_{ref} & μ^*_{ref} are the viscosities at a reference temperature. ψ & ψ^* are the viscosity correction coefficients. For the liquid phase ψ is negative and for the vapor phase ψ is positive. (In the liquid phase $\mu = \mu_{ref} + \left(-1.5 \cdot 10^{-5}\right)\left(T - T_{ref}\right)$, recall that the reference temperature is the cold plate temperature)

Momentum equations in both phases requires modification for non-constant viscosity model and the following equation gives momentum equation in its general form,

$$\rho\left(\frac{\partial \vec{v}}{\partial t} + \vec{v} \cdot \nabla \vec{v}\right) = -\nabla P + \rho \vec{g} + \nabla \cdot \vec{\vec{S}}$$

where $\vec{\vec{S}} = 2\mu\left(T\right)\left(\frac{\nabla \vec{v} + \nabla \vec{v}^t}{2}\right) \rightarrow \nabla \cdot \vec{\vec{S}} = \mu \nabla^2 \vec{v} + \nabla \mu \cdot \left(\nabla \vec{v} + \nabla \vec{v}^t\right)$ and for cylindrical coordinates

$$\nabla \vec{v} = \begin{vmatrix} \vec{i}_r \vec{i}_r \frac{\partial v_r}{\partial r} & \vec{i}_r \vec{i}_\theta \frac{\partial v_\theta}{\partial r} & \vec{i}_r \vec{i}_r \frac{\partial v_r}{\partial r} \\ \vec{i}_\theta \vec{i}_r \frac{1}{r}\left(\frac{\partial v_r}{\partial \theta} - v_\theta\right) & \vec{i}_\theta \vec{i}_\theta \frac{1}{r}\left(\frac{\partial v_\theta}{\partial \theta} + v_r\right) & \vec{i}_\theta \vec{i}_z \frac{1}{r}\frac{\partial v_z}{\partial \theta} \\ \vec{i}_z \vec{i}_r \frac{\partial v_r}{\partial z} & \vec{i}_z \vec{i}_\theta \frac{\partial v_\theta}{\partial z} & \vec{i}_z \vec{i}_z \frac{\partial v_z}{\partial z} \end{vmatrix}$$

and

$$\nabla \vec{v} = \begin{vmatrix} \vec{i}_r \vec{i}_r \frac{\partial v_r}{\partial r} & \vec{i}_r \vec{i}_\theta \frac{1}{r}\left(\frac{\partial v_r}{\partial \theta} - v_\theta\right) & \vec{i}_r \vec{i}_r \frac{\partial v_r}{\partial z} \\ \vec{i}_\theta \vec{i}_r \frac{\partial v_\theta}{\partial r} & \vec{i}_\theta \vec{i}_\theta \frac{1}{r}\left(\frac{\partial v_\theta}{\partial \theta} + \vec{v}_r\right) & \vec{i}_\theta \vec{i}_z \frac{\partial v_\theta}{\partial z} \\ \vec{i}_z \vec{i}_r \frac{\partial v_r}{\partial r} & \vec{i}_z \vec{i}_\theta \frac{1}{r}\frac{\partial v_z}{\partial \theta} & \vec{i}_z \vec{i}_z \frac{\partial v_z}{\partial z} \end{vmatrix}$$

By substituting the definition of $\nabla \cdot \vec{\vec{S}}$ into the momentum equation we get

$$\rho\left(\frac{\partial \vec{v}}{\partial t} + \vec{v} \cdot \nabla \vec{v}\right) = -\nabla P + \rho \vec{g} + \mu \nabla^2 \vec{v} + \nabla \mu \cdot \left(\nabla \vec{v} + \nabla \vec{v}^t\right)$$

and using the density and viscosity expansions we have

$$\rho_{ref}\left(\frac{\partial\vec{v}}{\partial t}+\vec{v}\cdot\nabla\vec{v}\right)=-\nabla P+\rho_{ref}\beta\left(T-T_{ref}\right)g\vec{i_z}+\ldots$$

$$\left[\mu_{ref}+\psi\left(T-T_{ref}\right)\right]\nabla^2\vec{v}+\nabla\left[\mu_{ref}+\psi\left(T-T_{ref}\right)\right]\cdot\left(\nabla\vec{v}+\nabla\vec{v}^t\right)$$

The scaled non-linear momentum equations for liquid and vapor phases become,

$$\frac{1}{\mathrm{Pr}}\left(\frac{\partial\vec{v}}{\partial t}+\vec{v}\cdot\nabla\vec{v}\right)=-\nabla P+Ra\,T\vec{i_z}+\nabla^2\vec{v}+E_\mu T\nabla^2\vec{v}+E_\mu\nabla T\cdot\left(\nabla\vec{v}+\nabla\vec{v}^t\right)$$

and

$$\frac{\nu}{\nu^*}\frac{1}{\mathrm{Pr}}\left(\frac{\partial\vec{v}^*}{\partial t}+\vec{v}^*\cdot\nabla\vec{v}^*\right)=-\frac{\mu_{ref}}{\mu^*_{ref}}\nabla P^*+\frac{\beta^*}{\beta}\frac{\nu}{\nu^*}Ra\,T^*\vec{i_z}+\nabla^2\vec{v}^*\ldots$$
$$+E^*_\mu T\nabla^2\vec{v}^*+E^*_\mu\nabla T^*\cdot\left(\nabla\vec{v}^*+\nabla\vec{v}^{*t}\right)$$

Upon perturbation the linearized momentum equation in the liquid phase

$$\frac{1}{\mathrm{Pr}}\left(\frac{\partial\vec{v}_1}{\partial t}\right)=-\nabla P_1+Ra\,T_1\vec{i_z}+\nabla^2\vec{v}_1+E_\mu T_0\nabla^2\vec{v}_1+E_\mu\nabla T_0\cdot\left(\nabla\vec{v}_1+\nabla\vec{v}_1^t\right)$$

and for the vapor phase

$$\frac{\nu}{\nu^*}\frac{1}{\mathrm{Pr}}\left(\frac{\partial\vec{v}^*_1}{\partial t}\right)=-\frac{\mu_{ref}}{\mu^*_{ref}}\nabla P^*_1+\frac{\beta^*}{\beta}\frac{\nu}{\nu^*}Ra\,T^*_1\vec{i_z}+\nabla^2\vec{v}^*_1+E^*_\mu T_0\nabla^2\vec{v}^*_1+E^*_\mu\nabla T^*_0\cdot\left(\nabla\vec{v}^*_1+\nabla\vec{v}^{*t}_1\right)$$

where $E_\mu=\dfrac{\psi\Delta T}{\mu_{ref}}$ and $E^*_\mu=\dfrac{\psi^*\Delta T}{\mu^*_{ref}}$

In addition to the domain momentum equations, the force balance at the interface needs modification for non-constant viscosity model. Recall that the force balance is given by

$$-\vec{\vec{T}}\cdot\vec{n}+\gamma 2H\cdot\vec{n}+\vec{t}\nabla_s\gamma=-\vec{\vec{T}}^*\cdot\vec{n}$$

where $\vec{\vec{T}}=-P\vec{\vec{I}}+\vec{\vec{S}}$ and $\vec{\vec{S}}=2\mu\left(T\right)\left(\dfrac{\nabla\vec{v}+\nabla\vec{v}^t}{2}\right)=\mu_{ref}\left(\nabla\vec{v}+\nabla\vec{v}^t\right)+$
$\psi\left(T-T_{ref}\right)\left(\nabla\vec{v}+\nabla\vec{v}^t\right)$

Derivations for the normal stress balance and tangential stress balances for constant viscosity were already given earlier. Also the we showed the momentum equation for the non-constant viscosity case in detail; therefore, here we will only show

the final perturbed version of stress balances for the non-constant viscosity model.

$$\frac{\mu^*}{\mu}\left(\frac{\partial v_{r1}^*}{\partial z}+\frac{1}{\chi}\frac{\partial v_{z1}^*}{\partial r}\right)-\left(\frac{\partial v_{r1}}{\partial z}+\frac{1}{\chi}\frac{\partial v_{z1}}{\partial r}\right)=\frac{Ma}{\chi}\left(\frac{\partial T_1}{\partial r}+\frac{dT_0}{dz}\frac{\partial Z_1}{\partial r}\right)\ldots$$

$$-E_\mu T_0^*\frac{\psi^*}{\psi}\left(\frac{\partial v_{r1}^*}{\partial z}+\frac{1}{\chi}\frac{\partial v_{z1}^*}{\partial r}\right)+E_\mu T_0\left(\frac{\partial v_{r1}}{\partial z}+\frac{1}{\chi}\frac{\partial v_{z1}}{\partial r}\right)$$

and

$$\frac{\mu^*}{\mu}\left(\frac{\partial v_{\theta 1}^*}{\partial z}+\frac{im}{\chi r}v_{z1}^*\right)-\left(\frac{\partial v_{\theta 1}}{\partial z}+\frac{im}{\chi r}v_{z1}\right)=\frac{im}{\chi r}Ma\left(T_1+\frac{dT_0}{dz}Z_1\right)-\ldots$$

$$E_\mu T_0^*\frac{\psi^*}{\psi}\left(\frac{\partial v_{\theta 1}^*}{\partial z}+\frac{im}{\chi r}v_{z1}^*\right)+E_\mu T_0\left(\frac{\partial v_{\theta 1}}{\partial z}+\frac{im}{\chi r}v_{z1}\right)$$

The normal stress balance becomes,

$$Ca\,(P_1-P_1^*)+2Ca\left(\frac{\mu^*}{\mu}\frac{\partial v_{z1}^*}{\partial z}-\frac{\partial v_{z1}}{\partial z}\right)+\left[\frac{1}{\chi^2}\left(\frac{\partial^2}{\partial r^2}+\frac{1}{r}\frac{\partial}{\partial r}-\frac{m^2}{r^2}\right)-Bo\right]Z_1=\ldots$$

$$2Q_\mu\left(T_0\frac{\partial v_{z1}}{\partial z}-T_0^*\frac{\psi^*}{\psi}\frac{\partial v_{z1}^*}{\partial z}\right)$$

where $Q_\mu=\dfrac{\psi\kappa\Delta T}{h\gamma}$.

APPENDIX J
HOW TO COMPARE 3-D PERIODIC MODEL WITH 1-D MODEL

To validate our numerical results of 3-D periodic calculations with 1-D calculations, we apply the curl operator twice on the linearized motion equations for both the upper fluid and lower fluid. Hence, the pressure, azimuthal velocity and radial velocity are eliminated in favor of the perturbed vertical velocity and temperature. We obtain for $\sigma = 0$.

$$\nabla^4 v_z + Ra_T \nabla^2 T = 0$$

$$\nabla^4 v_z^* + \frac{\nu}{\nu^*}\frac{\beta^*}{\beta} Ra_T \nabla^2 T^* = 0$$

$$\nabla^2 T - v_z \frac{dT_0}{dz} = 0$$

$$\nabla^2 T^* - \frac{\kappa}{\kappa^*} v_z^* \frac{dT_0^*}{dz} = 0$$

We can expand the variables in the liquid phase as

$$v_z = \cos(m\theta) J_m(k_{m,j} r) w(z)$$

$$T = \cos(m\theta) J_m(k_{m,j} r) \Theta(z)$$

$$v_r = \frac{1}{k_{m,j}} \cos(\mathrm{m}\theta) \mathrm{J}'_{\mathrm{m}}(k_{\mathrm{m,j}}\mathrm{r}) \frac{\mathrm{dw(z)}}{\mathrm{dz}}$$

$$v_\theta = -\frac{m}{k_{m,j}^2 r} \sin(\mathrm{m}\theta) \mathrm{J}_{\mathrm{m}}(k_{\mathrm{m,j}}\mathrm{r}) \frac{\mathrm{dw(z)}}{\mathrm{dz}}$$

Expanded variables in the vapor phase;

$$v_z^* = \cos(\mathrm{m}\theta) \mathrm{J}_{\mathrm{m}}(k_{\mathrm{m,j}}\mathrm{r}) \mathrm{w}^*(\mathrm{z})$$

$$T^* = \cos(m\theta) J_m(k_{m,j} r) \Theta^*(z)$$

$$v_r^* = \frac{1}{k_{m,j}} \cos(\mathrm{m}\theta) \mathrm{J}'_{\mathrm{m}}(k_{\mathrm{m,j}}\mathrm{r}) \frac{\mathrm{dw^*(z)}}{\mathrm{dz}}$$

$$v_\theta^* = -\frac{m}{k_{m,j}^2 r} \sin(\mathrm{m}\theta) \mathrm{J}_{\mathrm{m}}(k_{\mathrm{m,j}}\mathrm{r}) \frac{\mathrm{dw^*(z)}}{\mathrm{dz}}$$

Where J_m&J'_m: Bessel function J and its derivative.

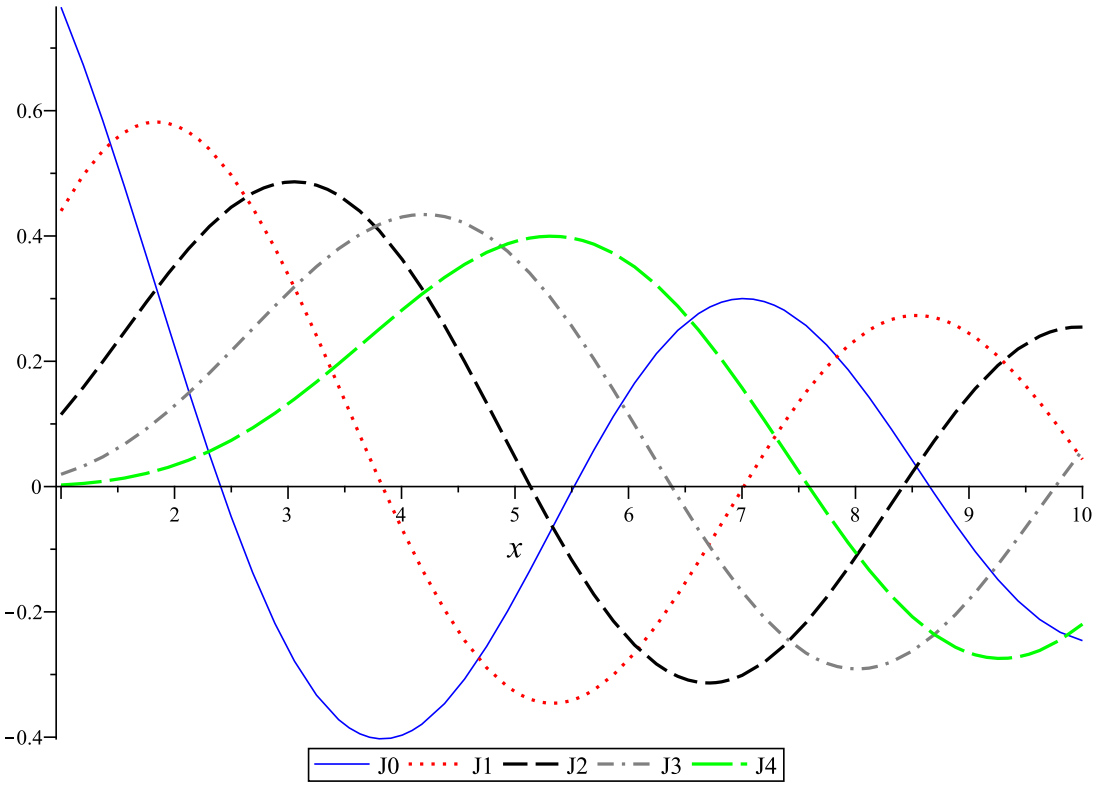

Figure J-1. J kind Bessel functions.

The above expansions assume separability in the r direction and this of course puts a restriction on the boundary conditions. Thus the comparison between 3-D and 1-D can be done when such expansions are valid and compatible with the boundary conditions, no slip being excluded from the compatible conditions.

Substituting the above expansions into the domain equations given in Appendix H, results in a 1-D problem, which can be directly compared with the results of 3-D calculations. The way to do it is to find a relation between wave number, k_{mj}, and azimuthal mode m for each aspect ratio and that is done by substituting; $v_z = \cos(\mathrm{m}\theta)\mathrm{J_m}(k_{\mathrm{m,j}}\mathrm{r})\mathrm{w(z)}$ into $\frac{\partial v_z}{\partial r}\Big|_{r=\chi} = 0$.

The dimensionless wave number is therefore given as

$$k_{\mathrm{m,j}} = \frac{Jr_{m,j}}{\chi}$$

where $Jr_{m,j}$ are the roots of the first derivatives of Bessel function for any fixed azimuthal mode number m and χ is the aspect ratio of the system. For reference purposes in the Figures J-1 and J-2 the Bessel functions and their derivatives are plotted.

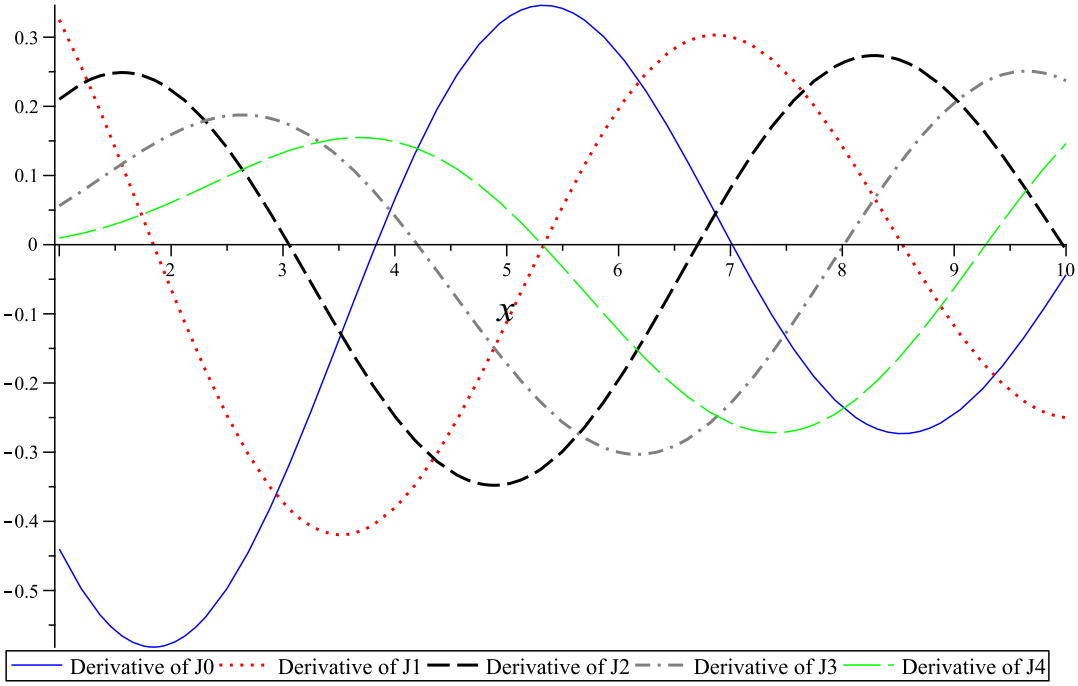

Figure J-2. Derivative of J kind Bessel functions.

Table J-1. Roots of the J'_m, $Jr_{m,j}$.

	J'_0	J'_1	J'_2	J'_3	J'_4
1^{st}	3.83	1.84	3.05	4.20	5.31
2^{nd}	7.01	5.33	6.70	8.01	9.28
3^{rd}	10.17	8.53	9.96	11.34	12.68
4^{th}	16.47	11.70	13.17	14.58	15.96

An example to compare the 3-D calculation with aspect ratio 1.5 and azimuthal mode 1;

$$k_{\mathrm{m,j}} = \frac{Jr_{m,j}}{\chi} = \frac{1.84}{1.5} \cong 1.22$$

APPENDIX K
DOMAIN VARIABLE EXPANSION AND MAPPINGS

In this appendix, the perturbation equations used in the theoretical work are explained. This is done for a one-dimensional domain and the reader is referred to Johns and Narayanan [29] for details

Let u denote the solution of a problem in an irregular domain D where D is not specified and must be determined as part of the solution. Imagine that D lies in the vicinity of a reference domain D_0 and can be expressed in terms of the reference domain via a parameter ε. Let u be a function of a spatial coordinate z. Then u must be a function of ε directly because it lies on D and also because it is a function of z. By an irregular domain it is meant a domain that is not convenient. Now to solve for u and obtain D simultaneously we can solve a series of companion problems defined on the nearby regular or convenient domain, D_0, which we called the reference domain. What needs to be done is to discover how to determine u in terms of the solutions to problems defined on. The points of D_0 will be denoted by the coordinate z_0 and those of D by the coordinate z.

Imagine a family of domains D_ε growing out of the reference domain D_0. u must be determined on each of these. The point z of the domain D_ε is then determined in terms of the point z_0 of the reference domain D_0 by the mapping.

$$z = f(z_0, \varepsilon)$$

The equation above is a little more general than necessary to explain the mapping for our purposes. In the problems of this study, only one part of the domain is irregular, namely the interface.

Now, to get going let us expand the function f in powers of ε as

$$f(z_0, \varepsilon) = f(z_0, \varepsilon = 0) + \varepsilon \frac{\partial f(z_0, \varepsilon = 0)}{\partial \varepsilon} + \frac{1}{2}\varepsilon^2 \frac{\partial^2 f(z_0, \varepsilon = 0)}{\partial \varepsilon^2} + \ldots$$

where $f(z_0, \varepsilon = 0) = z_0$ and the derivatives of f are evaluated holding $z_0$fixed. Then in terms of the notation

$$z_1(z_0, \varepsilon) = \frac{\partial f(z_0, \varepsilon = 0)}{\partial \varepsilon}$$
$$z_2(z_0, \varepsilon) = \frac{\partial^2 f(z_0, \varepsilon = 0)}{\partial \varepsilon^2}$$
$$\vdots$$

the mapping can be written as

$$z = z_0 + \varepsilon z_1(z_0, \varepsilon = 0) + \frac{1}{2}\varepsilon^2 z_2(z_0, \varepsilon = 0) + \ldots$$

Also, the boundary of the reference domain must be carried into the boundary of the present domain by the same mapping. The function, Z, which describes the boundary of the new domain, inherits its expansion in powers of from the mapping given in and can be written as

$$Z = Z_0 + \varepsilon Z_1(Z_0, \varepsilon = 0) + \frac{1}{2}\varepsilon^2 Z_2(Z_0, \varepsilon = 0) + \ldots$$

It is the Z_i's that need to be determined to specify the domain D_ε in terms of the domain D_0.

Accordingly, $u(z,\varepsilon)$ can be expanded in powers of ε along the mapping as

$$u(z,\varepsilon) = u(z = z_0,\varepsilon = 0) + \varepsilon \frac{du(z = z_0,\varepsilon = 0)}{d\varepsilon} + \frac{1}{2}\varepsilon^2 \frac{d^2u(z = z_0,\varepsilon = 0)}{d\varepsilon^2} + \ldots$$

where $\frac{du}{d\varepsilon}$ denotes the derivative of the function u depending on z and ε taken along the mapping. To obtain a formula for $\frac{du(z = z_0,\varepsilon = 0)}{d\varepsilon}$, differentiate u along the mapping taking z to depend on ε, holding z_0 fixed. Using the chain rule, this gives

$$\frac{du(z,\varepsilon)}{d\varepsilon} = \frac{\partial u(z,\varepsilon)}{\partial \varepsilon} + \frac{\partial u(z,\varepsilon)}{\partial z}\frac{\partial f(z_0,\varepsilon)}{\partial \varepsilon}$$

Now, set ε to zero in the above equation to get

$$\frac{du(z = z_0,\varepsilon = 0)}{d\varepsilon} = \frac{\partial u(z_0,\varepsilon = 0)}{\partial \varepsilon} + \frac{\partial u(z_0,\varepsilon = 0)}{\partial z} z_1(z_0, \varepsilon)$$

Then, introduce the definition of u_1 via

$$u_1(z_0) = \frac{\partial u(z_0, \varepsilon = 0)}{\partial \varepsilon}$$

and observe that

$$\frac{\partial u(z_0, \varepsilon = 0)}{\partial z} = \frac{\partial u_0(z_0)}{\partial z_0}$$

to get

$$\frac{du(z = z_0, \varepsilon = 0)}{d\varepsilon} = u_1(z_0) + \frac{\partial u_0(z_0)}{\partial z_0} z_1(z_0, \varepsilon)$$

All the other orders of the derivatives of u can be determined the same way. Finally, if a domain variable needs to be specified at the boundary it is written as

$$\frac{du(z = Z_0, \varepsilon = 0)}{d\varepsilon} = u_1(Z_0) + \frac{\partial u_0(Z_0)}{\partial z_0} Z_1(Z_0, \varepsilon)$$

When additional derivatives are obtained and plugged into the expansion of u, it becomes

$$u(z, \varepsilon) = u_0 + \varepsilon \left(u_1 + \frac{\partial u_0}{\partial z_0} z_1 \right) + \frac{1}{2} \varepsilon^2 \left(u_2 + 2 \frac{\partial u_1}{\partial z_0} z_1 + \frac{\partial^2 u_0}{\partial z_0^2} z_1^2 + \frac{\partial u_0}{\partial z_0} z_2 \right) + \dots$$

The careful reader will notice that the mapping z_1 does not appear in the domain equations given in the work. To show why, let us work out an example and so let u satisfy an equation

$$\frac{\partial u}{\partial z} = 0$$

in the new domain. Our reference domain, however, is in the coordinate system, z_0. Thus,

$$\frac{\partial u}{\partial z} = \frac{\partial u}{\partial z_0} \frac{\partial z_0}{\partial z}$$

Hence, we must differentiate the right hand side of the expansion of u with respect to z_0, holding ε fixed and then multiply it by $\frac{\partial z_0}{\partial z} = 1 - \varepsilon \frac{\partial z_1}{\partial z} - \frac{1}{2} \varepsilon^2 \frac{\partial z_2}{\partial z} - \dots$

This gives us to the first order

$$\frac{\partial u}{\partial z} = \frac{\partial u_0}{\partial z_0} + \varepsilon \left(\frac{\partial u_1}{\partial z_0} + \frac{\partial^2 u_0}{\partial z_0^2} z_1 \right) + \dots$$

See how the derivatives of z_1 and z_2 are lost during the step where we multiplied the derivative of u with respect to z_0 by $\frac{\partial z_0}{\partial z}$. Now going back to our example and plugging this in, we get

$$\frac{\partial u}{\partial z} = \frac{\partial u_0}{\partial z_0} + \varepsilon \left(\frac{\partial u_1}{\partial z_0} + \frac{\partial^2 u_0}{\partial z_0^2} z_1 \right) + \dots = 0$$

In the domain

$$\frac{\partial u_0}{\partial z_0} = 0$$

and accordingly, $\frac{\partial^2 u_0}{\partial z_0^2} = 0$, which gives

$$\frac{\partial u_1}{\partial z_0} = 0$$

The mapping is lost from domain equations. If surface variables were considered the mapping would not be lost.

APPENDIX L
BINARY MIXTURE PROPERTIES

The mixture properties are typically calculated using simple mixing rules with respect to either mass or mole fraction such as for density, latent heat, and surface tension.

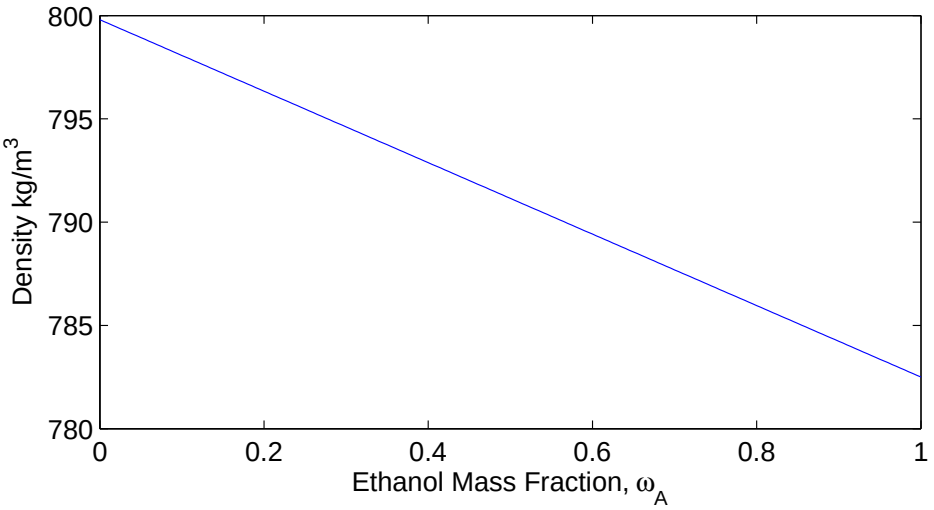

Figure L-1. Density of the liquid mixture with respect to mass fraction.

For example for both liquid and vapor densities are calculated using;

$$\rho_{\text{mix}} = \omega_A \rho_A + (1 - \omega_A)\, \rho_B$$

here ω_A is the mass fraction of ethanol.

Latent heat and surface tension of the mixture are calculated using the mole fraction instead of the mass fraction such as surface tension of the mixture is given by,

$$\gamma_{\text{mix}} = x_A \gamma_A + (1 - x_A)\, \gamma_B$$

here x_A is the mole fraction of ethanol.

Refutas equation is used to calculate the liquid mixture viscosity and it is done in three steps. The first step is to calculate the Viscosity Blend Number (VBN) for each

component,

$$VBN_A = 14.534 \times \log\left(\log\left(\nu_A + 0.8\right)\right) + 10.975$$

$$VBN_B = 14.534 \times \log\left(\log\left(\nu_B + 0.8\right)\right) + 10.975$$

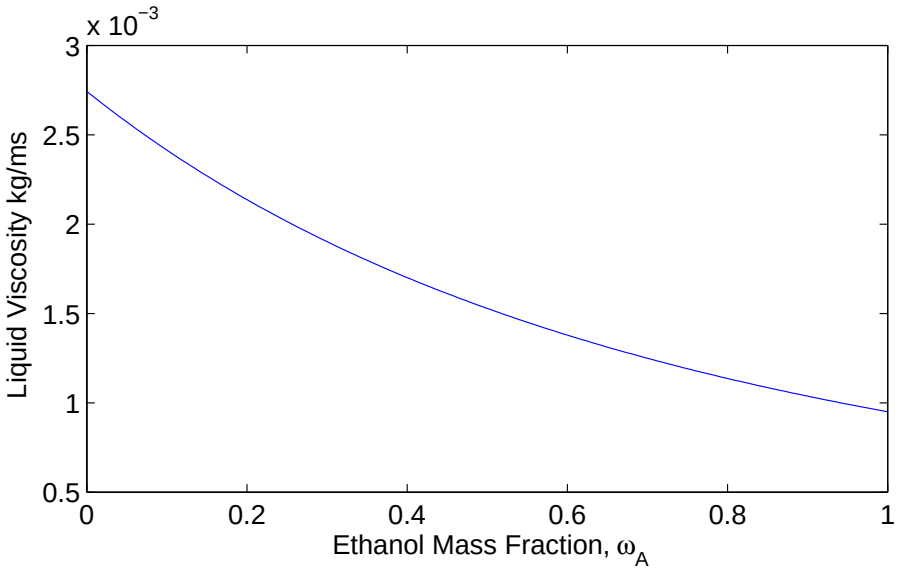

Figure L-2. Viscosity of the liquid mixture with respect to mass fraction.

Next step is the calculate the VBN of the mixture,

$$VBN_{mix} = \omega_A VBN_A + \left(1 - \omega_A\right) VBN_B$$

and the last step is to get the viscosity of the mixture,

$$\nu_{mix} = \exp\left(\exp\left(VBN_{mix} - 10.975\right)/14.534\right) - 0.8$$

Note that to use the Refutas equation we need each component viscosity in centistokes unit.

The gas mixture viscosity is calculated using method of Wilke which is an empirical formula for alcohol mixtures. The method requires calculating the viscosity coefficients

of each component using the following equation,

$$\Psi_{AB} = \left(1 + \left(\frac{\mu_A^*}{\mu_B^*}\right)^{0.5} \left(\frac{M_A}{M_B}\right)^{0.25}\right)^2 \Bigg/ \left(8\left(1 + \left(\frac{M_A}{M_B}\right)\right)\right)^{0.5}$$

$$\Psi_{AB} = \Psi_{BA}\left(\frac{\mu_B^* M_A}{\mu_A^* M_B}\right)$$

and the viscosity of the mixture

$$\mu_{mix}^* = \left(y_A \mu_A^*\right)\left(\left(1 - y_A\right) + y_A \Psi_{BA}\right)/\left(y_A + \left(1 - y_A\right)\Psi_{AB}\right)$$

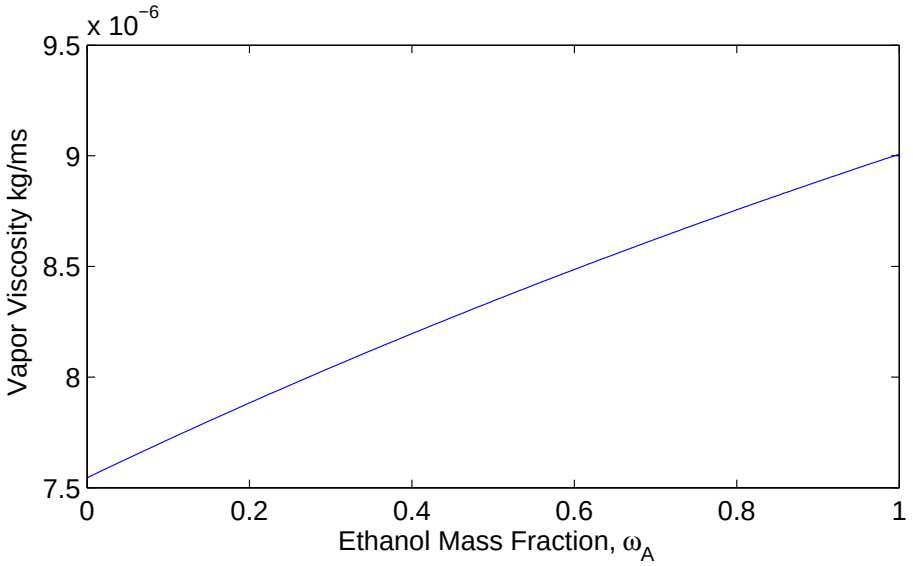

Figure L-3. Viscosity of the vapor mixture with respect to mass fraction.

Same method is used for thermal conductivity of the vapor mixture by just replacing the viscosity terms with thermal conductivities.

At last for the liquid thermal conductivity Filippov equation is used with mass fractions of the each component.

$$k_{mix} = \omega_A k_A + \left(1 - \omega_A\right) k_B + abs\left(k_A - k_B\right)\left(1 - \omega_A\right)^{0.5} \omega_A$$

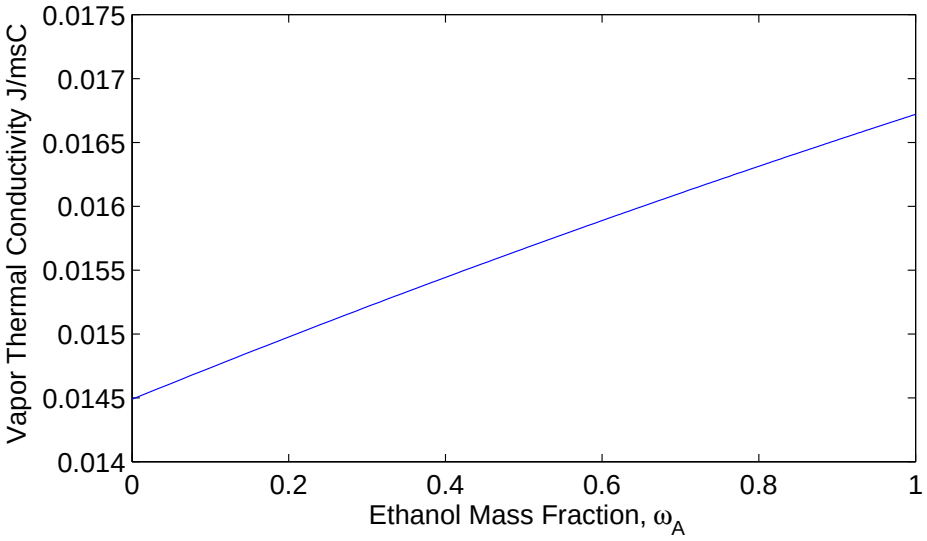

Figure L-4. Thermal conductivity of the vapor mixture with respect to mass fraction.

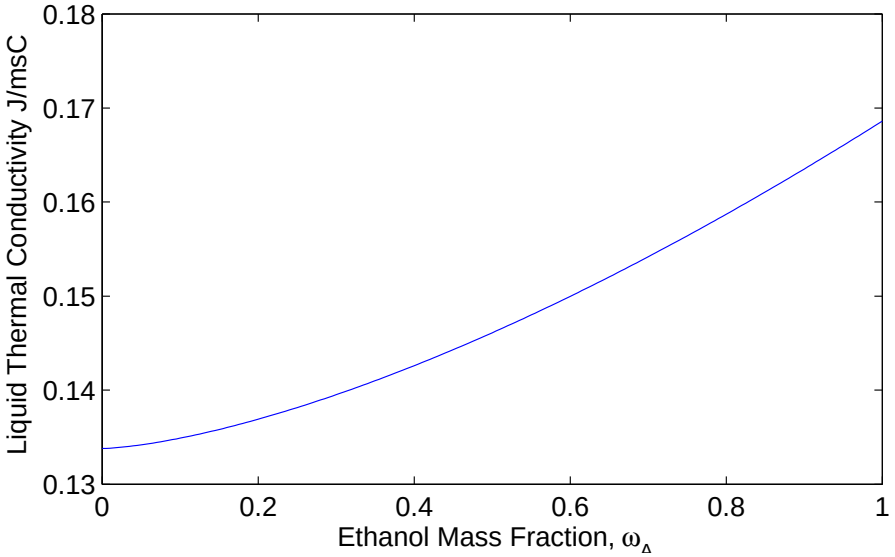

Figure L-5. Thermal conductivity of the liquid mixture with respect to mass fraction.

APPENDIX M
SIMPLE EVAPORATIVE INSTABILITY EXPERIMENT FOR MIDDLE SCHOOLS

In this appendix a simple set of experiments are proposed (also results are shown) for middle school science classes. The following set of experiments is simple to conduct but shows the important physics of an evaporative convective system. The main idea of the experiments is to show the effect of evaporation, density stratification and viscosity. We will need;

- 3 easy to find liquids; ethanol (instead of ethanol other alcohols can be used), water, and glycerin,
- Petri dishes, sample experiments are done with 6 inch diameter petri dishes,
- Containers with a lid ($75\ ml$, preferably glass or plastic ones through which you can see),
- Food coloring,
- Kalliroscope tracer. (This can be easily ordered online)

In the first experiment we will show the effect of evaporation by comparing the evaporation of ethanol with water. Note that ethanol is more volatile than water. To visualize the flow we first need to mix the tracer with our liquids using the containers. For $50\ ml$ of ethanol or water less than a gram of tracer would be sufficient. You can always try and see if it is sufficient by adding a little at a time and check if you can visualize a flow when you shake the container. Adding food coloring will create a contrast that might help to see the flow. After mixing the tracer with the liquids, simply pour the liquids into petri dishes. You will observe some pattern formation due to flow in the ethanol, shown in Figure M-1, but no-flow in the water, shown in Figure M-2.

Let us first explain why we see flow in ethanol but not in water. This is mainly because ethanol evaporates more than water and due to this evaporation the surface of the ethanol gets cooler compared to the bottom of the petri dish. In other words the surface of the ethanol becomes heavier and wants to move down pushing the liquid from the bottom to the surface. However, this density stratification is not the only reason why

Figure M-1. Evaporating ethanol layer. Pattern formation.

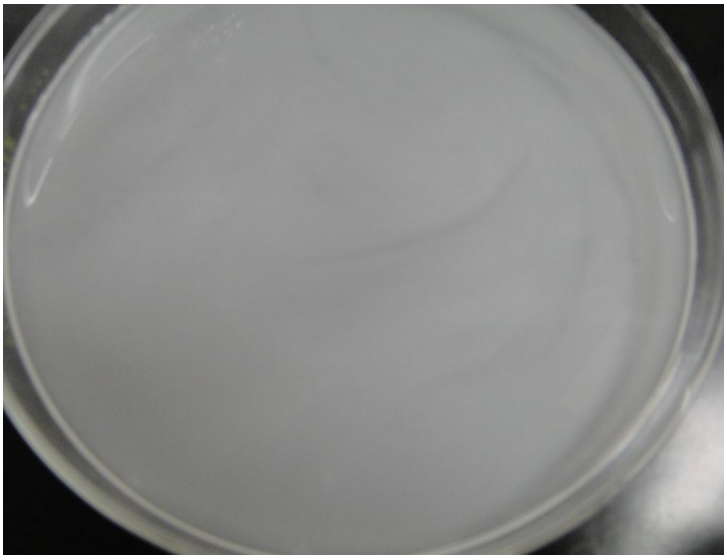

Figure M-2. Water layer. No-Flow.

you see flow in ethanol but not in water. Evaporation itself creates flow in ethanol too which is weak in water.

If you want to see the patterns and flow in water you will need to put the petri dish on top of a heater, shown in Figure M-3. (You should keep the heater in its lowest position because you do not want to boil the water). Heating from below creates the

density stratification like evaporation did in ethanol. It makes the bottom water lighter than the top and initiate flow.

Figure M-3. Water layer heating from below. Pattern formation. (Food coloring is added)

To see the effect of viscosity we will add around $3\ ml$ glycerin to $50\ ml$ ethanol. This will mainly make the viscosity of ethanol higher. After adding glycerin again pour the liquid into the petri dish. You will not able see the any flow in the petri dish. This is mainly because by adding glycerin you increased the viscosity of ethanol and viscosity works against flow.

REFERENCES

[1] J. R. Pearson, On convection cells induced by surface tension, J. Fluid Mech. 4 (1958) 489–500.

[2] L. Rayleigh, On convection currents in a horizontal layer of fluid, when the higher temperature is on the under side, Phil. Mag. 32 (1916) 529–546.

[3] H. Bénard, Les tourbillons cellulaires dans une nappe liquide, Rev. Gen. Sciences Pure Appl. 11 (1900) 1261–1271.

[4] S. Chandrasekhar, Hydrodynamic and Hydromagnetic Stability, Oxford University Press, Oxford, 1961.

[5] J. P. Burelbach, S. G. Bankoff, S. H. Davis, Nonlinear stability of evaporating and condensing liquid films, J. Fluid Mech. 195 (1988) 692–714.

[6] J. Margerit, M. Dondlinger, P. Dauby, Improved 1.5-sided model for the weakly nonlinear study of benardmarangoni instabilities in an evaporating liquid layer, J. Colloid Interface Sci. 290 (2005) 220–230.

[7] A. Oron, Nonlinear dynamics of thin evaporating liquid films subject to internal heat generation, Fluid Dynamics at Interfaces (1999) 3–15.

[8] A. Huang, D. D. Joseph, Instability of the equilibrium of a liquid below its vapour between horizontal heated plates, J. Fluid Mech. 242 (1992) 235–247.

[9] O. Ozen, R. Narayanan, The physics of evaporative and convective instabilities in bilayer systems: Linear theory, Phys. Fluids 16 (2004) 4644–4653.

[10] O. Ozen, R. Narayanan, The physics of evaporative and convective instabilities in bilayer systems: weakly nonlinear theory, Phys. Fluids 16 (2004) 4653–4661.

[11] B. Haut, P. Colinet, Surface-tension-driven instabilities of a pure liquid layer evaporating into an inert gas, J. Colloid Interface Sci. 285 (2005) 296–305.

[12] G. B. McFadden, S. R. Coriell, K. F. Gurski, D. L. Cotrellc, Onset of convection in two liquid layers with phase change, Phys. Fluids 19 (2007) 104109–13.

[13] W. Guo, R. Narayanan, Interfacial instability due to evaporation and convection: linear and nonlinear analyses, J. Fluid Mech. 650 (2010) 363–389.

[14] A. Oron, S. H. Davis, S. G. Bankoff, Long-scale evolution of thin liquid films, Rev. Mod. Phys. 69 (1997) 931–980.

[15] C. Ward, D. Stanga, Interfacial conditions during evaporation or condensation of water, Phys. Rev.E 64 (2001) 051509–9.

[16] J. Margerit, P. Colinet, G. Lebon, C. S. Iorio, J. C. Legros, Interfacial nonequilibrium and benard-marangoni instability of a liquid-vapor system, Phys. Rev. E 68 (2003) 041601–14.

[17] P. Shankar, M. Deshpande, On the temperature distribution in liquid vapor phase change between plane liquid surfaces, Phys. Fluids A 2 (1990) 1030–1038.

[18] P. G. de Gennes, Instabilities during the evaporation of a film: Non-glassy polymer + volatile solvent, Eur. Phys. 16 (2001) 421–430.

[19] B. Trouette, E. Chénier, C. Delcarte, B. Guerrier, Numerical study of convection induced by evaporation in cylindrical geometry, Eur. Phys. Special Topics 192 (2011) 83–93.

[20] H. Machrafi, A. Rednikov, P. Colinet, P. Dauby, Bénard instabilities in a binary-liquid layer evaporating into an inert gas, J. Colloid Interface Sci. 349 (2010) 331–353.

[21] H. Machrafi, A. Rednikov, P. Colinet, P. Dauby, Bénard instabilities in a binary-liquid layer evaporating into an inert gas: Stability of quasi-stationary and time-dependent reference profiles, Eur. Phys. Special Topics 192 (2011) 71–81.

[22] H. Mancini, D. Maza, Pattern formation without heating in an evaporative convection experiment, Europhys. Lett. 66 (2004) 812–850.

[23] J. Zhang, Surface Tension-Driven Flows and Applications, Research Signpost, India, 2006.

[24] J. Zhang, R. Behringer, A. Oron, Marangoni convection in binary mixtures, Phys. Rev. E 76 (2007) 016306–7.

[25] J. Zhang, A. Oron, R. Behringer, Novel pattern forming states for marangoni convection in volatile binary liquids, Phys. Fluids 23 (2011) 0721102–5.

[26] S. Dehaeck, C. Wylock, P. Colinet, Evaporating cocktails, Phys. Fluids 21 (2009) 091108–1.

[27] G. Toussaint, H. Bodiguel, F. Doumenc, B. Guerrier, C. Allain, Experimental characterization of buoyancy- and surface tension-driven convection during the drying of a polymer solution, Int. J. Heat Mass Transfer 51 (2008) 4228–4237.

[28] J. C. Slattery, Interfacial Transport Phenomena, Springer-Verlag, New York, 1990.

[29] L. E. Johns, R. Narayanan, Interfacial Instability, Springer-Verlag, New York, 2002.

[30] W. Guo, G. Labrosse, R. Narayanan, The Chebyshev Spectral Method in Transport Phenomena, Springer-Verlag, 2013.

[31] C. L. Yaws, Yaws′ Handbook of Thermodynamic and Physical Properties of Chemical Compounds, Knovel, 2003.

[32] R. E. Maples, Petroleum Refinery Process Economics 2^{nd} Edition, Pennwell Books, Tulsa, 2000.

[33] C. R. Wilke, A viscosity equation for gas mixtures, J. Chem. Phys. 18 (1950) 517.

[34] F. Ullmann, Ullmann's Chemical Engineering and Plant Design, Wiley-VCH, Hoboken, 2005.

[35] O. Ozen, Effect of vapor dynamics on interfacial instabilities, Ph.D. thesis, University of Florida, 2004.

[36] L. E. Scriven, C. V. Sternling, On cellular convection driven by surface tension gradients: effects of mean surface tension and surface viscosity, J. Fluid Mech. 19 (1964) 321–340.

BIOGRAPHICAL SKETCH

Kamuran Erdem UGUZ was born in Turkey. He graduated from Yildiz Technical University in Istanbul, Turkey, receiving a B.S. degree in chemical engineering in 2004. He then attended Bogazici University in Istanbul, Turkey, receiving a M.S. degree in chemical engineering in 2007.